

國立交通大學

材料科學與工程學系

博士論文

成長於氧化鎂基板上之氮氧化鈦與碳氧化鈦磊晶薄

膜結構與特性研究

Structure and properties of epitaxial titanium oxynitride
and titanium oxycarbide films on MgO substrate

研究生：Do Thi Hien

指導教授：張立 教授

中華民國 一百零二年 十月

國立交通大學

材料科學與工程學系

博士論文

成長於氧化鎂基板上之氮氧化鈦與碳氧化鈦磊晶薄

膜結構與特性研究

Structure and properties of epitaxial titanium oxynitride
and titanium oxycarbide films on MgO substrate

研究生：Do Thi Hien

指導教授：張立 教授

中華民國 一百零二年 十月

成長於氧化鎂基板上之氮氧化鈦與碳氧化鈦磊晶薄膜結構與特性
研究

Structure and properties of epitaxial titanium oxynitride and titanium
oxycarbide films on MgO substrate

研究生：杜氏賢

Student: Do Thi Hien

指導教授：張立 教授

Advisor: Dr. Li Chang



Submitted to Department of Materials Science and Engineering
College of Engineering
National Chiao Tung University
in partial Fulfillment of Requirements
for the Degree of Doctor of Philosophy
in
Materials Science and Engineering

October 2013
Hsinchu, Taiwan, Republic of China

中華民國 一百零二年 十月

成長於氧化鎂基板上之氮氧化鈦與碳氧化鈦磊晶薄膜結構與特性研究

研究生：杜氏賢 (Do Thi Hien)

指導教授：張立博士

國立交通大學材料科學與工程學系博士班

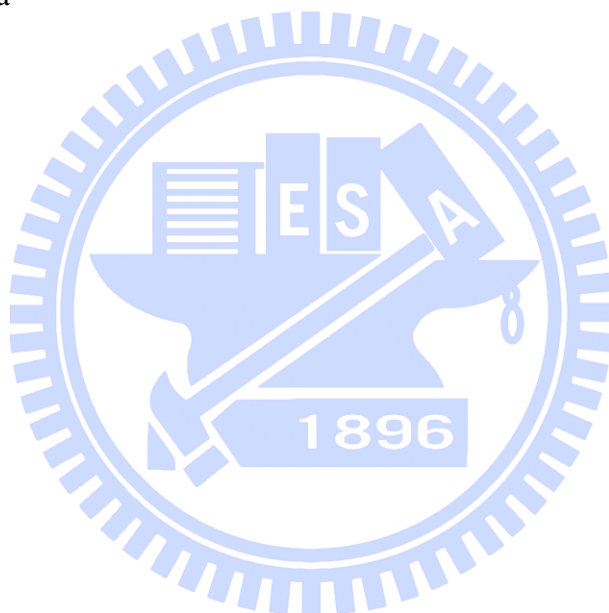
摘要

氮氧化鈦(TiN_xO_y) 與碳氧化鈦(TiC_xO_y)由於其獨特的特性，在科技領域中已成為非常受人矚目的材料。氮氧化鈦與碳氧化鈦由於具有相對新穎的組成，因此仍需要許多的研究與分析工作，以了解其相關特性。儘管目前已有許多相關的研究，但因欠缺單晶材料，而無法獲得基本性質。因此，在本研究中，將於 MgO 基板上沉積高品質之 TiN_xO_y 與 TiC_xO_y 磊晶薄膜，並探討 TiN_xO_y 在氫電漿蝕刻下的蝕刻狀況與穩定性。同時針對 TiN_xO_y 與 TiC_xO_y 磊晶薄膜的機械性質，進行深入的研究。

本論文研究的 $\text{TiC}_{0.47}\text{O}_{0.69}$ 與 TiN_xO_y 磊晶薄膜是使用脈衝雷射沉積法(pulsed laser deposition)於 MgO 基板上成長，薄膜具有不同化學的組成 ($0.63 < x < 1.11$, $0.1 < y < 0.55$)。X 光光電子能譜(X-ray photoelectron spectroscopy, XPS)及 X 光繞射(X-ray diffraction, XRD)的分析結果顯示，以異質磊晶方式沉積於 MgO 基板上的 TiN_xO_y 與 TiC_xO_y 薄膜，其結晶性佳，並且均處於完全壓縮應變(fully compressive strain)的狀態之下。所沉積的 TiN_xO_y 與 $\text{TiC}_{0.47}\text{O}_{0.69}$ 磊晶薄膜也都具有良好的導電特性。經由穿透式電子顯微鏡(Transmission electron microscopy, TEM)的分析得知， TiN_xO_y 與 $\text{TiC}_{0.47}\text{O}_{0.69}$ 薄膜內所含有的差排密度低，而原子力顯微鏡(Atomic force microscopy, AFM)的分析則顯現兩者的薄膜表面均相當平整。當氧的含量增加，會減少 TiN_xO_y 薄膜的導電性及晶格常數，殘留應力也因此隨之而減小。

另一方面，對 TiN_xO_y 磊晶薄膜進行氬電漿處理。掃描式電子顯微鏡(Scanning electron microscopy, SEM)、AFM 以及 XPS 的分析結果顯示， TiN_xO_y 的蝕刻與化學穩定性與氬氣壓力大小有著強烈的關係。當氬氣壓力低於 40 Torr 時， TiN_xO_y 仍然相當穩定並保有其良好的結晶性。隨著壓力的增加，將可能導致倒角錐狀之蝕刻凹坑的形成。

關於 TiN_xO_y 與 $\text{TiC}_{0.47}\text{O}_{0.69}$ 薄膜的機械性質，則使用奈米壓痕技術(nanoindentation)來加以量測。以 TiN_xO_y 薄膜而言，其薄膜硬度(H)與楊氏係數(E)分別約為 17~26 GPa 以及 355~430 GPa，不論是薄膜硬度或是楊氏係數，均隨著氧含量的增加而減小，隨著氮含量的增加而變高。而硬度與楊氏係數降低的同時，也發現其殘留壓應力亦會變小。另外在 TiC_xO_y 薄膜方面， $\text{TiC}_{0.47}\text{O}_{0.69}$ 經過量測所得到的數值為 $H \sim 21 \pm 1.7$ GPa 以及 $E \sim 390 \pm 6.4$ GPa。



Structure and properties of epitaxial titanium oxynitride and titanium oxycarbide films on MgO substrate

Student: Do Thi Hien

Advisor: Dr. Li Chang

Department of Materials Science and Engineering

National Chiao Tung University

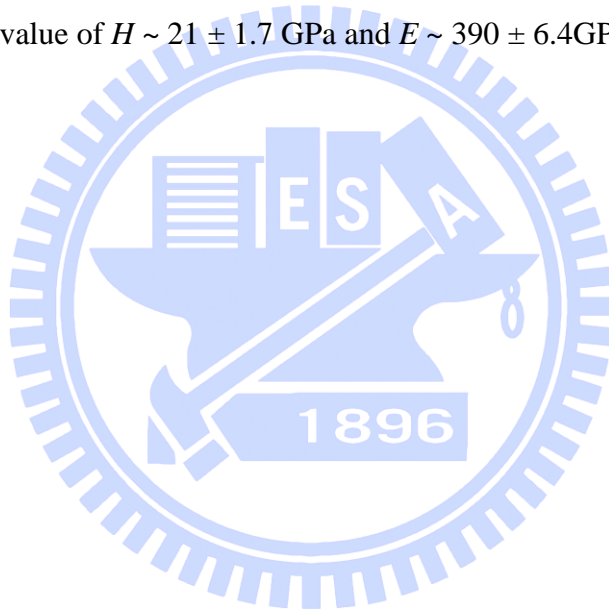
Abstract

Titanium oxynitride (TiN_xO_y) and titanium oxycarbide (TiC_xO_y) have become very attractive materials in the field of science and technology due to their unique properties. Because titanium oxynitride and titanium oxycarbide are of relatively new compositions, therefore, they still need more works and characterizations to explore their properties. Although there have been relatively large amounts of studies on titanium oxynitrides and titanium oxycarbides, some basic properties of the films have not been established due to the lack of single crystals. Therefore, in the thesis, we report the epitaxial growth of TiN_xO_y and TiC_xO_y films on MgO substrates. We also study the stability and etching of TiN_xO_y in hydrogen plasma. Mechanical properties of epitaxial TiN_xO_y and TiC_xO_y films are especially investigated.

The epitaxial $\text{TiC}_{0.47}\text{O}_{0.69}$ and TiN_xO_y films with different chemical composition ($0.63 < x < 1.11$, $0.1 < y < 0.55$) were deposited on MgO substrates by pulsed laser deposition method. X-ray photoelectron spectroscopy (XPS) and X-ray diffraction (XRD) analyses showed that the TiN_xO_y and $\text{TiC}_{0.47}\text{O}_{0.69}$ films are heteroepitaxially grown on MgO with good crystallinity and they are under compressive strain. Both deposited epitaxial TiN_xO_y and TiC_xO_y are very electrically conducting. Transmission electron microscopy analyses showed that TiN_xO_y and TiC_xO_y films contain a low density of dislocations. Atomic force microscopy (AFM) revealed very smooth surfaces of TiN_xO_y and $\text{TiC}_{0.47}\text{O}_{0.69}$ films. The increase in oxygen content reduces electrical conductivity and the lattice parameters of TiN_xO_y films, and residual stress decreases as a consequence.

Epitaxial TiN_xO_y films were treated under hydrogen plasma generated from microwave. Scanning electron microscopy (SEM), AFM, and XPS results showed that the stability and etching of TiN_xO_y strongly depend on hydrogen gas pressure. TiN_xO_y was very chemically stable and remained with good crystallinity under hydrogen pressure below 40 Torr. With increase of pressure, it may lead to the formation of etch pits in inverse pyramid shape.

The mechanical properties of TiN_xO_y and $\text{TiC}_{0.47}\text{O}_{0.69}$ films were characterized using nanoindentation. For TiN_xO_y films, hardness H and Young's modulus E are about 17 - 26 GPa and 355 - 430 GPa, respectively; both H and E decrease with increasing oxygen content and increase with increasing nitrogen content; a reduction of H and E with decreasing residual compressive stress are also observed. Titanium oxycarbide film with composition of $\text{TiC}_{0.47}\text{O}_{0.69}$ shows the value of $H \sim 21 \pm 1.7$ GPa and $E \sim 390 \pm 6.4$ GPa.



Acknowledgements

I am indebted to many people who contributed in several ways to this thesis, and supported me with their cooperation and timely help.

I particular, I wish to express my sincere gratitude to my research advisor Prof. Li Chang, for providing me an opportunity to work in his research group. I thank his for unique personal support in every aspect of the experimental work, for all the stimulating ideas, all the deep discussion, for providing support in preparation of various manuscripts for publications, presentations, posters and for the time he spent reviewing this thesis. He has been a great mentor with his enthusiasm, understanding and willingness to help students professionally and personally.

I am extremely thankful to Dr. Y.H. Han, Dr. J.C. Tian, Dr. C.Y. Peng, Mr. Tzu-Chun Yen, Dr. W.W. Lin, Dr. W.C. Chen, Dr. J.Y. Chen, Mr. K.A. Chiu, Mr. Y.S. Shih, Ms. Y.C. Chen, Ms. P.Y. Lin, and L.L. Wei for serving my experimental supports and their precious suggestions to my study. I would like to thanks to all my lab members for their friendship and help.

Most importantly, I wish to thank my entire family like to dedicate this work to my family. I especially thank my husband for his endless love and supports throughout my life. Most of all, I wish to thank my 9-month old daughter for giving me so much happiness, confidence, and motivation in every single day of my life.

I would like to thank everybody who was important to the successful realization of thesis, as well as expressing my apology that I could not mention personally one by one.

The financial support of my Ph. D research work by a grant from the NCTU and NSC, Taiwan, ROC is gratefully acknowledged.

Contents

Abstract (in Chinese)-----	I
Abstract (in English)-----	III
Acknowledgements-----	V
Contents -----	VI
Abbreviations -----	IX
Table Captions-----	XI
Figure Captions-----	XII
Chapter 1: Introduction -----	1
1.1. Background-----	1
1.1.1. Structure and properties-----	1
1.1.2. Applications-----	8
1.1.3. Film growth-----	8
1.2. Motivation-----	9
1.3. Structure of thesis-----	10
References-----	12
Chapter 2: Epitaxial growth of titanium oxynitride and titanium oxynitride films on MgO substrate -----	19
2.1. Introduction-----	19
2.2. Experimental-----	21
2.2.1. Pulsed laser deposition system-----	21
2.2.2. Experimental flowcharts and deposition parameters and material analysis methods-----	21
2.2.3. Instruments-----	24
2.2.3.1. X-ray photoelectron spectroscopy-----	24
2.2.3.2. X-ray diffraction (XRD)-----	25
2.2.3.3. Transmission electron microscopy (TEM)-----	27
2.2.3.4. Atomic Force Microscopy (AFM)-----	29
2.2.3.5. Electrical conductivity measurement-----	30
2.3. Structure and properties of epitaxial TiN_xO_y films on MgO (001) substrates-----	30
2.3.1. Chemical composition-----	30
2.3.2. Microstructure -----	34
2.3.3. Determination of the strain/stress tensors in the epitaxial $\text{TiN}_x\text{O}_y/\text{MgO}$	

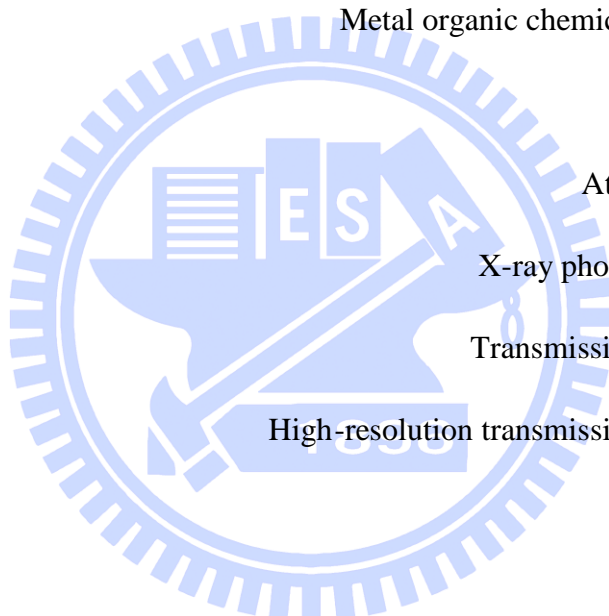
layers by x-ray diffraction-----	42
2.3.4. Surface morphology-----	52
2.3.5. Electronic properties-----	52
2.4. Structure and properties of epitaxial TiC_xO_y films on MgO (001) substrates----	53
2.4.1. Chemical composition-----	53
2.4.2. Microstructure-----	56
2.4.3. Determination of the strain/stress tensors in the epitaxial $\text{TiC}_x\text{O}_y/\text{MgO}$ layers by x-ray diffraction-----	61
2.4.4. Surface morphology-----	62
2.4.5. Electronic properties-----	63
2.5. Summary-----	63
References-----	65
Chapter 3: Nanoindentation studies of epitaxial TiN_xO_y (001) and TiC_xO_y (001) films on MgO (001)-----	69
3.1. Introduction-----	69
3.2. The theory of nanoindentation-----	69
3.3. Substrate effects and the limitation of conventional Oliver-Pharr method-----	71
3.4. Li and Vlassak model-----	73
3.5. Application of Li and Vlassak model for determining hardness and Young's modulus of epitaxial TiN_xO_y and TiC_xO_y films grown on MgO (001) substrate--	75
3.5.1. Experimental -----	75
3.5.2. Results and discussions-----	76
A. $\text{TiN}_x\text{O}_y/\text{MgO}$ -----	76
B. $\text{TiC}_x\text{O}_y/\text{MgO}$ -----	84
3.7. Summary-----	87
References-----	88
Chapter 4: Stability and etching of TiN_xO_y in hydrogen microwave plasma-----	91
4.1. Introduction-----	91
4.2. Experimental-----	91
4.3. Stability and etching of TiN_xO_y : morphology and mechanism-----	92
4.4. Summary-----	103
References-----	104
Chapter 5: Conclusions and future works-----	105
5.1. Conclusions-----	105

5.2. Future works-----	106
Appendix A-----	108
Appendix B-----	111
List of publications-----	118
Autobiography-----	119



Abbreviations

TiN	Titanium nitride
TiC	Titanium carbide
TiN _x O _y	Titanium oxynitride
TiC _x O _y	Titanium oxycarbide
CVD	Chemical vapor deposition
PLD	Pulsed laser deposition
MOCVD	Metal organic chemical vapor deposition
MgO	Magnesium oxide
AFM	Atomic force microscopy
XPS	X-ray photoelectron spectroscopy
TEM	Transmission electron microscopy
HRTEM	High-resolution transmission electron microscopy
XRD	X-ray diffraction
Ar	Argon
nm	nanometer
cm	centimeter
eV	electron volt
FWHM	Full width at half maximum
RSM	Reciprocal space maps
XRR	X-ray reflectivity
MPCVD	Microwave plasma chemical vapor deposition



H

Hardness

E

Young's modulus



Table Captions

Table 1.1: Structural and thermal, electrical, and mechanical properties of TiN, TiC, TiO, and MgO-----	3
Table 2.1: Deposition parameters for titanium oxynitride films by the PLD method-----	23
Table 2.2: Deposition parameters for titanium oxycarbide films by the PLD method-----	23
Table 2.3: Chemical composition, thickness, in-plane a , out-of plane c , and relaxed a_o lattice parameters, FWHM of (002) TiN_xO_y , in-plane residual strain ε_{\parallel} and stress σ_{\parallel} , and critical thickness h_c of TiN_xO_y films-----	35
Table 2.4: XRD measured and calculated strains in 5 $[hkl]$ directions for the $\text{TiN}_{1.11}\text{O}_{0.10}$ film-----	45
Table 2.5: XRD measured and calculated strains in 5 $[hkl]$ directions for the $\text{TiN}_{0.97}\text{O}_{0.23}$ film-----	46
Table 2.6: XRD measured and calculated strains in 5 $[hkl]$ directions for the $\text{TiN}_{0.81}\text{O}_{0.38}$ film -----	46
Table 2.7: XRD measured and calculated strains in 5 $[hkl]$ directions for the $\text{TiN}_{0.63}\text{O}_{0.55}$ film -----	47
Table 2.8: The principal stress σ_1 , σ_2 , and σ_3 , maximum shear stress τ_{max} , and the critical shear stress τ_{crit} [2.22] of TiN_xO_y films-----	51
Table 2.9: XRD measured and calculated strains in 5 $[hkl]$ directions for the $\text{TiC}_{0.47}\text{O}_{0.69}$ film-----	61
Table 2.10: The principal stress σ_1 , σ_2 , and σ_3 , and maximum shear stress τ_{max} of the $\text{TiC}_{0.47}\text{O}_{0.69}$ film-----	62
Table 3.1: The hardness and Young's modulus of TiN_xO_y films calculated by using Li-Vlassak method -----	77
Table 3.2: The hardness and Young's modulus of $\text{TiC}_{0.47}\text{O}_{0.69}$ film calculated by using Li-Vlassak method-----	85
Table 4.1: Hydrogen plasma treatment parameters -----	92

Figure Captions

Figure 1.1: NaCl structure of TiN, TiC, and TiO-----	2
Figure 1.2: Calculated Ti–C phase diagram [1.15]-----	4
Figure 1.3: Calculated Ti–N phase diagram [1.16]-----	4
Figure 1.4: Calculated Ti–O phase diagram [1.18]-----	5
Figure 1.5: Pseudoternary phase diagram of the TiN-TiC-TiO system at 1100 °C (from Neumann <i>et al.</i> [1.28]). The cell parameters a_o of Ti(C,N,O) are indicated. The lines separate zones of similar a_o -----	6
Figure 1.6: Structure of a) TiN, b) TiC, c) TiN _x O _y , and d) TiC _x O _y viewing from [001] direction. TiN _x O _y and TiC _x O _y structures are made by substituting oxygen atoms for nitrogen and carbon atom, respectively-----	7
Figure 2.1: The PLD process-----	20
Figure 2.2: A schematic view of the PLD system-----	21
Figure 2.3: Experimental flowcharts of deposition and characterization of epitaxial of titanium oxynitride and titanium oxycarbide films on MgO (001) substrate-----	22
Figure 2.4: X-ray a) symmetric scan, b) asymmetric scan, and c) skew-symmetric scan techniques-----	26
Figure 2.5: Ewald sphere constructions and the diffraction patterns for one intense diffraction spot with a) Kikuchi line runs exactly through its corresponding spot \mathbf{g} ($s = 0$), and b) the excess Kikuchi line lies outside its corresponding diffraction spot \mathbf{g} ($s > 0$)-----	28
Figure 2.6: $3\mathbf{g}$ condition for the WBDF image. The \mathbf{g} reflection is in the optical axis with a large excitation error-----	29
Figure 2.7: XPS depth profiles for sample a) A, b) B, c) C and d) D with different oxygen content -----	31
Figure 2.8: XPS spectra for Ti-2p of samples A, B, C and D after Ar sputtering for one minute. The spectra are deconvoluted into components of titanium nitride, titanium oxynitride, and titanium dioxide.-----	32
Figure 2.9: XPS spectra for N-1s of samples A, B, C and D after Ar sputtering for one minute. The spectra are deconvoluted into components of titanium nitride and titanium oxynitride-----	33

Figure 2.10: XPS spectra for O-1s of samples A, B, C and D after Ar sputtering for one minute. The spectra are deconvoluted into components of titanium oxynitride and titanium dioxide-----	34
Figure 2.11: XRD 2 θ - θ scans for four TiN _x O _y films -----	36
Figure 2.12: High-resolution XRD 2 θ - θ scans for epitaxial TiN _x O _y films with different chemical composition deposited on MgO substrates -----	36
Figure 2.13: XRD ϕ -scan of {022} reflections for TiN _x O _y films grown on MgO substrate, showing epitaxial relationship between the film and the substrate is TiN _x O _y (001)//MgO(001) and TiN _x O _y [100]/MgO[100] -----	37
Figure 2.14: Reciprocal space maps of the asymmetric (113) MgO and (113) TiN _x O _y reflections with different composition of a) TiN _{1.1} O _{0.10} , b) TiN _{0.97} O _{0.23} , c) TiN _{0.81} O _{0.38} and d) TiN _{0.63} O _{0.55} -----	38
Figure 2.15: X-ray reflectivity curve for the four TiN _x O _y films -----	40
Figure 2.16: Cross-sectional HRTEM images of a) sample A and b) sample B along [100] zone axis showing sharp and smooth interfaces between TiN _x O _y and MgO (indicated by arrows). No misfit dislocations at the interfaces can be observed over the range of 12-14 nm -----	41
Figure 2.17: a) Cross-sectional TEM image of sample A in [100] bright-field and the corresponding diffraction pattern at the film/substrate interface. Cross-sectional bright-field TEM images of sample A under two-beam condition of b) $g = 002$ and c) $g = 022$ -----	42
Figure 2.18: Definition of the coordinate system for the specimen S_i and the laboratory system L_i . The incident beam, the diffracted beam, and the normal to the diffracting planes L_3 are in the same plane. The sample can be rotated on the diffractometer in ϕ and in ψ . S_3 is normal to the sample surface, and S_1 and S_2 are in the sample surface-----	43
Figure 2.19: Coordinate settings-----	44
Figure 2.20: Mohr's circles for a three-dimensional state of stress-----	49
Figure 2.21: The maximum shear stresses τ_{max} acting on the plane that bisects the angle between the planes in which the maximum σ_1 and minimum σ_3 principal stresses act -----	51
Figure 2.22: AFM images of TiN _x O _y surface for a) sample A, b) sample B, c) sample C, and d) sample D-----	53

Figure 2.23: XPS spectra for (a) C-1s, (b) Ti-2p, and (c) O-1s, as a function of Ar sputtering time -----	55
Figure 2.24: XPS depth profile for TiC_xO_y film deposited on MgO-----	56
Figure 2.25: XRD (a) 2θ - θ scan and (b) ω -scan for $\text{TiC}_{0.47}\text{O}_{0.69}$ film deposited on MgO (001)-----	57
Figure 2.26: XRD ϕ -scan of {022} planes for $\text{TiC}_{0.47}\text{O}_{0.69}$ film on MgO (001) substrate, showing that epitaxial relationship between the film and the substrate is $\text{TiCO}(001)//\text{MgO}(001)$ and $\text{TiCO}[100]//\text{MgO}[100]$ -----	58
Figure 2.27: X-ray reflectivity curve for the deposited $\text{TiC}_{0.47}\text{O}_{0.69}$ film -----	58
Figure 2.28: Reciprocal space map of the asymmetric (113) for $\text{TiC}_{0.47}\text{O}_{0.69}$ film on MgO-----	59
Figure 2.29: Cross-sectional HRTEM image along [100] zone axis showing a sharp interface between $\text{TiC}_{0.47}\text{O}_{0.69}$ and MgO. No misfit dislocations are observed at the interface over the range of 15 nm -----	60
Figure 2.30: AFM image of $\text{TiC}_{0.47}\text{O}_{0.69}$ film surface -----	63
Figure 3.1: (a) A typical load-displacement curve and (b) the deformation pattern of an elastic-plastic sample during and after indentation -----	71
Figure 3.2: Schematic diagrams of a) sink-in (hard films/soft substrates) and b) pile-up (soft films/hard substrates) indentations -----	72
Figure 3.3: Contour plot of $\log_{10}(\chi^2)$ as a function of E_f and η for the $\text{TiN}_x\text{O}_y/\text{MgO}$ sample. The unit of χ^2 is in nm^2 -----	78
Figure 3.4: The Young's modulus of TiN_xO_y films as a function of h/t (indentation depth/film thickness) obtained by using Li-Vlassak method, together with the Young's modulus of MgO substrate. The results obtained using Oliver-Pharr method are presented for comparison-----	80
Figure 3.5: The hardness of TiN_xO_y films as a function of indentation depth calculated by using both Li-Vlassak and Oliver-Pharr methods. The hardness value of MgO substrate is also included-----	81
Figure 3.6: The dependence of the hardness and Young's modulus of TiN_xO_y films on chemical composition-----	82
Figure 3.7: Evolution of the DOS of the titanium oxynitrides (NaCl structure) with the composition [3.23]-----	83
Figure 3.8: Evolution of the hardness and Young's modulus of TiN_xO_y films with	

residual compressive stress -----84

Figure 3.9: Contour plot of $\log_{10}(\chi^2)$ as a function of E_f and η for the $\text{TiC}_{0.47}\text{O}_{0.69}/\text{MgO}$ sample. The unit of χ^2 is in nm^2 -----85

Figure 3.10: The hardness of $\text{TiC}_{0.47}\text{O}_{0.69}$ film as a function of indentation depth calculated by using both Li-Vlassak and Oliver-Pharr methods. The hardness value of MgO substrate is also included-----86

Figure 3.11: The Young's modulus of $\text{TiC}_{0.47}\text{O}_{0.69}$ film as a function of h/t (indentation depth/film thickness) obtained by using Li-Vlassak method, together with the Young's modulus of MgO substrate. The results obtained using Oliver-Pharr method are presented for comparison-----87

Figure 4.1: AFM images of (a) as-grown TiN_xO_y films and (b) TiN_xO_y film after hydrogen plasma treatment at pressure of 40 Torr for 90 min (sample 1)----94

Figure 4.2: AFM images of TiN_xO_y after etching at (a) 60 Torr for 30 min (sample 2), 80 Torr for (b) 30 min (sample 3) and (c) 60 min (sample 4); (d) cross-sectional SEM image of TiN_xO_y after etching at 80 Torr for 150 min (sample 5)-----95

Figure 4.3: The distribution of the etch size and etch depth at (a) 60 Torr for 30 min, 80 Torr for (b) 30 min, (c) 60 min, and (d) 150 min-----96

Figure 4.4: XPS depth profiles for (a) as-grown TiN_xO_y film and (b) sample 1-----99

Figure 4.5: High-resolution XPS spectra for (a) Ti-2p and (b) O-1s as function of Ar sputtering time of as-grown TiN_xO_y and sample 1. The spectra were deconvoluted into components using Voigt curve fitting-----100

Figure 4.6: XRD 2θ - θ scans for (a) as-grown TiN_xO_y and (b) sample 1. The corresponding XRD ω -scan of (002) TiN_xO_y is displayed in the inset-----102

Figure 4.7: X-ray reflectivity curves for TiN_xO_y films before and after treatment at 40 Torr for 90 min-----102

Chapter 1

Introduction

1.1. Background

1.1.1. Structure and properties

Titanium nitride (TiN), titanium carbide (TiC), and titanium monoxide TiO belong to the class of so-called refractory metal compounds. They are all known as hard materials and crystallize in rock salt NaCl structure with close lattice constants [1.1]. Figure 1.1 shows the structure of TiN, TiC, and TiO. Generally, titanium compounds have high melting points and extreme hardness such as covalent crystals and they also have interesting optical, electronic, catalytic and magnetic properties. Table 1.1 presents the structure, and thermal, electrical, and mechanical properties of TiN, TiO, and TiC. Among those compounds, TiN and TiC possess many similarities in physical properties such as excellent electrical and thermal conductivity, low coefficient of friction, and high corrosion and oxidation resistance [1.1].

In terms of chemical bonding, TiN_x , TiC_x , and TiO_x are found to exist not only in the stoichiometric ($x = 1$) form, but also in the nonstoichiometric form with $x < 1$ (substoichiometric form) and $x > 1$ (overstoichiometric form) [1.2-6]. Those compounds can exist in wide composition ranges while still retain their NaCl cubic structure ($0.6 < x < 1.2$ for TiN_x [1.7-9], $0.48 < x < 1$ [1.10, 11] for TiC_x , and $0.51 < x < 1.26$ for TiO_x [1.12, 13]); and the composition have strong effects on properties of those titanium compounds. In TiO_x structure, 10 – 15 % vacancies are found at both Ti and O lattice sites [1.12, 13], while only vacancies in C sublattices are reported in TiC_x structure [1.10, 11]. In substoichiometric TiN_x structure, the main point defects are N vacancies, while overstoichiometric TiN_x structure contains both Ti vacancies and N interstitials [1.9].

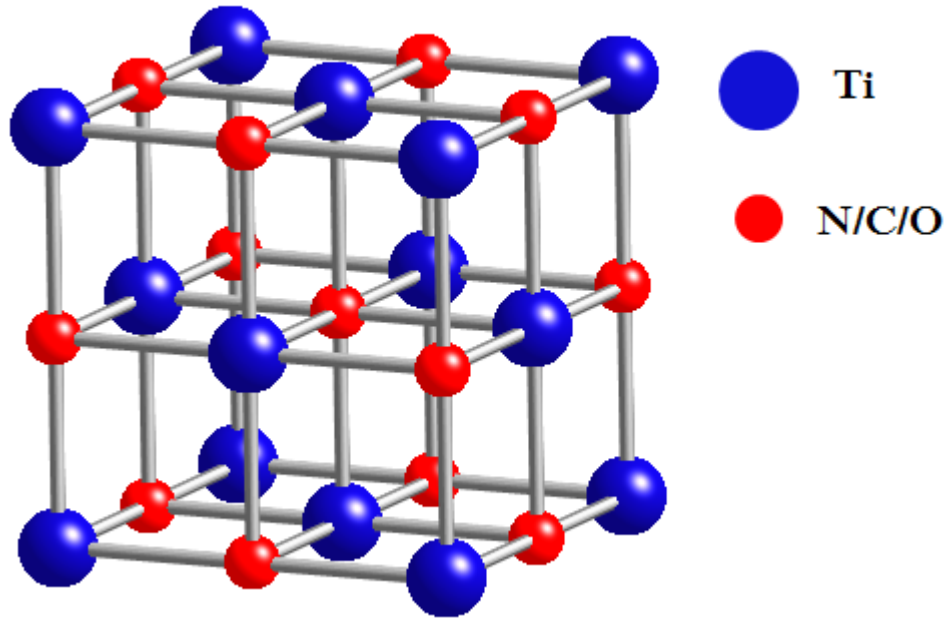


Figure 1.1: NaCl structure of TiN, TiC, and TiO.

Figure 1.2 shows the Ti-C phase diagram from the most recent assessment by Frisk using Calphad method [1.14, 15]. In these works the δ phase is treated as a solution phase and modeled with a two-sublattice model, $(\text{Ti})_1(\text{C}, \text{Va})_1$, where Ti completely occupies one sublattice and C partially occupies the other, thus leaving vacancies Va. Carbon and vacancies form a solid solution on the second sublattice and any ordering at low temperature is ignored in the model. Both α -Ti (HCP) and β -Ti (BCC) have low solubility of carbon. At low carbon content the δ -TiC_x phase boundary is quite steep, which hints that the phase field is limited by the formation of an almost stoichiometric (fixed composition) compound. Figure 1.3 shows the Ti-N phase diagram [1.14, 16] also using Calphad method. Compared to the Ti-C phase diagram in Fig. 1.2, both the α -Ti and β -Ti phases dissolve much more nitrogen than carbon. The δ -TiN_x phase is similar to the δ -TiC_x phase and δ -TiN_x is usually modeled in the same way as the carbide phase. The δ -TiN_x phase field is wider than the phase field of δ -TiC_x and, moreover, an ordered phase, ϵ -Ti₂N, having the anti-rutile structure [1.17] appears at low temperature. Figure 1.4 shows the Ti-O phase diagram assessed by Lee [1.18].

Table 1.1: Structural and thermal, electrical, and mechanical properties of TiN, TiC, TiO, and MgO.

	Titanium nitride TiN	Titanium carbide TiC	Titanium monoxide TiO	Magnesium oxide MgO
Structure	NaCl	NaCl	NaCl	NaCl
Lattice constant	4.2417 Å (PDF 38-1420)	4.317 Å (PDF 89-3828)	4.1770 Å (PDF 8-117)	4.211 (PDF 89-4248)
Density	5.22 g/cm ³ [1.1, 19]	4.93 g/cm ³ [1.1]	4.95 g/cm ³ [1.20]	3.58 g/cm ³
Melting point	2930 °C [1.1, 19]	3160 °C [1.1]	1750 °C [1.20]	2852 °C
Thermal conductivity	19.2 W.m ⁻¹ .K ⁻¹ [1.1, 19]	17.14 - 30.93 W.m ⁻¹ .K ⁻¹ [1.21]	-	5 - 60 W.m ⁻¹ .K ⁻¹
Thermal expansion coefficient	$9.35 \times 10^{-6} \text{ K}^{-1}$ [1.1, 19]	$4.1 \times 10^{-6} \text{ K}^{-1}$ [1.21]	-	$13 \times 10^{-6} \text{ K}^{-1}$ [1.22]
Vickers hardness	18-21 GPa [1.1, 19]	26 - 31 GPa [1.21, 23]	-	10 GPa [1.24, 25]
Modulus of elasticity	533 GPa for [002] 416 GPa for [111] [1.26]	439 GPa [1.21] [1.23]	400 GPa [1.13]	300 GPa [1.24, 25]
Electrical resistivity	21.7 μΩ·cm [1.27]	55 μΩ·cm [1.28]	190 μΩ·cm [1.29]	-

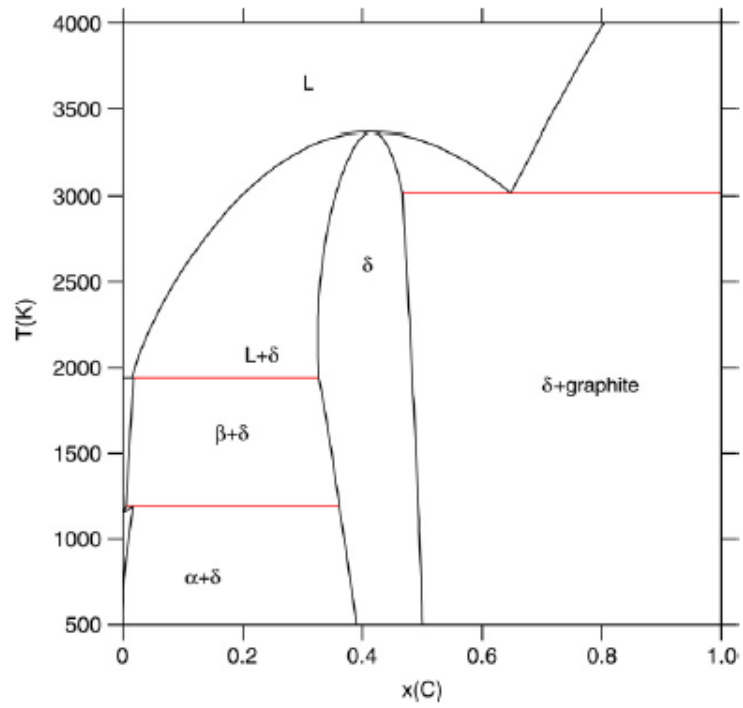


Figure 1.2: Calculated Ti-C phase diagram [1.15].

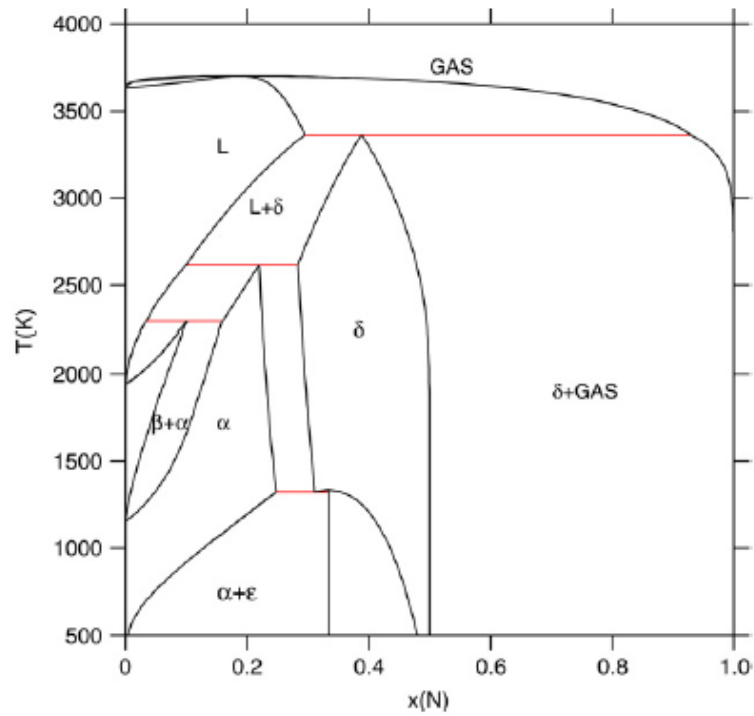


Figure 1.3: Calculated Ti-N phase diagram [1.16].

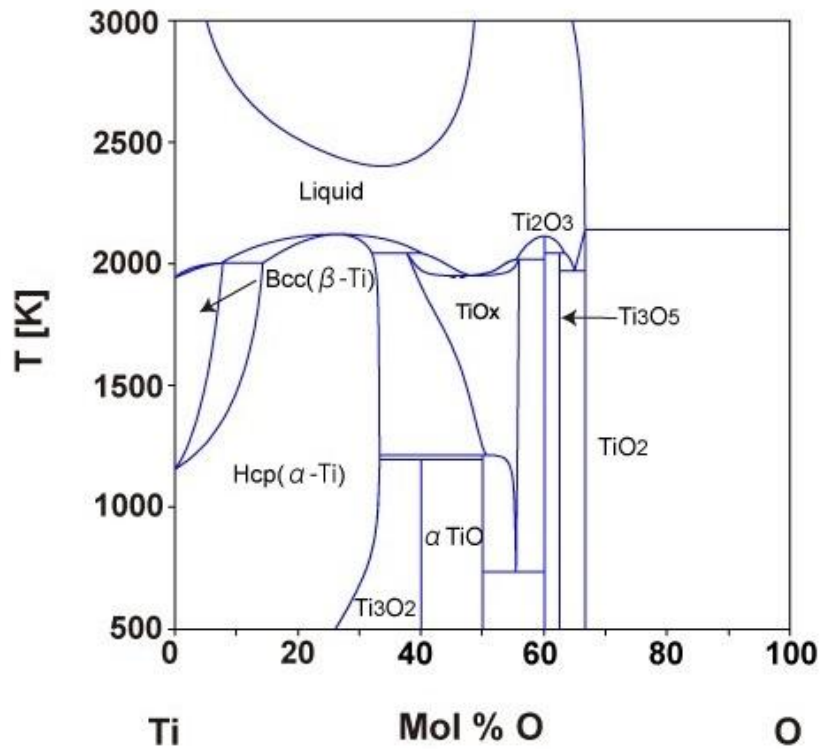


Figure 1.4: Calculated Ti-O phase diagram [1.18].

It is noticed that the group IV B metals such as titanium present pseudoternary systems of the type “TiO - TiN - TiC” [1.30]. This system shows substitutional solid solutions including “TiN-TiO”, “TiC-TiO”, and “TiN-TiC”, which correspond to extensive monophasic zones. The solid solutions, named $\text{Ti}(\text{N,C,O})$ have the same cubic crystalline structure with that of TiN, TiC and TiO phases. The unit-cell parameter a_o of $\text{Ti}(\text{N,C,O})$ phase depends on the TiC, TiO and TiN content. Figure 1.5 shows the pseudoternary phase diagram “TiO-TiN-TiC” proposed by Neumann *et al.* [1.31]. The monophasic zone covers the whole diagram at temperatures higher than 1100 °C. This zone corresponds to the $\text{Ti}(\text{C,N,O})$ phase. The cell parameter a_o varies between 4.12 Å and 4.32 Å. The monophasic zones cover in part of the TiN-TiO and TiC-TiO axes in this system. Thus, the subsystems “TiN-TiO” and “TiC-TiO” present titanium oxynitride $\text{Ti}(\text{N,O})$ and titanium oxycarbide $\text{Ti}(\text{C,O})$, respectively. These oxynitride and oxycarbide have the same cubic structure of $\text{Ti}(\text{N,C,O})$ with a_o depending on TiN, TiC, and TiO content. The binary systems $\text{Ti}(\text{N,O})$ and $\text{Ti}(\text{C,O})$ have recently attracted many attentions. As stated above, TiN_x , TiC_x , and TiO_x generally exist in nonstoichiometric forms, and therefore titanium oxynitride and titanium oxycarbide have always found to exist in

nonstoichiometric form of TiN_xO_y and TiC_xO_y (with $y \leq 1 - x$ or $y \geq 1 - x$) instead of $\text{TiN}_x\text{O}_{1-x}$ and $\text{TiC}_x\text{O}_{1-x}$, respectively. Due to the fact that oxygen has high reactivity with titanium, TiN_xO_y and TiC_xO_y are usually formed by the addition of oxygen to the TiN and TiC matrix, in which oxygen replaces nitrogen and carbon sublattice. This process can be carried out through the oxidation of TiN and TiC, or simultaneous mixing of elements or precursors methods [1.32-36]. Figure 1.6 shows the structure of TiN, TiC, TiN_xO_y , and TiC_xO_y , in which TiN_xO_y and TiC_xO_y are formed by the oxygen replacement for nitrogen and carbon. It is noticed that Ti(N,O) and Ti(C,O) benefit from many remarkable properties of both metallic oxides (chemical stability, optical properties) and nitrides/carbides (hardness, wear resistance); and the optical, electrical, and mechanical properties of TiN_xO_y and TiC_xO_y can be tailored between those of metallic nitrides/carbides and those of corresponding ionic oxides by varying the oxygen content [1.33, 37-39].

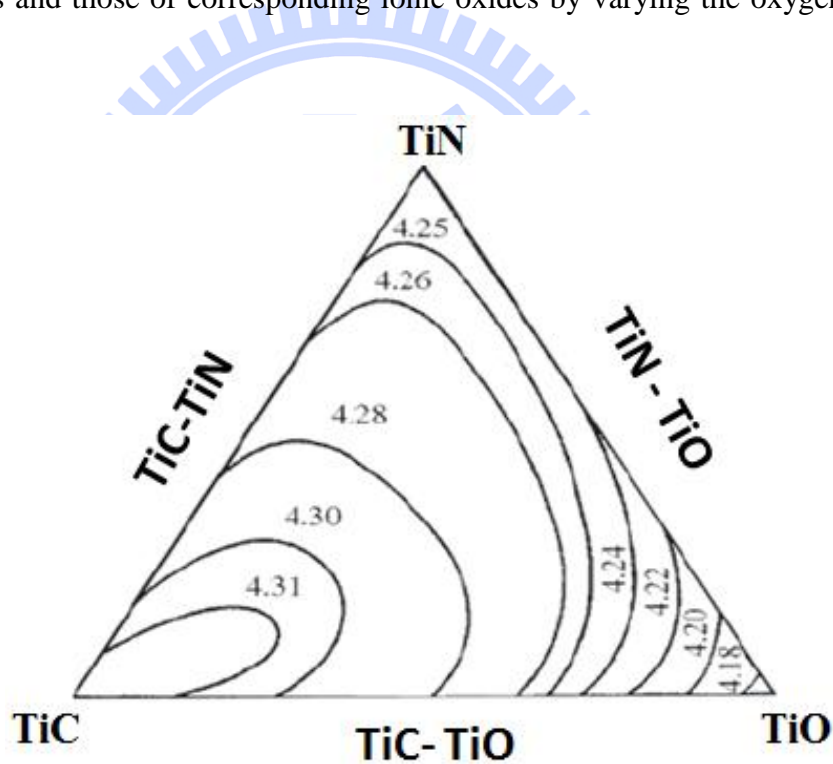


Figure 1.5: Ternary phase diagram of the TiN-TiC-TiO system at 1100 °C (from Neumann *et al.* [1.31]). The cell parameters a_o of Ti(C,N,O) are indicated. The lines separate zones of similar a_o .

It has shown that TiN_xO_y and TiC_xO_y still retains their NaCl crystal structure with a wide range of x and y [1.40, 41]). Therefore, similar to TiN and TiC, the slip systems in

TiN_xO_y and TiC_xO_y are mainly $1/2\langle 110 \rangle$ {110}, and may also be {100}, {111}, and {112} [1.42]. The substitution of oxygen for nitrogen/carbon atoms could result in the changes in their structures as well as electronic structure and mechanical properties. Indeed, TiN and TiC contain both covalent and ionic bonding. The changes in oxygen and nitrogen/carbon content result in changes of covalent and ionic contribution to the bond in the TiN_xO_y and TiC_xO_y compounds. This is due to the difference in valence electrons of carbon (four valence electrons), nitride (five valence electrons), and oxygen (six valence electrons) [1.41, 43] that can result in the change of overlapping of atomic orbital.

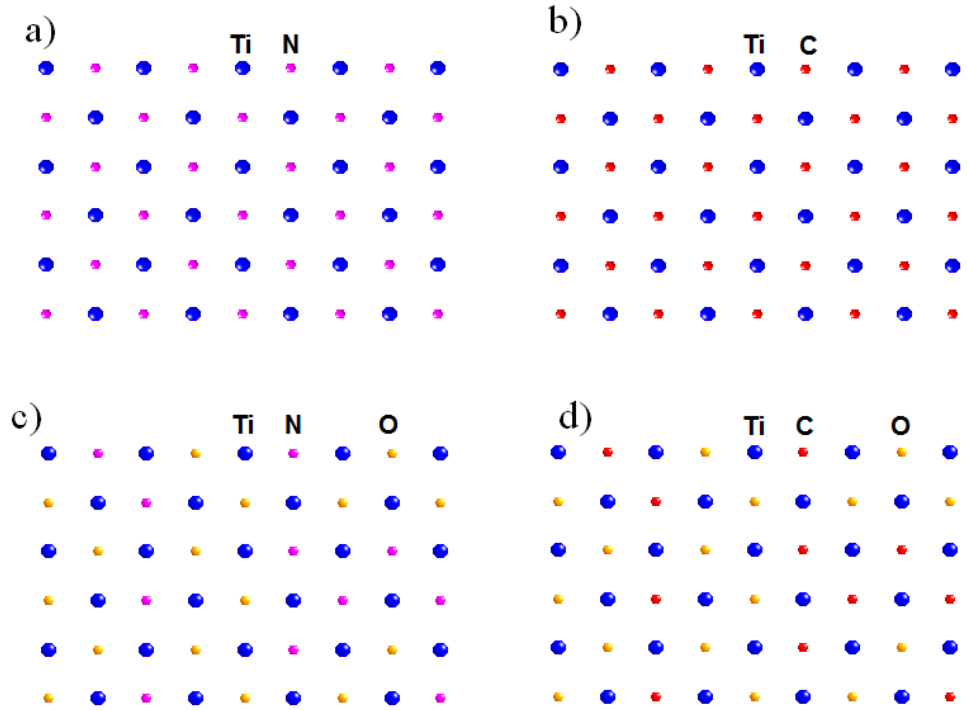


Figure 1.6: Structure of a) TiN, b) TiC, c) TiN_xO_y , and d) TiC_xO_y viewing from [001] direction. TiN_xO_y and TiC_xO_y structures are made by substituting oxygen atoms for nitrogen and carbon atom, respectively.

Magnesium oxide (MgO) is also one of the most important materials used in the manufacturing of refractories. MgO is an insulator, and it is very chemically and physically stable at high temperature that is similar to TiC, TiN, and TiO. The physical and mechanical properties of MgO are shown in Table 1.1. MgO also has NaCl structure and its lattice constant is very close to those of TiC, TiN, and TiO. Therefore, MgO has

been widely used as substrate for the deposition of high-quality TiN, TiC, TiN_xO_y , and TiC_xO_y films.

1.1.2. Applications

Titanium oxynitride and titanium oxycarbide possess many interesting properties of both titanium nitride/carbide and titanium oxide. Therefore, those compounds have been widely used in a wide range of applications such as decorative and wear-resistant coating, and electronic devices [1.33, 37-39, 44]. Owing to excellent optical properties, titanium oxynitride has been used transparent IR window electrodes [1.37], solar collector devices [1.34, 37], electrical switchable windows [1.45], and photocatalysis [1.46]. In comparison with TiN, titanium oxynitride has shown new interesting properties that can be used as biomaterials [1.47, 48], memory devices [1.49]. In addition, titanium oxynitride nanocrystals with NaCl (rock-salt) structure especially show ultraviolet light emission in photoluminescence spectra at room temperature contrasted with TiN case [1.50].

1.2.3. Film growth

TiN films have been widely grown by pulsed laser deposition (PLD) and magnetron sputtering on various substrates such as MgO, Si, glasses, and stainless steels [1.51-64]. A large amount of scientific works about the deposition of polycrystalline [1.51-55] and epitaxial [1.56-64] TiN films have been reported. Epitaxial TiN has been successfully grown on MgO [1.56, 57, 59, 62] and Si [1.58, 60, 61, 63, 64] substrates. The best quality of epitaxial TiN films on MgO was reported in ref. [1.59], in which the full width at half maximum (FWHM) of the TiN(200) peak in ω -rocking curve scan was found to be 0.13° . In case of epitaxial TiN on Si substrate, the best quality was found in ref. [1.58], in which the FWHM the TiN (200) reflection is 0.47° .

TiC films have been grown by various processes such as chemical vapor deposition (CVD), pulsed laser deposition (PLD), magnetron sputtering, and evaporation on various substrates such as MgO, Si, graphite, and stainless steels [1.65-73]. Similarly to TiN, there have been many reports on polycrystalline [1.65-68] and epitaxial [1.69-72] TiC films. Epitaxial TiC films were found to be widely deposited on MgO [1.70-72], 6H-SiC [1.69], and Si [1.73] substrates. The best quality of epitaxial TiC with FWHM was found to be 0.63° on MgO [1.72], and 2.5° on Si [1.73].

TiN_xO_y films have been deposited by various processes, including oxidation of TiN [1.32], nitridation of TiO₂ [1.74], and simultaneous mixing of elements or precursors methods such as magnetron sputtering [1.33], evaporation [1.34], metal organic chemical vapor deposition (MOCVD) [1.35], and pulsed laser deposition (PLD) [1.36]. Similarly, most of TiC_xO_y films have been grown by chemical vapor deposition (CVD) and magnetron sputtering [1.38, 39, 75-78]. In those processes, both TiN_xO_y and TiC_xO_y films usually grown on various substrates such as Si, glass, and steel. In most cases, however, TiN_xO_y and TiC_xO_y films have been reported to be amorphous or polycrystalline. There is the fact that epitaxial growth of TiN_xO_y and TiC_xO_y films has been rarely studied in contrast with the case of TiN and TiC. To our best knowledge, there are no reports on the epitaxial TiN_xO_y and TiC_xO_y films, and no bulk and single crystal TiN_xO_y and TiC_xO_y are available.

1.2. Motivation

Titanium oxynitride and titanium oxycarbide are of relatively new compositions. Therefore, they still need many works and characterizations to explore an accomplished knowledge on their properties. One of the most interesting properties is the effects of oxygen on structure, electrical and mechanical properties of TiN_xO_y and TiC_xO_y. In fact, there have been large amounts of scientific studies on the optical and electrical properties, and chemical compositions of titanium oxynitride and titanium oxycarbide. However, most of those studies focused on polycrystalline TiN_xO_y and TiC_xO_y films in contrast with epitaxial TiN_xO_y and TiC_xO_y films that has been rarely reported. This is due to the fact that TiN_xO_y and TiC_xO_y are very hard materials and are difficult to synthesize in bulk by several common deposition methods such as chemical vapor deposition (CVD), magnetron sputtering, and evaporation. Moreover, in order to obtain high-quality, especially epitaxial TiN_xO_y and TiC_xO_y films, those methods require a relatively high substrate temperature which may lead to serious problems for many applications. For hard materials such as TiN, TiC, TiN_xO_y and TiC_xO_y, mechanical properties are very important. The difficulty in deposition of epitaxial TiN_xO_y and TiC_xO_y also limited the chance to study mechanical properties of TiN_xO_y and TiC_xO_y due to the fact that mechanical properties depend on not only chemical composition but also microstructure, whereas microstructure of polycrystalline TiN_xO_y and TiC_xO_y films varies widely and is often uncharacterized. The deposition of epitaxial TiN_xO_y also can improve electrical conductivity and overcome the problem of fast grain boundary diffusion of dopants and

impurities along the columnar grains of the polycrystalline films [1.79-82]. Furthermore, study of epitaxial films can improve our understanding of basic properties of TiN_xO_y and TiC_xO_y . Growth of epitaxial TiN_xO_y and TiC_xO_y films is also helpful for etching study due to it can avoid the complicated etch effects from grain boundaries and orientations in polycrystalline films.

TiN , TiC , TiN_xO_y and TiC_xO_y films have been widely applied in hydrogen environment; but there is still a lack of understanding about the effect of hydrogen on those materials. Furthermore, studying the etching of those materials by pure hydrogen plasma could be helpful for the first understanding about the role of hydrogen in the patterning process using plasma containing atomic hydrogen such as Cl_2/CHF_3 , $\text{Cl}_2/\text{Ar}/\text{CHF}_3$, $\text{Cl}_2/\text{N}_2/\text{CHF}_3$, Ar/CHF_3 , and CH_4/H_2 [1.83, 84]. Moreover, hydrogen plasma treatment can be applied to the revelation of dislocation etch pits in TiN , TiC , TiN_xO_y and TiC_xO_y .

This thesis reports the successful growth of epitaxial titanium oxynitride and titanium oxycarbide films on MgO (001) substrates using pulsed laser deposition. The crystallinity, microstructure, chemical composition, and morphology of titanium oxynitride and titanium oxycarbide were investigated. The effect of oxygen on the lattice parameter, microstructure, electrical, and mechanical properties of TiN_xO_y was especially investigated. Mechanical properties of TiN_xO_y films were characterized by using nanoindentation. The nanoindentation data was then analyzed and simulated to exclude the substrate effect and then extract the accurate hardness and Young's modulus of the films. The study of the effects of hydrogen microwave plasma on the stability and etching of titanium oxynitride films as function of gas pressure and treating time was also studied.

1.3. Structure of the thesis

The thesis consists of five chapters and is organized as follows: Chapter 2 presents experimental methods and procedures for growth of epitaxial TiN_xO_y and TiC_xO_y on MgO (001) substrates; surface morphology, chemical composition, microstructure, and electrical properties of TiN_xO_y and TiC_xO_y are also described. Chapter 3 shows the nanoindentation studies of epitaxial TiN_xO_y and TiC_xO_y films including the basic theory of nanoindentation, models to solve substrate effects, experimental procedures, and results. Chapter 4 shows the stability and etching of TiN_xO_y depending on the hydrogen

plasma treatment conditions. Finally, Chapter 5 presents conclusions of the present study as well as the future works.



References

- [1.1] H.O. Pierson, Handbook of Refractory Carbides and Nitrides: Properties, Characteristics, Processing and Applications, Noyes Publication, Westwood, New Jersey, USA, 1996.
- [1.2] A. Czyzniewski, W. Pecht, Deposition and some properties of nanocrystalline, nanocomposite and amorphous carbon-based coatings for tribological applications, J Mater Process Tech, 157 (2004) 274-283.
- [1.3] S.H. Jhi, S.G. Louie, M.L. Cohen, J. Ihm, Vacancy hardening and softening in transition metal carbides and nitrides, Phys Rev Lett, 86 (2001) 3348-3351.
- [1.4] A. Mani, P. Aubert, F. Mercier, H. Khodja, C. Berthier, P. Houdy, Effects of residual stress on the mechanical and structural properties of TiC thin films grown by RF sputtering, Surf Coat Tech, 194 (2005) 190-195.
- [1.5] W. Pecht, A. Czyzniewski, Deposition and some properties of carbide/amorphous carbon nanocomposites for tribological application, Surf Coat Tech, 174 (2003) 979-983.
- [1.6] K.E. Tan, A.M. Bratkovsky, R.M. Harris, A.P. Horsfield, D. NguyenManh, D.G. Pettifor, A.P. Sutton, Carbon vacancies in titanium carbide, Model Simul Mater Sc, 5 (1997) 187-198.
- [1.7] P.E. Schmid, M.S. Sunaga, F. Levy, Optical and electronic properties of sputtered TiN_x thin films, J Vac Sci Technol A, 16 (1998) 2870-2875.
- [1.8] J.H. Kang, K.J. Kim, Structural, optical, and electronic properties of cubic TiN_x compounds, J Appl Phys, 86 (1999) 346-350.
- [1.9] P. Patsalas, S. Logothetidis, Optical, electronic, and transport properties of nanocrystalline titanium nitride thin films, J Appl Phys, 90 (2001) 4725-4734.
- [1.10] V.N. Lipatnikov, A.I. Gusev, Dependence of the resistivity of nonstoichiometric titanium carbide TiC_y on the density and distribution of carbon vacancies, Jap J Appl Phys, 38 (1999) 294-300.
- [1.11] V.N. Lipatnikov, A. Kottar, L.V. Zueva, A.I. Gusev, Ordering effects in nonstoichiometric titanium carbide, Inorg Mater, 36 (2000) 155-161.
- [1.12] S.R. Barman, D.D. Sarma, Electronic-Structure of TiO_x (0.8 < x < 1.3) with disordered and ordered vacancies, Phys Rev B, 49 (1994) 16141-16148.
- [1.13] Y.O. Ciftci, Y. Unlu, K. Colakoglu, E. Deligoz, The structural, thermodynamical and elastic properties of TiO, Phys Scripta, 80 (2009) 025601.

- [1.14] D.A. Andersson, P.A. Korzhavyi, B. Johansson, First-principles based calculation of binary and multicomponent phase diagrams for titanium carbonitride, *Calphad*, 32 (2008) 543-565.
- [1.15] K. Frisk, A revised thermodynamic description of the Ti-C system, *Calphad*, 27 (2003) 367-373.
- [1.16] S. Jonsson, *Z. Metallkd.*, 87 (1996) 691–702.
- [1.17] E. Etchessahar, J.P. Bars, J. Debuigne, The Ti-N system - Equilibrium between the delta-phase, epsilon-phase and alpha-phase and the conditions of formation of the Lobier and Marcon metastable phase, *J Less-Common Met*, 134 (1987) 123-139.
- [1.18] B.-J. Lee, N. Saunders, Thermodynamic evaluation of the Ti-Al-O ternary system, *Z. Metallkd.*, 88 (1997) 152-161.
- [1.19] D.S. Stone, K.B. Yoder, W.D. Sproul, Hardness and elastic-modulus of TiN based on continuous indentation technique and new correlation, *J Vac Sci Technol A*, 9 (1991) 2543-2547.
- [1.20] N. Greenwood, A. Earnshaw, *Chemistry of the Elements*, Butterworth-Heinemann, 1997.
- [1.21] J.F. Shackelford, W. Alexander, *CRC Materials Science and Engineering Handbook*, Taylor & Francis, 2010.
- [1.22] C.S. Shin, D. Gall, N. Hellgren, J. Patscheider, I. Petrov, J.E. Greene, Vacancy hardening in single-crystal $\text{TiN}_x(001)$ layers, *J Appl Phys*, 93 (2003) 6025-6028.
- [1.23] P.C. Kong, B. Pfender, *Carbide, Nitride and Boride Materials Synthesis and Processing*, Chapman and Hall, London, 1997.
- [1.24] D. Caceres, I. Vergara, R. Gonzalez, Y. Chen, E. Alves, Nanoindentation on MgO crystals implanted with lithium ions, *Nucl Instrum Meth B*, 191 (2002) 154-157.
- [1.25] K. Kurosaki, D. Setoyama, J.J. Matsunaga, S. Yamanaka, Nanoindentation tests for TiO_2 , MgO, and YSZ single crystals, *J Alloy Compd*, 386 (2005) 261-264.
- [1.26] S. Nagao, K. Nordlund, R. Nowak, Anisotropic elasticity of IVB transition-metal mononitrides determined by ab initio calculations, *Phys Rev B*, 73 (2006) 144113.
- [1.27] R.C. Weast, *Handbook of Chemistry and Physics*, CRC Press, Boca Raton, FL, 1990.
- [1.28] P. Ettymayer, W. Lengauer, *Carbides: Transition Metal Solid State Chemistry*, Wiley, 1994.
- [1.29] C.N.R. Rao, W.E. Wahnsiedler, J.M. Honig, Plasma resonance in TiO, VO and NbO, *J Solid State Chem*, 2 (1970) 315-317.

- [1.30] A.D. Mazzonia, M.S. Conconib, Synthesis of group IVB metals oxycarbides by carboreduction reactions, *Materials Research*, 5 (2002) 459-466.
- [1.31] G. Neumann, R. Kieffer, P. Ettmayer, Über das System TiC-TiN-TiO, *Monatshefte für Chemie*, 103 (1972) 1130-1137.
- [1.32] J. Graciani, J.F. Sanz, T. Asaki, K. Nakamura, J.A. Rodriguez, Interaction of oxygen with TiN(001): N \leftrightarrow O exchange and oxidation process, *J Chem Phys*, 126 (2007) 244713.
- [1.33] F. Vaz, P. Cerqueira, L. Rebouta, S.M.C. Nascimento, E. Alves, P. Goudeau, J.E. Riviere, Preparation of magnetron sputtered TiN_xO_y thin films, *Surf Coat Tech*, 174 (2003) 197-203.
- [1.34] M. Lazarov, P. Raths, H. Metzger, W. Spirk, Optical-constants and film density of TiN_xO_y solar selective absorbers, *J Appl Phys*, 77 (1995) 2133-2137.
- [1.35] F. Maury, F.D. Duminica, TiO_xN_y coatings grown by atmospheric pressure metal organic chemical vapor deposition, *Surf Coat Tech*, 205 (2010) 1287-1293.
- [1.36] Y. Suda, H. Kawasaki, T. Ueda, T. Ohshima, Preparation of high quality nitrogen doped TiO₂ thin film as a photocatalyst using a pulsed laser deposition method, *Thin Solid Films*, 453 (2004) 162-166.
- [1.37] M. Braic, M. Balaceanu, A. Vladescu, A. Kiss, V. Braic, G. Epurescu, G. Dinescu, A. Moldovan, R. Birjega, M. Dinescu, Preparation and characterization of titanium oxy-nitride thin films, *Appl Surf Sci*, 253 (2007) 8210-8214.
- [1.38] A.C. Fernandes, P. Carvalho, F. Vaz, S. Lanceros-Mendez, A.V. Machado, N.M.G. Parreira, J.F. Pierson, N. Martin, Property change in multifunctional TiC_xO_y thin films: Effect of the O/Ti ratio, *Thin Solid Films*, 515 (2006) 866-871.
- [1.39] L. Marques, H.M. Pinto, A.C. Fernandes, O. Banakh, F.V.M.M.D. Ramos, Optical properties of titanium oxycarbide thin film, *Appl Surf Sci*, 255 (2009) 5615-5619.
- [1.40] A. Afir, M. Achour, N. Saoula, X-ray diffraction study of Ti-O-C system at high temperature and in a continuous vacuum, *J Alloy Compd*, 288 (1999) 124-140.
- [1.41] J. Graciani, S. Hamad, J.F. Sanz, Changing the physical and chemical properties of titanium oxynitrides TiN_{1-x}O_x by changing the composition, *Phys Rev B*, 80 (2009) 184112-184122.
- [1.42] D. Hull, D.J. Bacon, *Introduction to dislocations*, Butterworth-Heinemann, 2011.
- [1.43] L. Karlsson, L. Hultman, M.P. Johansson, J.E. Sundgren, H. Ljungcrantz, Growth, microstructure, and mechanical properties of arc evaporated TiC_xN_{1-x} (0 ≤ x ≤ 1) films, *Surf Coat Tech*, 126 (2000) 1-14.

- [1.44] D. Munteanu, R. Cozma, B. Borcea, F. Vaz, The influence of oxygen flow on the tribological behaviour and residual stress of TiCO thin-films, *J Optoelectron Adv M*, 8 (2006) 712-715.
- [1.45] Y. Saito, M. Hirata, H. Tada, M. Hyodo, Electrically switchable window using a suspension of TiO_xN_y particles, *Applied Physics Letters*, 63 (1993) 1319-1321.
- [1.46] R. Asahi, T. Morikawa, T. Ohwaki, K. Aoki, Y. Taga, Visible-light photocatalysis in nitrogen-doped titanium oxides, *Science*, 293 (2001) 269-271.
- [1.47] Y.X. Leng, P. Yang, J.Y. Chen, H. Sun, J. Wang, G.J. Wang, N. Huang, X.B. Tian, P.K. Chu, Fabrication of Ti-O/Ti-N duplex coatings on biomedical titanium alloys by metal plasma immersion ion implantation and reactive plasma nitriding/oxidation, *Surf Coat Tech*, 138 (2001) 296-300.
- [1.48] R.J. Koerner, L.A. Butterworth, I.V. Mayer, R. Dasbach, H.J. Busscher, Bacterial adhesion to titanium-oxy-nitride (TiNOX) coatings with different resistivities: a novel approach for the development of biomaterials, *Biomaterials*, 23 (2002) 2835-2840.
- [1.49] D.-H. Kang, D.-H. Ahn, M.-H. Kwon, H.-S. Kwon, K.-B. Kim, K.S. Lee, B.-k. Cheong, Lower voltage operation of a phase change memory device with a highly resistive TiON layer, *Japanese Journal of Applied Physics*, 43 (2004) 5243-5244.
- [1.50] X.G. Yang, C. Li, B.J. Yang, W. Wang, Y.T. Qian, Optical properties of titanium oxynitride nanocrystals synthesized via a thermal liquid-solid metathesis reaction, *Chem Phys Lett*, 383 (2004) 502-506.
- [1.51] N. Biunno, J. Narayan, S.K. Hofmeister, A.R. Srivatsa, R.K. Singh, Low-temperature processing of titanium nitride films by laser physical vapor-deposition, *Applied Physics Letters*, 54 (1989) 1519-1521.
- [1.52] V. Craciun, D. Craciun, C. Ghica, L. Trupina, C. Flueraru, N. Nastase, Growth of thin transparent titanium nitride layers by reactive laser ablation, *Appl Surf Sci*, 138 (1999) 593-598.
- [1.53] H.D. Gu, K.M. Leung, C.Y. Chung, X.D. Han, Room-temperature growth of high-purity titanium nitride by laser ablation of titanium in a nitrogen atmosphere, *Surf Coat Tech*, 110 (1998) 153-157.
- [1.54] J.H. Huang, K.W. Lau, G.P. Yu, Effect of nitrogen flow rate on structure and properties of nanocrystalline TiN thin films produced by unbalanced magnetron sputtering, *Surf Coat Tech*, 191 (2005) 17-24.

- [1.55] J.M. Lackner, W. Waldhauser, R. Berghauser, R. Ebner, B. Major, T. Schoberl, Structural, mechanical and tribological investigations of pulsed laser deposited titanium nitride coatings, *Thin Solid Films*, 453 (2004) 195-202.
- [1.56] N. Biunno, J. Narayan, A.R. Srivatsa, O.W. Holland, Laser deposition of epitaxial titanium nitride films on (100) MgO, *Applied Physics Letters*, 55 (1989) 405-407.
- [1.57] J. Bottiger, J. Chevallier, J.H. Petersen, N. Schell, W. Matz, A. Mucklich, Observation of the growth mode of TiN during magnetron sputtering using synchrotron radiation, *J Appl Phys*, 91 (2002) 5429-5433.
- [1.58] R. Chowdhury, X. Chen, J. Narayan, Pulsed-laser deposition of epitaxial Si/TiN/Si(100) heterostructures, *Applied Physics Letters*, 64 (1994) 1236-1238.
- [1.59] T. Lee, H. Seo, H. Hwang, B. Howe, S. Kodambaka, J.E. Greene, I. Petrov, Fully strained low-temperature epitaxy of TiN/MgO(001) layers using high-flux, low-energy ion irradiation during reactive magnetron sputter deposition, *Thin Solid Films*, 518 (2010) 5169-5172.
- [1.60] W.J. Meng, G.L. Eesley, Growth and mechanical anisotropy of TiN thin films, *Thin Solid Films*, 271 (1995) 108-116.
- [1.61] J. Narayan, P. Tiwari, X. Chen, J. Singh, R. Chowdhury, T. Zheleva, Epitaxial growth of TiN Films on (100) silicon substrates by laser physical vapor deposition, *Applied Physics Letters*, 61 (1992) 1290-1292.
- [1.62] N. Pryds, D. Cockburn, K. Rodrigo, I.L. Rasmussen, J. Knudsen, J. Schou, Growth of thin films of TiN on MgO(100) monitored by high-pressure RHEED, *Appl Phys a-Mater*, 93 (2008) 705-710.
- [1.63] P. Tiwari, T. Zheleva, J. Narayan, Epitaxial growth of TiN Films on (100) silicon substrates by laser physical vapor deposition, *Laser Ablation in Materials Processing : Fundamentals and Applications*, 285 (1993) 349-354.
- [1.64] T. Zheleva, K. Jagannadham, J. Narayan, Epitaxial growth in large-lattice-mismatch systems, *J Appl Phys*, 75 (1994) 860-871.
- [1.65] G. Leggieri, A. Luches, M. Martino, A. Perrone, G. Majni, P. Mengucci, I.N. Mihailescu, Laser reactive ablation deposition of titanium carbide films, *Thin Solid Films*, 258 (1995) 40-45.
- [1.66] P. Lin, C. Deshpandey, H.J. Doerr, R.F. Bunshah, N. Kaufherr, R. Nielsen, G. Fenske, Detailed characterization of TiC and TiN coatings prepared by the activated reactive evaporation process, *J Vac Sci Technol A*, 5 (1987) 2732-2736.

- [1.67] Y. Suda, H. Kawasaki, K. Doi, S. Hiraishi, Formation and properties of TiC thin films by pulsed Nd/YAG laser deposition, *Thin Solid Films*, 374 (2000) 282-286.
- [1.68] J.K. Tang, J.S. Zabinski, J.E. Bultman, TiC coatings prepared by pulsed laser deposition and magnetron sputtering, *Surf Coat Tech*, 91 (1997) 69-73.
- [1.69] A.K. Chaddha, J.D. Parsons, G.B. Kruaval, Thermally stable, low specific resistance ($130 \times 10^{-5} \Omega\text{cm}^2$) TiC ohmic contacts to n-type 6H α -SiC, *Applied Physics Letters*, 66 (1995) 760-762.
- [1.70] H. Hogberg, J. Birch, M.P. Johansson, U. Jansson, L. Hultman, Strain relaxation of low-temperature deposited epitaxial titanium-carbide films, *J Cryst Growth*, 219 (2000) 237-244.
- [1.71] L. Norin, H. Hogberg, J. Lu, U. Jansson, J.O. Malm, Deposition of transition metal carbide superlattices using C₆₀ as a carbon source, *Applied Physics Letters*, 73 (1998) 2754-2756.
- [1.72] L. Norin, S. McGinnis, U. Jansson, J.O. Carlsson, Low temperature deposition of epitaxial titanium carbide on MgO(001) by co-evaporation of C₆₀ and Ti, *J Vac Sci Technol A*, 15 (1997) 3082-3085.
- [1.73] W.H. Sheu, S.T. Wu, Epitaxial growth of TiC (002) on Si (001) by reactive magnetron sputtering at low temperatures, *Jpn J Appl Phys* 1, 37 (1998) 6094-6097.
- [1.74] O. Diwald, T.L. Thompson, T. Zubkov, E.G. Goralski, S.D. Walck, J.T. Yates, Photochemical activity of nitrogen-doped rutile TiO₂(111) in visible light, *J Phys Chem B*, 108 (2004) 6004-6008.
- [1.75] G. Georgiev, N. Feschiev, D. Popov, Z. Uzunov, Titanium carbide thin-films obtained by reactive magnetron sputtering, *Vacuum*, 36 (1986) 595-597.
- [1.76] J.E. Sundgren, B.O. Johansson, S.E. Karlsson, Mechanisms of reactive sputtering of titanium nitride and titanium carbide. 1. Influence of process parameters on film composition, *Thin Solid Films*, 105 (1983) 353-366.
- [1.77] A.C. Fernandes, P. Carvalho, F. Vaz, N.M.G. Parreira, P. Goudeau, E. Le Bourhis, J.P. Riviere, Correlation between processing and properties of titanium oxycarbide, TiC_xO_y, thin films, *Plasma Process Polym*, 4 (2007) S83-S88.
- [1.78] A.C. Fernandes, L. Cunha, C. Moura, F. Vaz, P. Carvalho, E. Le Bourhis, P. Goudeau, J.P. Riviere, N.M.G. Parreira, The effect of bombarding conditions on the properties of multifunctional Ti-C-O thin films grown by magnetron sputtering, *Surf Coat Tech*, 202 (2007) 946-951.

- [1.79] N. Kumar, M.G. Fissel, K. Pourrezaei, B. Lee, E.C. Douglas, Growth and properties of TiN and TiO_xN_y diffusion-barriers in silicon on sapphire integrated-circuits, *Thin Solid Films*, 153 (1987) 287-301.
- [1.80] W. Sinke, G.P.A. Frijilink, F.W. Saris, Oxygen in titanium nitride diffusion-barriers, *Applied Physics Letters*, 47 (1985) 471-473.
- [1.81] N. Kumar, J.T. McGinn, K. Pourrezaei, B. Lee, E.C. Douglas, Transmission electron-microscopy studies of brown and golden titanium nitride thin-films as diffusion-barriers in very large-scale integrated-circuits, *J Vac Sci Technol A*, 6 (1988) 1602-1608.
- [1.82] R. Chowdhury, R.D. Vispute, K. Jagannadham, J. Narayan, Characteristics of titanium nitride films grown by pulsed laser deposition, *J Mater Res*, 11 (1996) 1458-1469.
- [1.83] S.C. Abraham, C.T. Gabriel, J. Zheng, Performance of different etch chemistries on titanium nitride antireflective coating layers and related selectivity and microloading improvements for submicron geometries obtained with a high-density metal etcher, *J Vac Sci Technol A*, 15 (1997) 702-706.
- [1.84] J. Tonotani, T. Iwamoto, F. Sato, K. Hattori, S. Ohmi, H. Iwai, Dry etching characteristics of TiN film using Ar/CHF_3 , Ar/Cl_2 , and Ar/BCl_3 gas chemistries in an inductively coupled plasma, *J Vac Sci Technol B*, 21 (2003) 2163-2168.

Chapter 2

Epitaxial growth of titanium oxynitride and titanium oxycarbide films on MgO substrate

2.1. Introduction

Titanium oxynitride and titanium oxycarbide films have been deposited by many methods such as CVD, MOCVD, magnetron sputtering, evaporation, and PLD. Among those methods, PLD has been widely used over the past decade and has been considered as an attractive alternative for the deposition of high-quality thin films because of its unique advantages. The main advantages of PLD are [2.1]:

- (i) Conceptually simple: a laser beam vaporizes a target surface, producing a film with the same composition as the target.
- (ii) Non-volatile targets
- (iii) Multi-component target.
- (iv) Multi-target or multi-layer or alloy films.
- (v) Operated under any ambient gas over a broad range of gas pressure (from 0 – 1 Torr).
- (vi) Easy of thickness control.
- (vii) Generally of lower substrate temperature.
- (viii) Cost-effective: one laser can serve many vacuum systems.
- (ix) Fast: high quality samples can be grown reliably in 10 or 15 minutes.
- (x) Scalable: as complex oxides move toward volume production.

As shown in Fig. 2.1, the PLD process consists of three regimes:

- (i) Regime I: Laser-target interaction.
- (ii) Regime II: Target to substrate gas phase transportation.
- (iii) Regime III: Deposition and film growth process.

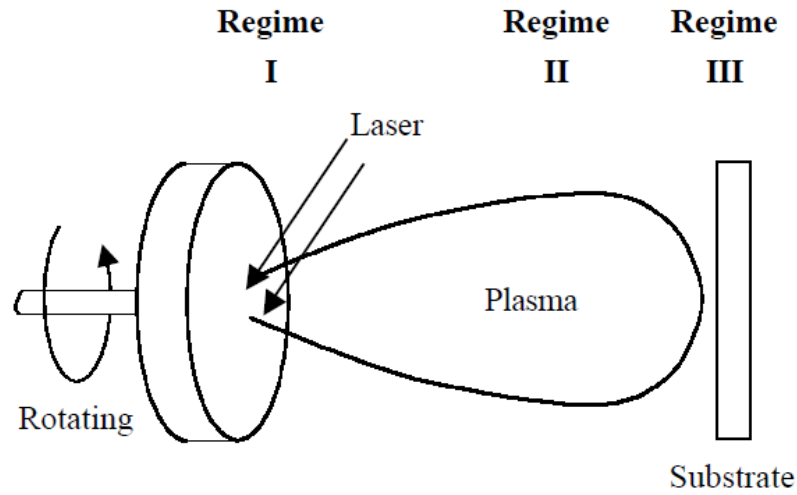


Figure 2.1: The PLD process.

The regime II of gas transportation contains high ion/neutral ratio and many ionized species with high kinetic energy (about 10-100 eV). Therefore, PLD is particularly capable of deposition of many materials that are difficult to synthesize in bulk and by other deposition methods such as ceramics (YBCO, PZT, SBN), complex oxides, hard materials (including diamond/diamond like films, TiN, TiC, TiN_xO_y , TiC_xO_y , SiC...), and exotic alloys and multi-component films (Fe_{16}N_2 , $\text{La}_{1-x}\text{Sr}_x\text{MnO}_3$). The film's structure and growth mechanism are strictly related to the conditions of plasma obtained by the interaction between targets and laser beam. Authors in ref. [2.2] have shown that in the plume produced from TiC targets, there is the presence of a large amount of ions with high kinetic energy including Ti^+ , Ti^{2+} , and C^+ ions. The neutral Ti was also obtained in the TiC plasma plume. In case of pulsed laser deposition of TiN by the irradiation Ti target in nitrogen gas, the plasma plume contains high-density of reactive species and high-energy ions such as Ti and Ti^+ , Ti^{2+} , N^+ , and N^{2+} [2.3, 4].

In this chapter, we present the detailed description of the experimental procedures for epitaxial growth of titanium oxynitride and titanium oxycarbide films on MgO (001) substrate using PLD. The crystallinity, microstructure, chemical composition, and morphology of titanium oxynitride and titanium oxycarbide are also studied. The effect of oxygen on the lattice parameter, microstructure, and electrical properties of TiN_xO_y was especially investigated. The residual strain and stress tensors of TiN_xO_y and TiC_xO_y films were also calculated.

2.2. Experimental

2.2.1. Pulsed laser deposition system

The deposition of titanium oxynitride and titanium oxycarbide films was carried out in a PLD system. The base pressure in this PLD system can reach 1×10^{-6} Torr. Figure 2.2 presents a schematic view of the PLD system. The basic structure of the PLD system consists of the following parts:

- (i) The substrate stage can be heated up to 700°C .
- (ii) A 2-inch target is placed opposite to a substrate stage at a distance of 14 cm. The target can be rotated to avoid pitting during deposition.
- (iii) KrF ($\lambda = 248 \text{ nm}$) laser beam is incident at an angle of 45° with respect to the target.
- (iv) The PLD reactor chamber is made of stainless steel to sustain high temperature and pressure.

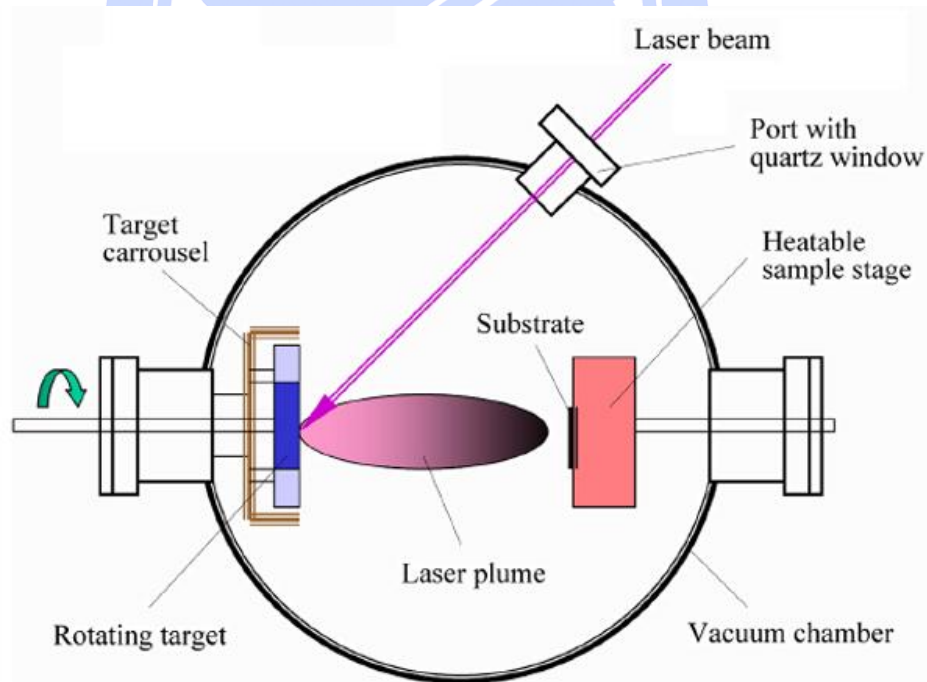


Figure 2.2: A schematic view of the PLD system.

2.2.2. Experimental flowcharts and parameters and material analysis methods

Figure 2.3 shows the experimental flowcharts of deposition and characterization of epitaxial of titanium oxynitride and titanium oxycarbide films on MgO (001) substrates. Before titanium oxynitride and titanium oxycarbide films deposition, MgO substrates were heat-treated at 700°C for 30 minutes to obtain a smooth and clean surface. To obtain TiN_xO_y films with different chemical composition, a $\text{TiNO}_{0.064}$ target was used, and the deposition process was carried out under base pressure of 1×10^{-6} Torr and under nitrogen ambient gas of 10^{-3} - 10^{-5} Torr. Detailed deposition parameters are shown in Table 2.1. A $\text{TiCO}_{0.5}$ target was used to deposit TiC_xO_y films, and deposition parameters for the TiC_xO_y films are showed in Table 2.2. After the deposition process had been completed, the substrate was cooled down to room temperature in 90 minutes.

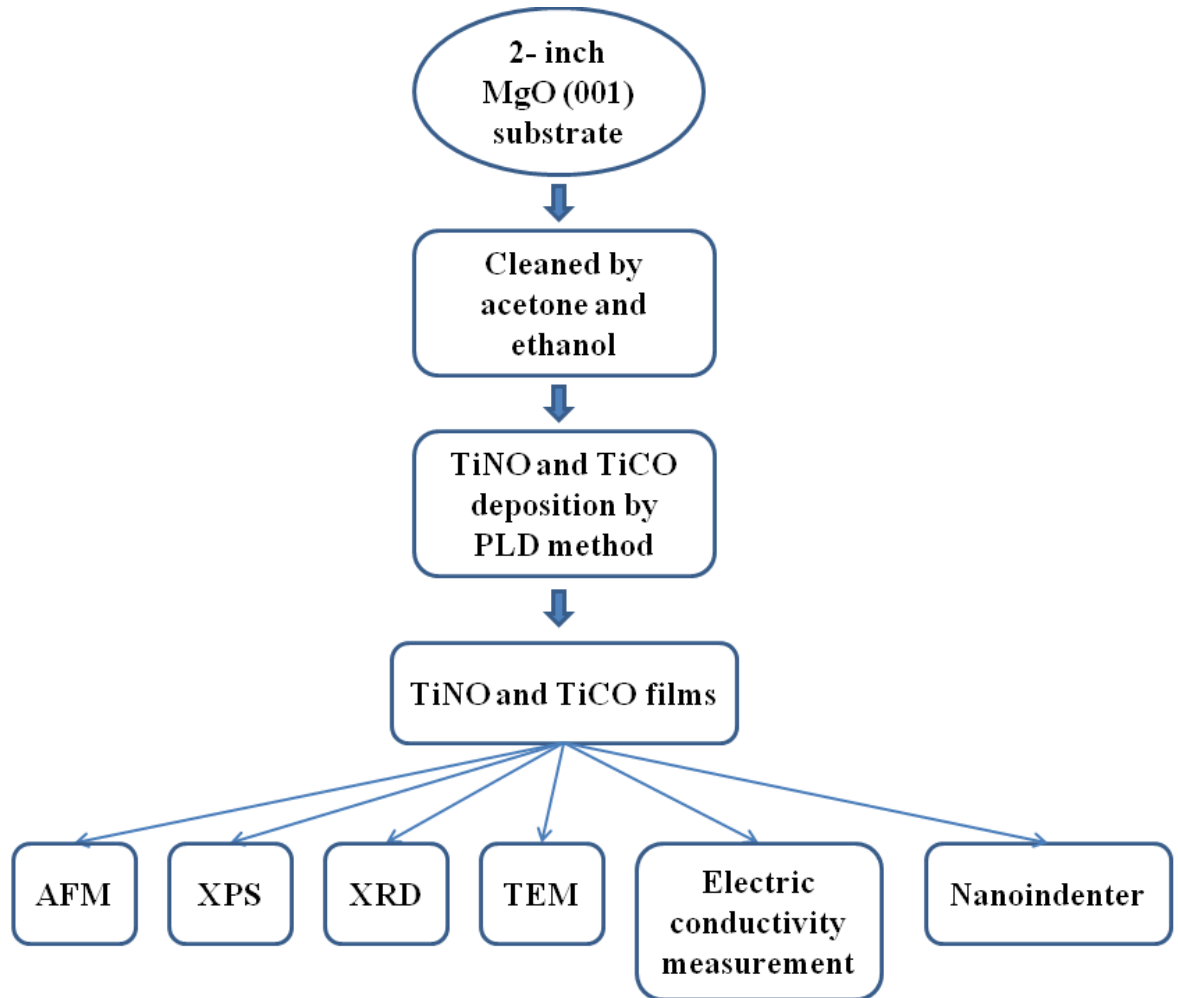


Figure 2.3: Experimental flowcharts of deposition and characterization of epitaxial of titanium oxynitride and titanium oxycarbide films on MgO (001) substrate.

Table 2.1: Deposition parameters for titanium oxynitride films by the PLD method.

Sample	A	B	C	D
Base Pressure (Torr)	1×10^{-6}	1×10^{-6}	1×10^{-6}	1×10^{-6}
Substrate-target distance (cm)	14	14	7	7
Substrate temperature	700° C	700° C	700° C	700° C
Nitrogen flowing gas	No	Yes	Yes	Yes
Working pressure (Torr)	1×10^{-6}	1×10^{-5}	1×10^{-4}	5×10^{-3}
Pulse repetition rate (Hz)	5	5	5	5
Time (min)	180	120	180	180

Table 2.2: Deposition parameters for titanium oxycarbide films by the PLD method.

Sample	1
Base Pressure (Torr)	1×10^{-6}
Substrate-target distance (cm)	14
Substrate temperature	700° C
Working pressure (Torr)	1×10^{-6}
Pulse repetition rate (Hz)	5
Time (min)	120

The deposited films were then analyzed by atomic force microscopy (AFM), x-ray photoelectron spectroscopy (XPS), x-ray diffraction pattern (XRD), transmission electron microscopy, Hall measurements, and nanoindenter. The results of nanoindentation as well as data analysis will be presented in Chapter 3.

2.2.3. Instruments:

2.2.3.1. X-ray photoelectron spectroscopy

X-ray photoelectron spectroscopy (XPS) is one of the most powerful techniques used in the surface, interface and thin film analysis. Of all the presently available instrumental techniques for surface analysis, XPS can generally do quantitative analysis with readily interpretable and the informative results of chemical analysis.

In an XPS experiment, the sample is irradiated by low energy X-rays in an ultra high vacuum environment. This causes photo-ionisation of the atoms at the specimen's surface: photoelectrons are emitted from the atomic energy levels with very specific Binding Energies and, consequently, with a very accurate spectral signature/fingerprint for all the elements from the Periodic Table and their chemical compounds. Quantitative data can be obtained from peak heights or peak areas. The quantitative sensitivity is in the range of (10^{-2} - 10^{-4}) of a monolayer and the surface sensitivity is in the range of (2-100) monolayers (<0.5 - 20nm). From the results of this analysis, it is possible to infer which elements are present on the specimen, what their chemical states are (due to chemical shifts of the binding energy of the electron shells), and in what quantities they are present. The following quantitative results are obtained with errors <10% (and <5% for using well known standards): element relative concentrations, oxidation states relative concentrations, and chemical states relative concentrations.

In general, the basis advantages of XPS are:

- (i) Nondestructive
- (ii) Surface sensitive (100 Å)
- (iii) Elemental sensitive
- (iv) All elements (except for hydrogen and helium)
- (v) Quantitative
- (vi) Chemical bonding information
- (vii) High information content

In this study, XPS was used to analyze the chemical composition of the deposited films and chemical states of titanium, nitrogen, carbon, and oxygen. XPS analyses were formed on a PHI Quantera SXM (ULVAC-PHI) system with monochromatic Al K α radiation source. Argon ion with ion energy of 5keV was used for sputter profiling. For XPS quantitative analysis, the peak area was corrected with relative sensitivity factors from manufacture's program and database. The spectra were deconvoluted into components using Voigt curve fitting.

2.2.3.2. X-ray diffraction (XRD)

X-ray diffraction (XRD) is a very important experimental technique that has long been used to address all issues related to the crystal structure of solids, including lattice constants, identification of unknown materials, orientation of single crystals, and ect. The Bede D1 system is a versatile high resolution X-ray diffractometer for the characterization of advanced materials. The system is most suitable for characterization of thin films, superlattices, and single crystal wafers, although it can also characterize other forms of materials. A range of parameters can be measured including thickness, composition, relaxation, strain, area uniformity, density, roughness, phase, crystalline texture, crystallinity, pore size and grain size.

In this study, a Bede D1 high-resolution x-ray diffractometer, equipped with two two-bounce Si 220 channel-cut collimator crystals (CCC), a dual channel Si 220 analyser crystal, and CuK $_{\alpha 1}$ radiation ($\lambda = 1.5406 \text{ \AA}$), was used to investigate the crystallinity, microstructure, and to calculate the strain/stress tensors of the films. Since CuK $_{\beta}$ ($\lambda = 1.39 \text{ \AA}$) is also radiated from x-ray tube with Cu target, a Ni filter is used to eliminate the XRD peaks caused by the CuK $_{\beta}$. A symmetric 2θ - θ scan is used to determine the d-spacing of the planes parallel to the sample surface [see Fig. 2.4a]. In this type of scan, the angle θ of the incoming beam with respect to the sample surface is varied, while simultaneously keeping the detector at an angle of 2θ with respect to the incoming beam. The angle θ at which a diffraction peak is observed, can then used to give the interplanar distance by using Bragg law. In order to determine the d-spacing of a set of planes that are tilted by an angle with respect to the sample surface, an asymmetric θ - 2θ scan can be performed [see Fig. 2.4b]. As in the case of a symmetric scan, the detector is placed at an angle of 2θ with respect to the incoming beam. The incoming beam, however, makes an angle of ω with respect to the sample surface. Note that $\omega = \theta - \psi$, where is ψ the angle between

sample surface and the measured plane. An alternative to the asymmetric scan method is the skew-symmetric measuring geometry [Fig. 2.4c)]. As in the case of the symmetric scan, the incoming beam forms an angle θ with respect to the sample surface, while the detector is put at 2θ . The difference is that the sample is tilted over a fixed angle ψ around the axis that is parallel to the sample surface and the plane of the incoming and outgoing beam.

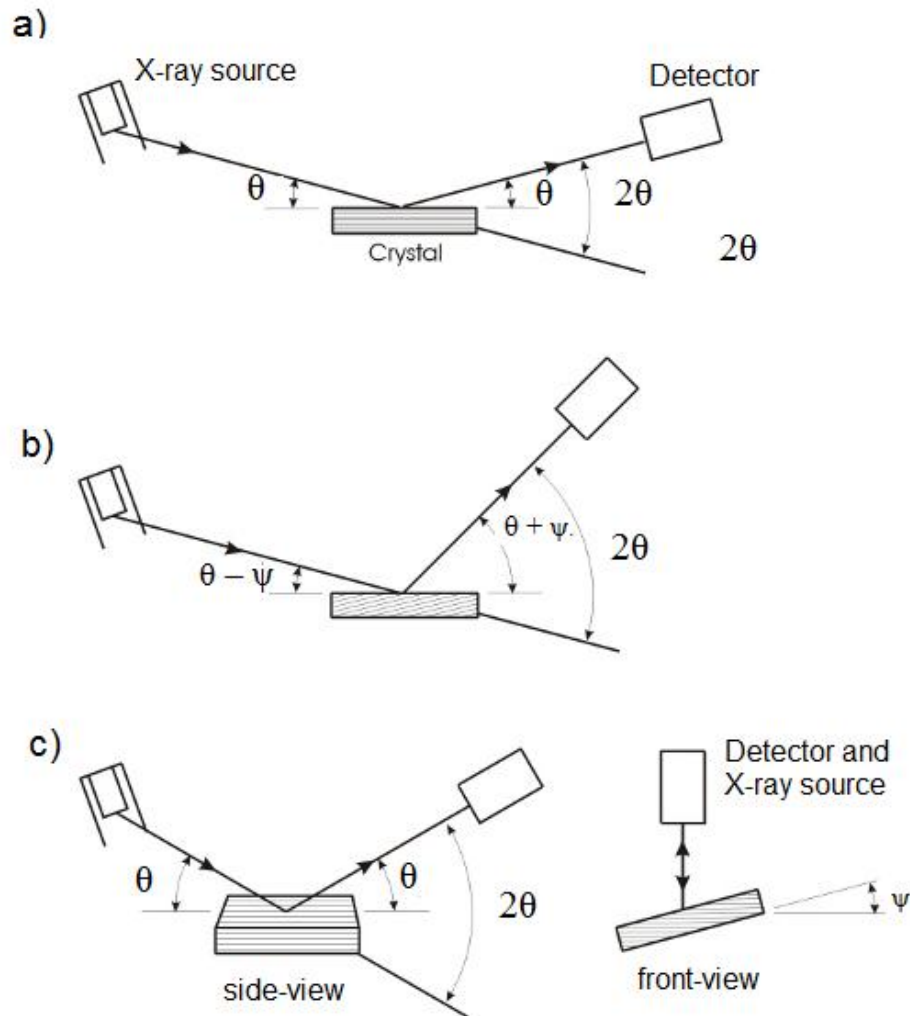


Figure 2.4: X-ray a) symmetric scan, b) asymmetric scan, and c) skew-symmetric scan techniques.

The XRD 2θ - θ scans, ω -scans, and asymmetric reciprocal space mapping (RSM) were performed under high-resolution mode set up. The set up of high-resolution mode consists of two Si 220 channel-cut crystals as the beam conditioner to provide four-bounce reflection and collimate the incident beam for 25 arcsec angular divergence, and a

dual channel Si 220 analyser (DCA) crystal. When RSM mode is applied, the loop scanning is used and the reciprocal space mapping is constructed by adding all the loop scan result. The X-ray reflectivity (XRR) was performed using only one two Si 220 channel-cut crystal and without DCA. The film thickness was then derived from analysis of XRR data using Bede software.

2.2.3.3. Transmission electron microscopy (TEM)

Transmission electron microscopy (TEM) is the most important instrument to obtain the atomic high-resolution images and to analyze defects in detail. There are two basic modes of TEM operation: diffraction patterns and imaging modes. As the beam of electrons passes through a crystalline specimen, it is scattered according to the Bragg's law. The beams that are scattered at small angles to the transmitted beam are focused by the objective lens to form a diffraction pattern at its back focal plane. The scattered beams are recombined to form an image in the image plane. The diffraction patterns are obtained by adjusting the imaging system lenses so that the back focal plane of the objective lens acts as the object plane for the intermediate lens. Then the diffraction pattern is projected onto the viewing screen. At the imaging mode, the intermediate lens is adjusted so that its object plane is the image plane of the objective lens. The image is then projected onto the viewing screen.

In this thesis, cross-sectional TEM specimens were prepared by tripod polishing method and focused ion beam (FIB) technique (FEI Nova 200). The tripod polished specimens were Ar-ion milled at angle of 4-6° and acceleration voltage of 4-5 kV. TEM specimens were then examined in a JEOL 2010F microscope at 200 kV accelerating voltage. The high-resolution TEM images were taken at high magnification up to 800k, and the lattice image of specimens can be obtained at magnification of 600k. Dislocation analyses were performed by tilting the specimen to the so called two-beam conditions, where only one diffracted beam is strong and the direct beam is the other strong spot. The steps to obtain the appropriate tilt conditions as follows:

- (i) Turn to diffraction patterns mode.
- (ii) Tilt the specimen into an appropriate zone axis (in this case [100])
- (iii) Tilt the specimen to the two-beam condition: only transmitted beam and the desired diffracted beam \mathbf{g} (in this case $\mathbf{g} = 002$ and $\mathbf{g} = 022$) and get rid of almost other diffraction spots (Fig. 2.5a). To get best diffraction contrast

from defects, the specimen is advisory to be tilted so that we have two-beam condition with slight deviation from the Bragg conditions. This is measured by the vector \mathbf{s} ($\mathbf{K} = \mathbf{g} + \mathbf{s}$, where \mathbf{K} is a diffraction vector) which is called the excitation error or deviation parameter. The best possible strong-beam image contrast conditions for a defect imaging is achieved when the excess Kikuchi line lies slightly outside its corresponding diffraction spot \mathbf{g} or small and positive deviation parameter $s > 0$ (Fig. 2.5b).

- (iv) To get two-beam bright-field image: insert the objective aperture on transmitted beam at optic axis. To get two-beam dark-field image: tilt the incident beam so that the strong diffraction spot \mathbf{g} moves onto the optic axis. If one does so, the \mathbf{g} diffraction will become weaker and the so called weak-beam dark-field (WBDF) image conditions or $3\mathbf{g}$ condition (Fig. 2.6) will be set, and then insert the objective aperture on the diffraction \mathbf{g} .
- (v) Turn to imaging mode and take the pictures.

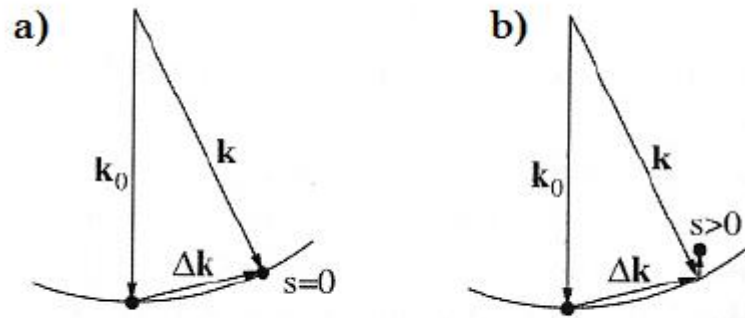


Figure 2.5: Ewald sphere constructions and the diffraction patterns for one intense diffraction spot with a) Kikuchi line runs exactly through its corresponding spot \mathbf{g} ($s = 0$), and b) the excess Kikuchi line lies outside its corresponding diffraction spot \mathbf{g} ($s > 0$).

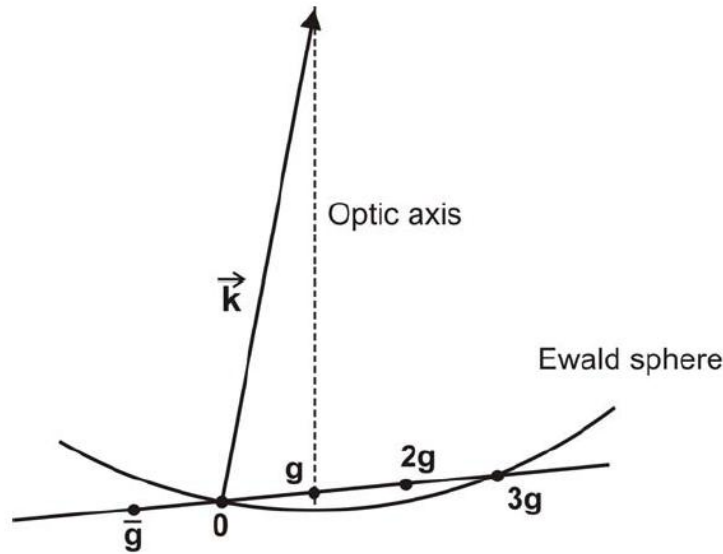


Figure 2.6: $3g$ condition for the WBDF image. The g reflection is in the optical axis with a large excitation error.

2.2.3.4. Atomic Force Microscopy (AFM)

Atomic Force Microscopy (AFM) is a common tool for the use of the surface imaging and analytical studies of roughness. Both contact and tapping mode are well suited for topographical imaging of surfaces, with vertical resolution ranging from one micron down to sub nanometer scales. In all techniques (contact, tapping, scanning tunneling, and lateral force mode) share a common approach where a motor controlling a mechanical tip is placed in a feedback loop as the tip is scanned across a surface. Tapping mode in D3100 is the most common imaging technique we have used. This mode operates by scanning a tip attached to the end of an oscillating cantilever across the sample surface. The amplitude of oscillation ranges from 20 nm to 100 nm, with the frequency near the resonant peak of the cantilever. The tip lightly taps the surface, altering the oscillatory motion as the scanner moves across the surface. By adjusting the vertical position of the scanner to maintain a constant RMS signal of oscillation, a surface is imaged. The oscillation is measured by a laser positioned by the user to reflect signal into a photodiode detector.

In this study, we have used Digital Instrument Nanoscope, D3100 AFM at a scan size of $5 \times 5 \mu\text{m}^2$ and the scan rate of 1 Hz to know surface imaging and roughness of the films.

2.2.3.5. Electrical conductivity measurement

The Hall Measurement System is a complete system for measuring the resistivity, carrier concentration, and mobility of semiconductors and compound semiconductors. The Hall Measurement System includes software with I-V curve capability for checking the ohmic integrity of the user made sample contacts.

In this thesis, a HMS-3000 Hall Measurement System was used to measure the resistivity of TiN_xO_y and TiC_xO_y films. Three measurements were performed for each deposited films, and the average results of the group are presented here.

2.3. Structure and properties of epitaxial TiN_xO_y films on MgO (001) substrates

2.3.1. Chemical composition and chemical state

Figure 2.7 shows XPS depth profiles of samples A, B, C and D with different oxygen content. As seen in Fig. 2.7, the chemical composition of samples A, B, C, and D is uniform. The chemical composition of the four samples is presented in Table 2.3. The results suggest that the addition of oxygen atoms occurred in the overstoichiometric TiN_x ($x > 1$). The chemical states of the four TiN_xO_y films were identified by examining Ti-2p, O-1s, and N-1s XPS spectra in high-resolution mode after Ar sputtering for one minute (~ 2 nm). As shown in Fig. 2.8, the Ti-2p_{3/2} peak in the spectra can be deconvoluted into three components of Ti-N bonding (454.9 eV corresponding to titanium nitride), N-Ti-O bonding (~ 456.7 eV corresponding to titanium oxynitride), and Ti-O bonding (458.4 eV corresponding to titanium dioxide) [2.5-7]. The N-1s spectra (Fig. 2.9) reveal a small amount of chemisorbed molecular nitrogen (398.7 eV) and two main components of titanium nitride (397 eV) and titanium oxynitride (396.2 eV) [2.6] in agreement with the results determined from Ti peaks. As shown Fig. 2.10, samples with higher oxygen content show stronger O-1s signals.

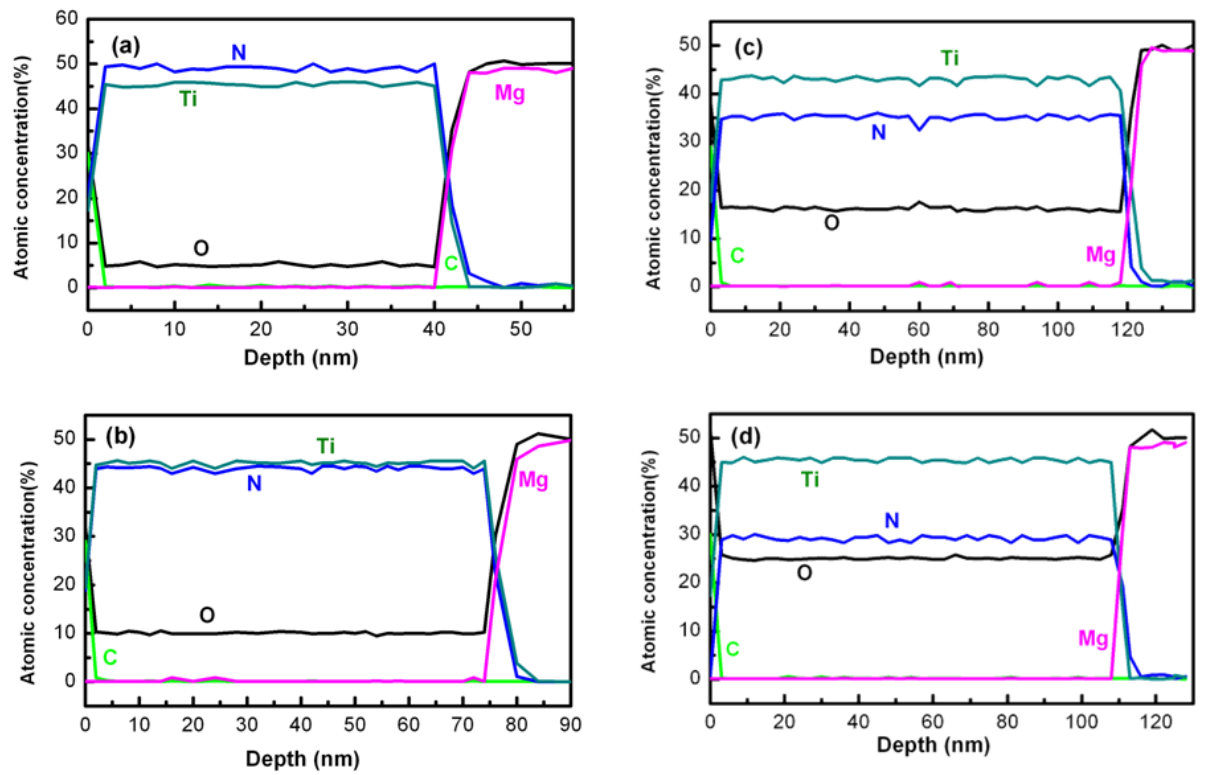


Figure 2.7: XPS depth profiles for sample a) A, b) B, c) C and d) D with different oxygen content.

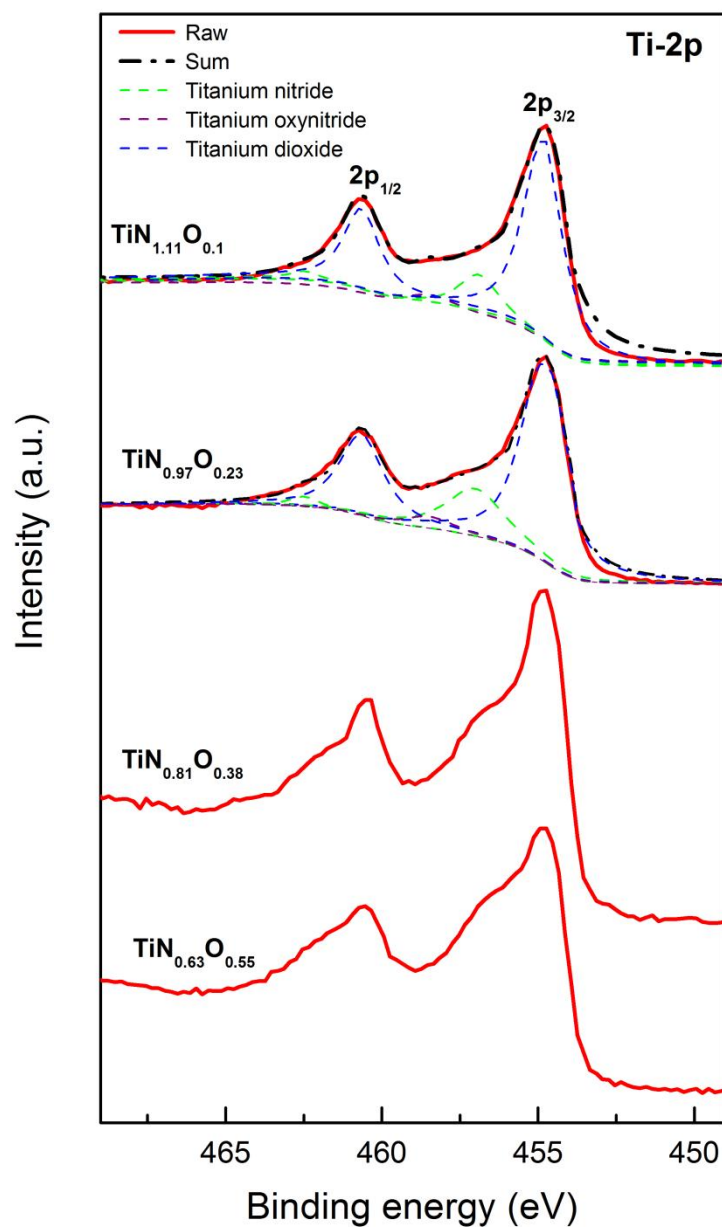


Figure 2.8: XPS spectra for Ti-2p of samples A, B, C and D after Ar sputtering for one minute. The spectra are deconvoluted into components of titanium nitride, titanium oxynitride, and titanium dioxide.

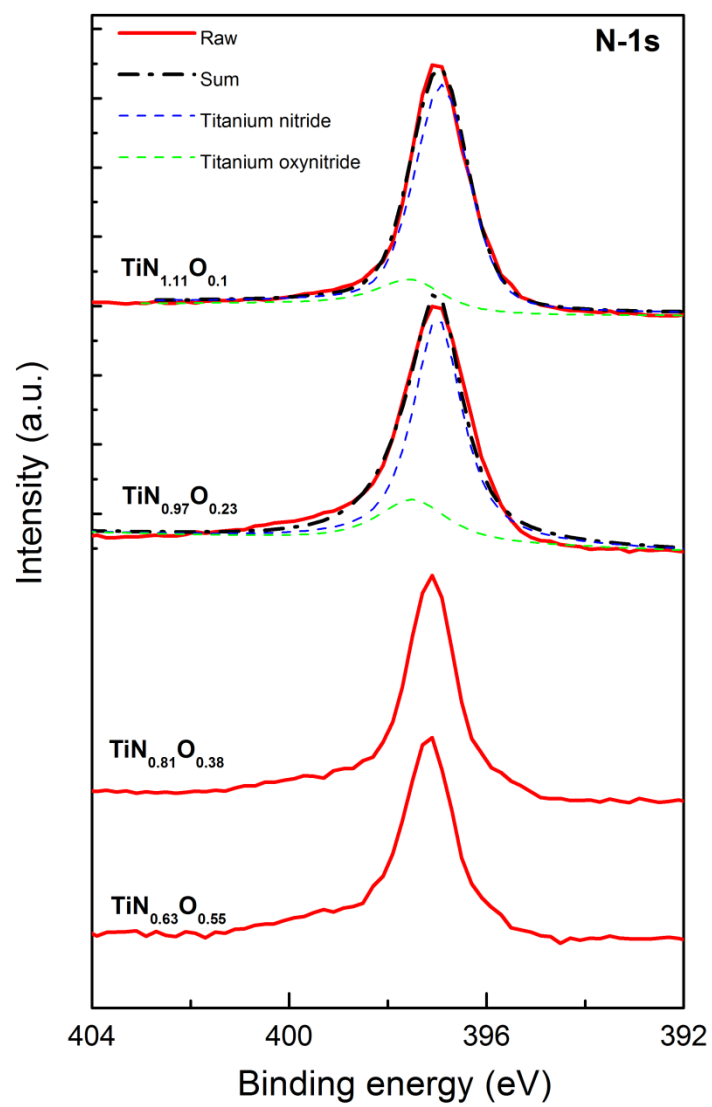


Figure 2.9: XPS spectra for N-1s of samples A, B, C and D after Ar sputtering for one minute. The spectra are deconvoluted into components of titanium nitride and titanium oxynitride.

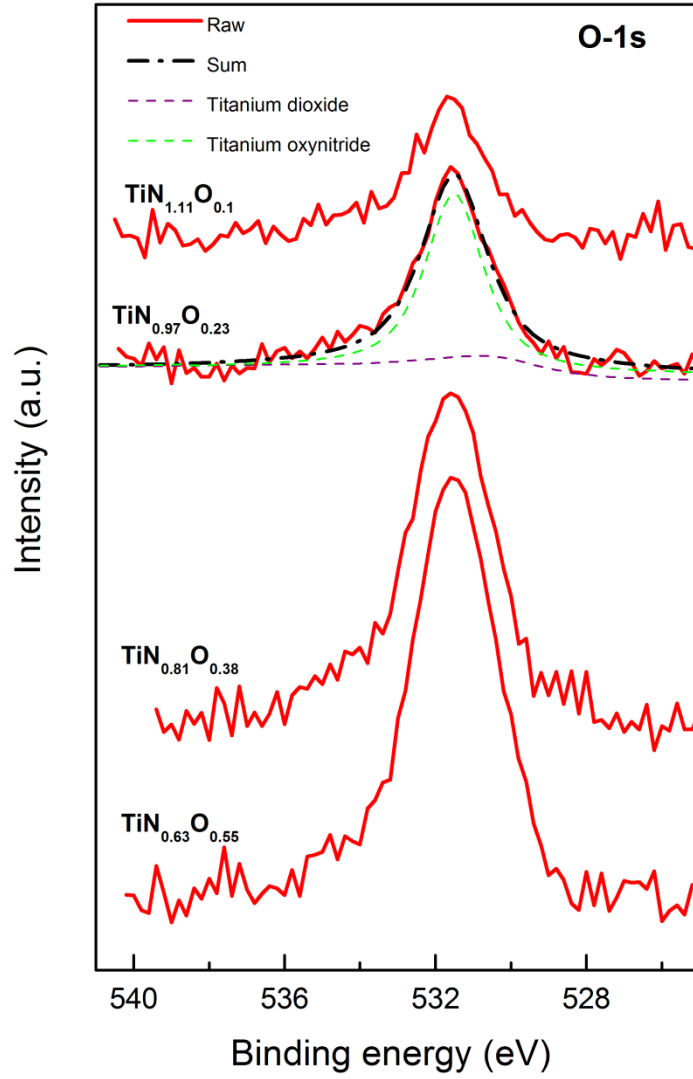


Figure 2.10: XPS spectra for O-1s of samples A, B, C and D after Ar sputtering for one minute. The spectra are deconvoluted into components of titanium oxynitride and titanium dioxide

2.3.2. Microstructure

X-ray diffraction (XRD) patterns of samples A, B, C, and D in Fig. 2.11 show only TiN_xO_y (002) and TiN_xO_y (004) reflections in addition to MgO ones, suggesting that (001) oriented single-phase titanium oxynitride has been deposited on MgO(001) substrates in our experimental conditions. As seen in Fig. 2.12 of high-resolution XRD 2θ - θ (HR-XRD) scans, TiN_xO_y (002) peaks shift to higher 2θ values with increasing oxygen content due to a change in the lattice parameter and to different residual strain. The finite-thickness interference fringes in HR-XRD 2θ - θ scans indicate that TiN_xO_y surfaces and TiN_xO_y

/MgO interfaces are smooth. The full width at half maximum (FWHM) of $\text{TiN}_x\text{O}_y(002)$ determined by x-ray rocking curve scans are about 58-62 arcsec (shown in Table 2.3), indicates that all as-deposited films have a good quality (the FWHM of MgO substrate is 42 arcsec). The x-ray ϕ -scan was done on those films to verify the orientation relationship between TiN_xO_y and MgO substrates. As seen in Fig. 2.13, four $\{022\}$ peaks of MgO and TiN_xO_y appear at the same ϕ angles with separation of 90° . This result suggests that the TiN_xO_y films have epitaxially grown on MgO substrates with the cube-on-cube relationship of $\text{TiN}_x\text{O}_y(001)/\text{MgO}(001)$ and $\text{TiN}_x\text{O}_y[100]/\text{MgO}[100]$.

Table 2.3: Chemical composition, thickness, in-plane a , out-of plane c , and relaxed a_o lattice parameters, FWHM of (002) TiN_xO_y , in-plane residual strain $\varepsilon_{||}$ and stress $\sigma_{||}$, and critical thickness h_c of TiN_xO_y films.

Sample	A	B	C	D
Chemical composition	$\text{TiN}_{1.11}\text{O}_{0.10}$	$\text{TiN}_{0.97}\text{O}_{0.23}$	$\text{TiN}_{0.81}\text{O}_{0.38}$	$\text{TiN}_{0.63}\text{O}_{0.55}$
Thickness	41 nm	76 nm	120 nm	110 nm
FWHM of (002) TiN_xO_y (arcsec)	62	58	60	61
a (Å)	4.2124	4.2116	4.2121	4.2112
c (Å)	4.2577	4.2541	4.2412	4.2231
a_o (Å)	4.2414	4.2388	4.2307	4.2188
$\varepsilon_{ }$ (%)	-0.69	-0.65	-0.44	-0.18
$\sigma_{ }$ (GPa)	-3.77	-3.53	-2.43	-0.99
h_c (nm)	9.6	10.4	17	49

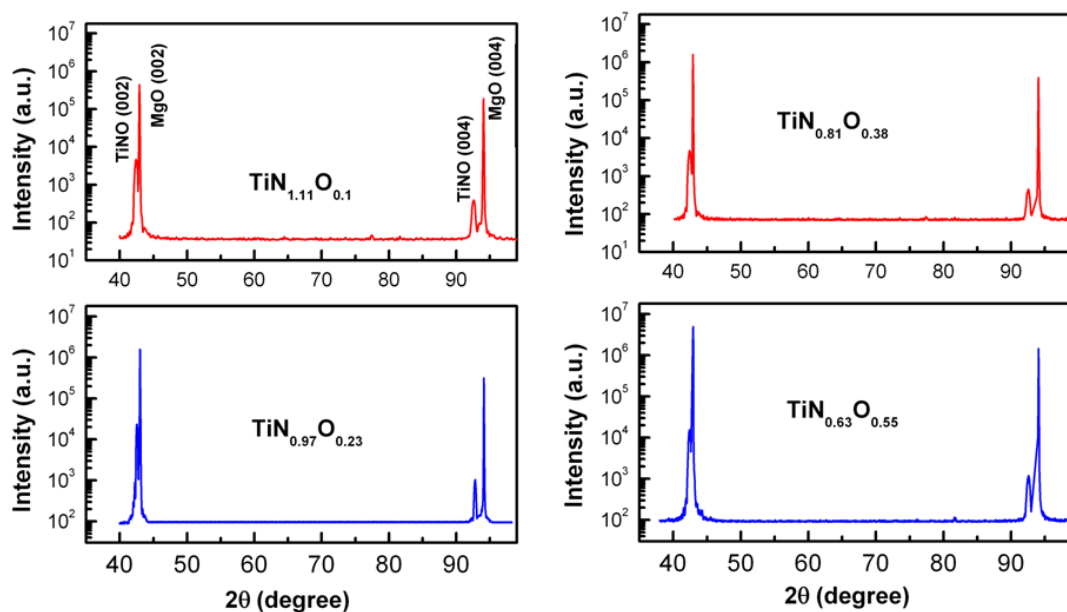


Figure 2.11: XRD 2θ-θ scans for four TiN_xO_y films.

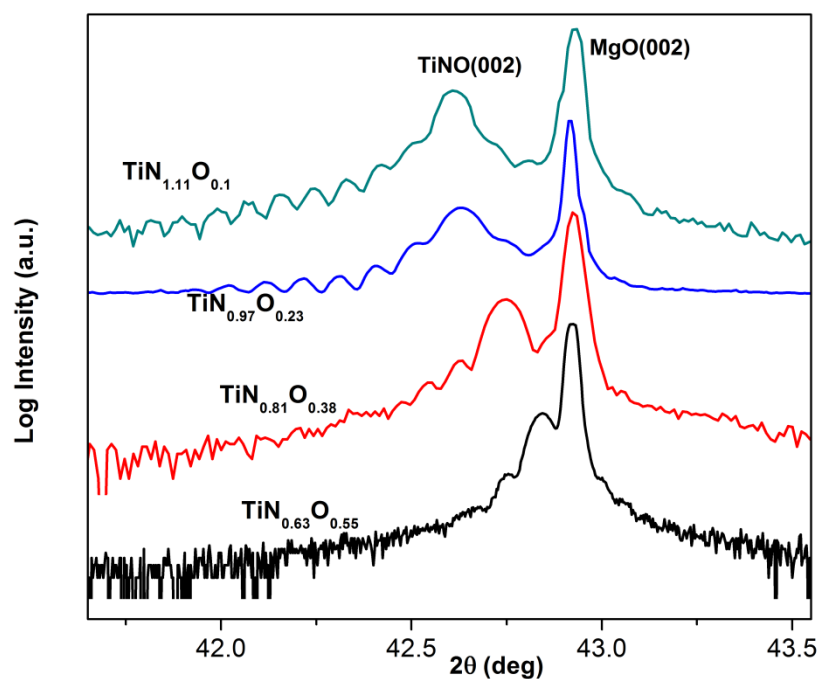


Figure 2.12: High-resolution XRD 2θ-θ scans for epitaxial TiN_xO_y films with different chemical composition deposited on MgO substrates

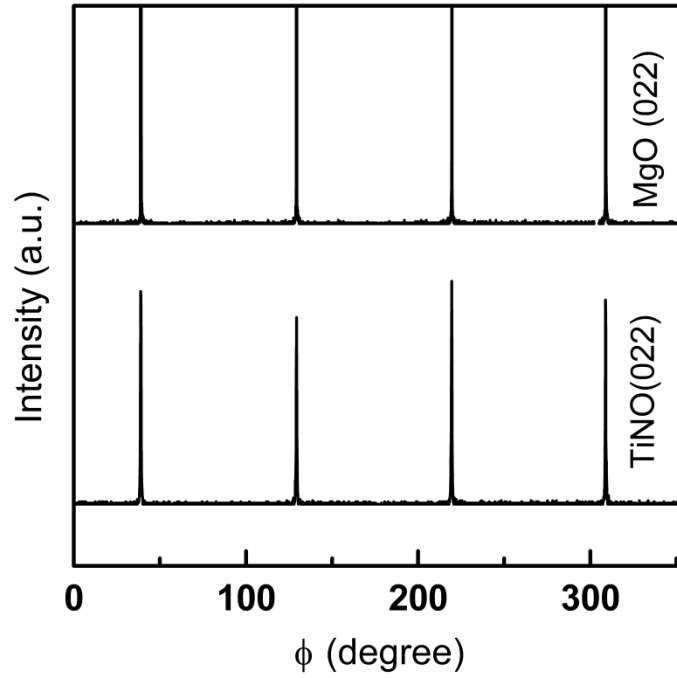


Figure 2.13: XRD ϕ -scan of {022} reflections for TiN_xO_y films grown on MgO substrate, showing epitaxial relationship between the film and the substrate is $\text{TiN}_x\text{O}_y(001)//\text{MgO}(001)$ and $\text{TiN}_x\text{O}_y[100]//\text{MgO}[100]$.

To investigate the effect of oxygen content on the lattice parameters of TiN_xO_y films, XRD reciprocal space maps (RSM) of asymmetric (113) MgO and (113) TiN_xO_y reflections were acquired. As shown in Fig. 2.14, asymmetric (113) MgO and TiN_xO_y reflections for both samples are almost vertically aligned, implying that TiN_xO_y lattices are in coherency with MgO one. Hence, all TiN_xO_y films may be under fully compressive strain as a result from lattice mismatch and thermal mismatch with MgO. The thermal strain was induced due to a large difference in coefficient of thermal expansion (CTE) of MgO and TiN_xO_y ($\alpha_{\text{MgO}} = 13 \times 10^{-6} \text{ K}^{-1}$ [2.8] and assume $\alpha_{\text{TiNO}} \sim \alpha_{\text{TiN}} = 9.35 \times 10^{-6} \text{ K}^{-1}$ [2.8]). When substrate temperature dropped from 700° C down to room temperature, MgO substrate contracted more than the TiN_xO_y layer, resulting in the generation of compressive strain of -0.54% in the TiN_xO_y layer. The out-of-plane, c , and in-plane, a , lattice parameters of TiN_xO_y can be determined as follows: $c = 3/Q_z$ and $a = \sqrt{2}/Q_x$, where Q_z and Q_x are vertical and horizontal vectors that lie along

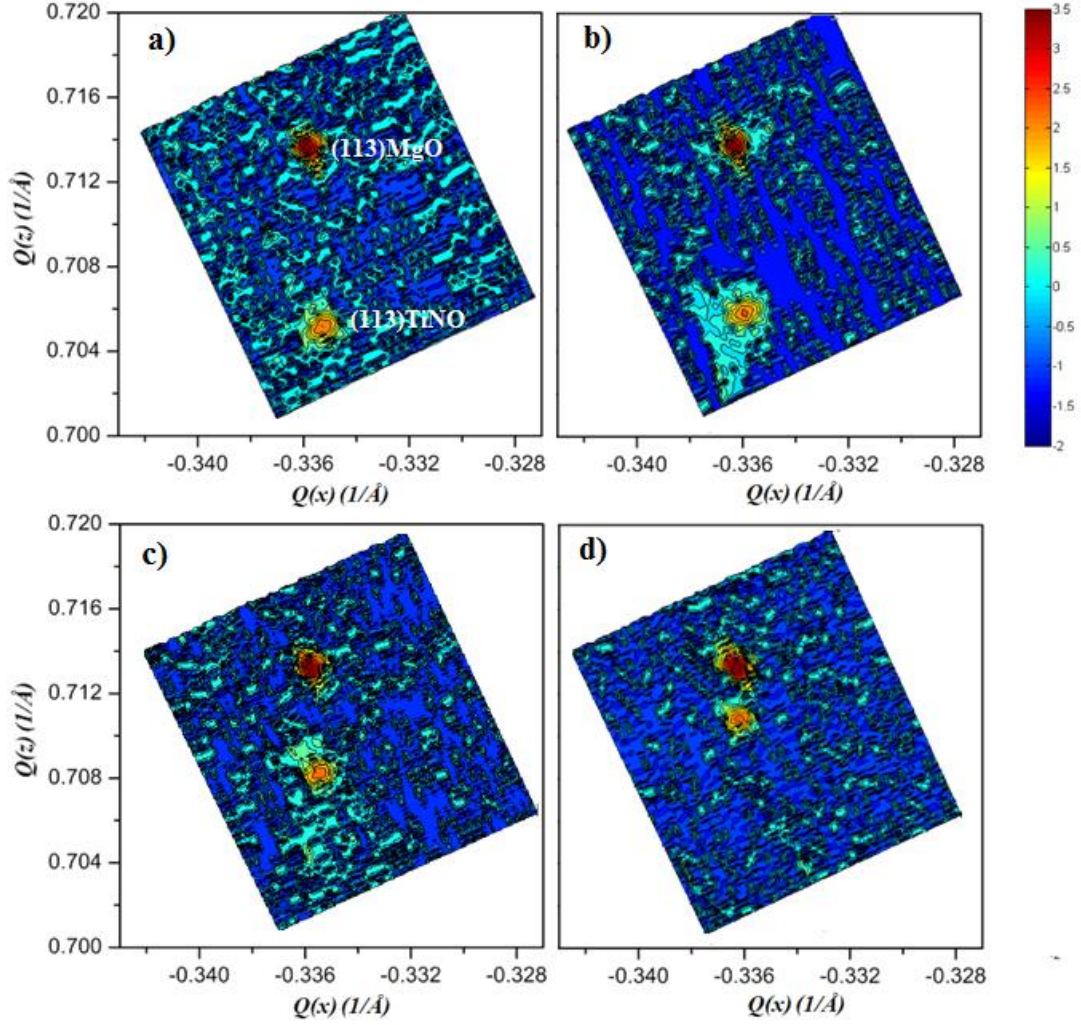


Figure 2.14: Reciprocal space maps of the asymmetric (113) MgO and (113) TiN_xO_y reflections with different composition of a) $\text{TiN}_{1.1}\text{O}_{0.10}$, b) $\text{TiN}_{0.97}\text{O}_{0.23}$, c) $\text{TiN}_{0.81}\text{O}_{0.38}$ and d) $\text{TiN}_{0.63}\text{O}_{0.55}$.

MgO [001] and MgO [110] directions, respectively [2.8]. The relaxed lattice parameter a_o can be calculated from c and a by using equation: $a_o = c[1 - 2\nu(c - a)/c(1 + \nu)]$ [2.8], where ν is the Poisson ratio of the deposited films. Due to the slight difference in Poisson ratio between TiN and TiO ($\nu_{\text{TiN}} = 0.22$ [2.8] and $\nu_{\text{TiO}} = 0.232$ [2.9]) and the large ratio of N/O of the deposited TiN_xO_y films, we can assume $\nu_{\text{TiNO}} \sim \nu_{\text{TiN}}$. Using MgO (113) peak as reference ($a_{\text{MgO}} = 4.2112 \text{ \AA}$ [2.8]), the lattice parameters (c , a , and a_o) and in-plane residual strain ϵ_{\parallel} and stress σ_{\parallel} , and theoretical critical thickness h_c of samples A, B, C, and D can be calculated and are listed in Table 2.3. Theoretical critical thickness h_c of TiN_xO_y films is calculated by using Matthews and Blakeslee model [2.10]. The in-plane residual stress σ_{\parallel} is calculated using Young's modulus value obtained from nanoindentation data

in Chapter 3. The results show that lattice parameters of TiN_xO_y films decrease with the increase of oxygen concentration but still lie in the lattice parameter range between bulk TiN ($a_{\text{TiN}} = 4.2417 \text{ \AA}$ from powder diffraction file PDF 38-1420) and bulk TiO ($a_{\text{TiO}} = 4.1770 \text{ \AA}$, PDF 8-117). Those results are also in good agreement with the values reported in ref. [2.11]. Due to the fact that the radius of oxygen anion is smaller than that of nitrogen anion, the substitution of oxygen for nitrogen enables lattice parameter to decrease with increasing oxygen concentration [2.12]. Additional to the effect of anion radii on the lattice parameter, the effect of electrostatic repulsion between N and O anions around Ti vacancies has also been taken into consideration [2.13]. Indeed, the XPS results above suggest that the substitution of oxygen for nitrogen occurs in the over-stoichiometric TiN_x , and such a non-stoichiometric structure has been reported to contain many Ti vacancies [2.14]. Therefore, there may have an electrostatic repulsion between anions around Ti vacancies. Besides, N atoms need three electrons to close its shell in order to achieve the most stable configuration (N^{3-}) while O atoms only need two (O^{2-}) [2.13]. Hence, the replacement of N^{3-} by O^{2-} induces a decrease in the electrostatic repulsion between the anions around Ti vacancies and consequently lattice parameter decreases.

The second source of compressive strain can be generated from the film/substrate lattice mismatch that is determined as $\delta = [a_{\text{MgO}} - a_{\text{film}}]/a_{\text{MgO}}$. δ is -0.73% for pure TiN, -0.716% for sample A, -0.655% for sample B, -0.466% for sample C, and -0.185% for sample D. The result also shows that more oxygen content incorporated into the deposited films can reduce the lattice mismatch between MgO and TiN_xO_y . In other words, the addition of oxygen can result in the high-quality titanium oxynitride with a composition which can make the deposited films to be excellently coherent with MgO, contrasting with the case of pure TiN on MgO. Indeed, author in ref. [2.8] have shown that stoichiometric TiN film is semi-coherent with MgO that resulted from the generation of misfit dislocations at TiN/MgO interface.

The x-ray reflectivity (XRR) curves of samples are shown in Fig. 2.15. From curve fitting, the thickness of the TiN_xO_y films can be determined and shown in Table 2.3.

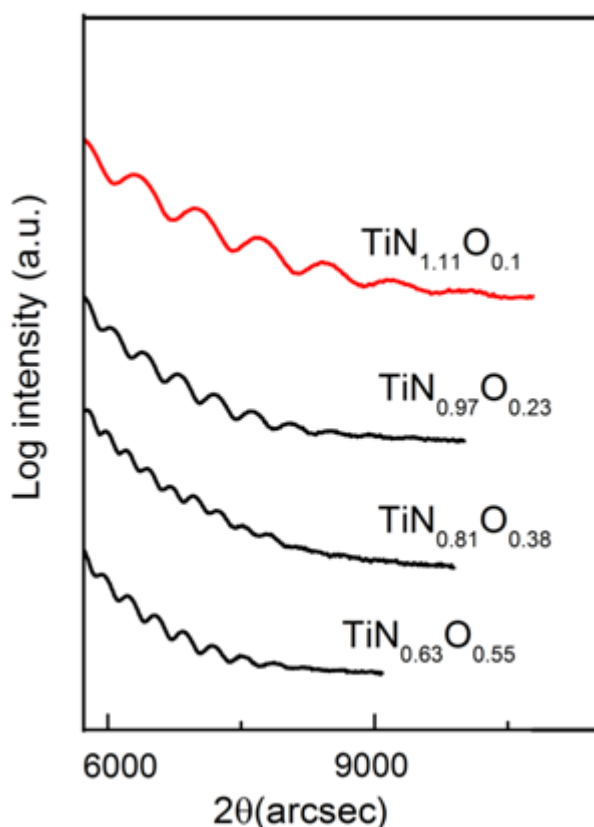


Figure 2.15: X-ray reflectivity curve for the four TiN_xO_y films.

The epitaxial growth of TiN_xO_y on MgO is also confirmed by cross-sectional high-resolution TEM as shown in Fig. 2.16 for samples A and B along [100] zone axis. The high-resolution TEM images reveal sharp and smooth interfaces without any interlayer between the films and the substrates. No misfit dislocations at the coherent interface between TiN_xO_y and MgO in both samples can be identified in the range over 12-14 nm as a result of the very small in-plane lattice mismatch between them, consistent with the XRD data above.

Figure 2.17a shows the cross-sectional bright field TEM image for sample A viewed along [100] zone axis. The corresponding selected area diffraction (SAD) pattern at the interface appears as a single-crystalline pattern, even though RSM maps above show MgO and TiN_xO_y reflections separated from each other. This implies that TiN_xO_y has been epitaxially grown on MgO with the cube-on-cube relationship, but due to a very small lattice mismatch

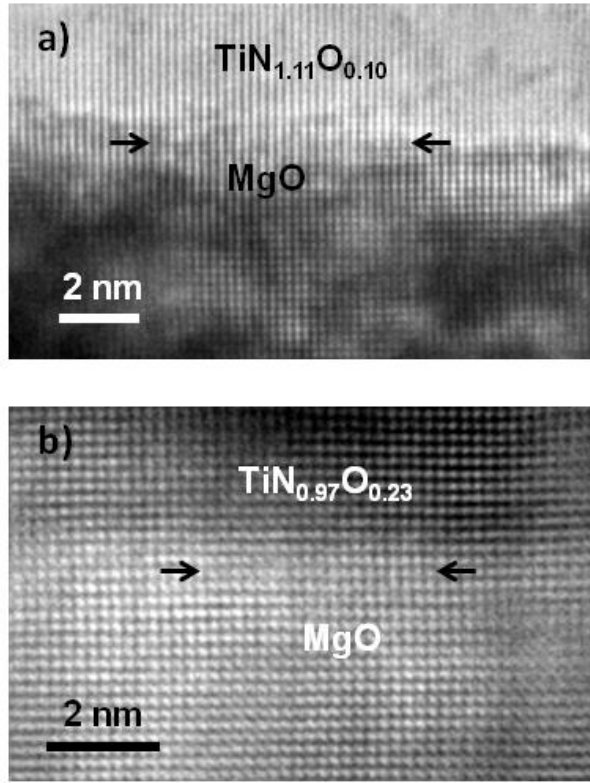


Figure 2.16: Cross-sectional HRTEM images of a) sample A and b) sample B along [100] zone axis showing sharp and smooth interfaces between TiN_xO_y and MgO (indicated by arrows). No misfit dislocations at the interfaces can be observed over the range of 12-14 nm.

between TiN_xO_y and MgO, their diffraction spots cannot be distinguished due to the limit of SAD resolution. To investigate microstructural defects in the TiN_xO_y epilayers, the two-beam TEM technique was performed for sample A along [100] zone axis. As seen in Figs. 2.17b and 2.17c, cross-sectional bright-field TEM images obtained with different two-beam conditions of $\mathbf{g} = 002$ and $\mathbf{g} = 022$ show that no dislocations can be identified in the range of 250 nm. The dislocation density can be estimated from XRD data [2.15-17]:

$$N = \frac{\alpha^2}{4.35 \times b^2}$$

where α is the tilt/twist angles (rad), respectively, b is the length of Burgers vectors of edge and screw dislocation in TiN_xO_y films, respectively. In TiN_xO_y structure, $b = \frac{1}{2}$

$\langle 110 \rangle$. The calculation of twist angle is complex, while the tilt angle can roughly approximate to the FWHM of (002) TiN_xO_y peak. The dislocation density is then calculated using tilt angle to be around $\sim 2 \times 10^7 \text{ cm}^{-2}$. Therefore, to identify one dislocation, the required observation range can be up to $5 \mu\text{m}$ that is far beyond the limited observation range in our specimens.

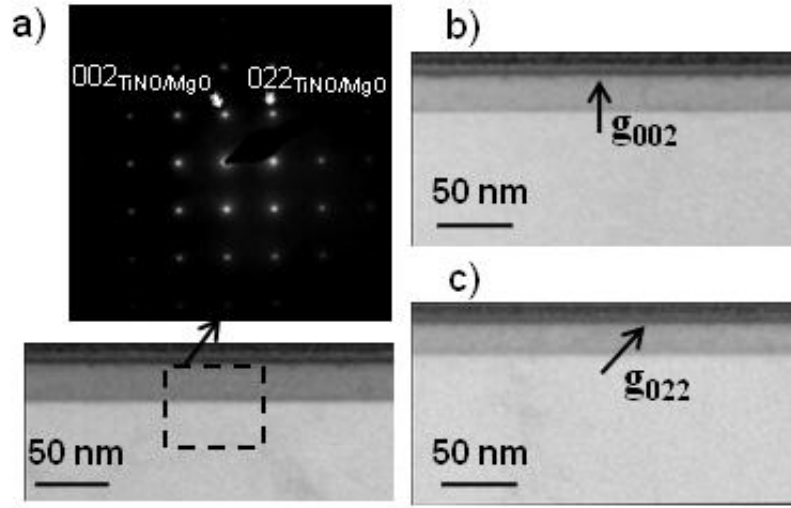


Figure 2.17: a) Cross-sectional TEM image of sample A in [100] bright-field and the corresponding diffraction pattern at the film/substrate interface. Cross-sectional bright-field TEM images of sample A under two-beam condition of b) $g = 002$ and c) $g = 022$.

2.3.3. Determination of the strain/stress tensors in the epitaxial $\text{TiN}_x\text{O}_y/\text{MgO}$ layers by x-ray diffraction

As clearly shown in Fig. 2.14 and Table 2.3, all the deposited films are under fully compressive strain due to thermal mismatch and lattice mismatch between TiN_xO_y and MgO . In this section, we present the calculation of the complete residual strain/stress tensors of those films by using the multiple skew-symmetric x-ray diffraction method [2.18]. Several techniques such as nano-indentation fracture method, X-ray diffraction, and Raman spectroscopy were used to measure residual stress in thin films. The X-ray method for determination of residual stress in crystalline materials is based on the measurement of inter-planar spacing d at various tilts, ϕ and ψ , to the X-ray beam, where ψ is the angle between the diffracting plane normal and the specimen surface normal, and

ϕ is azimuth angle (Fig. 2.18). The residual stress in the polycrystalline thin film with random orientation is mainly measured by $\sin^2\psi$ method. In this method, strains ϵ of a specific lattice plane (hkl) are measured at some offset angle ψ , and then the residual stress of thin film was calculated from the relationship of ϵ - $\sin^2\psi$. This method, however, cannot be directly applied to the stress determination in the epitaxial thin films because X-ray diffraction is obtained only at a definite ψ angle. Therefore, this method was modified to utilize to epitaxial thin films: multiple asymmetric lattice planes (hkl) were used instead of a specific lattice plane.

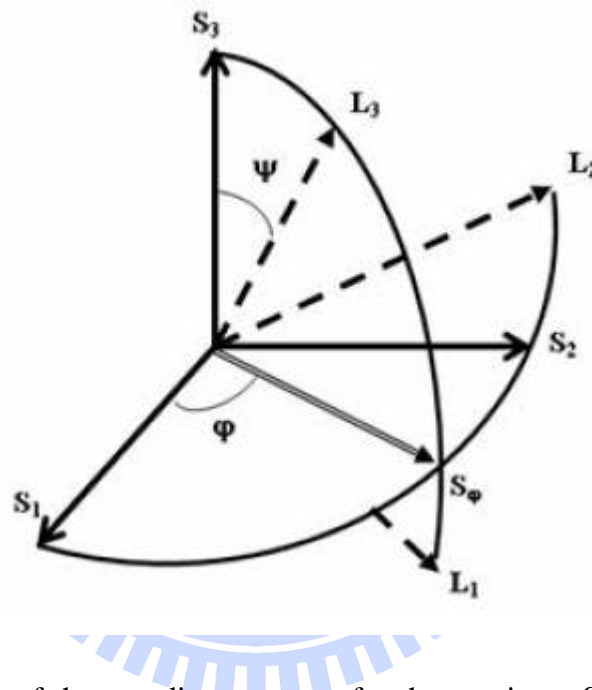


Figure 2.18: Definition of the coordinate system for the specimen S_i and the laboratory system L_i . The incident beam, the diffracted beam, and the normal to the diffracting planes L_3 are in the same plane. The sample can be rotated on the diffractometer in ϕ and in ψ . S_3 is normal to the sample surface, and S_1 and S_2 are in the sample surface.

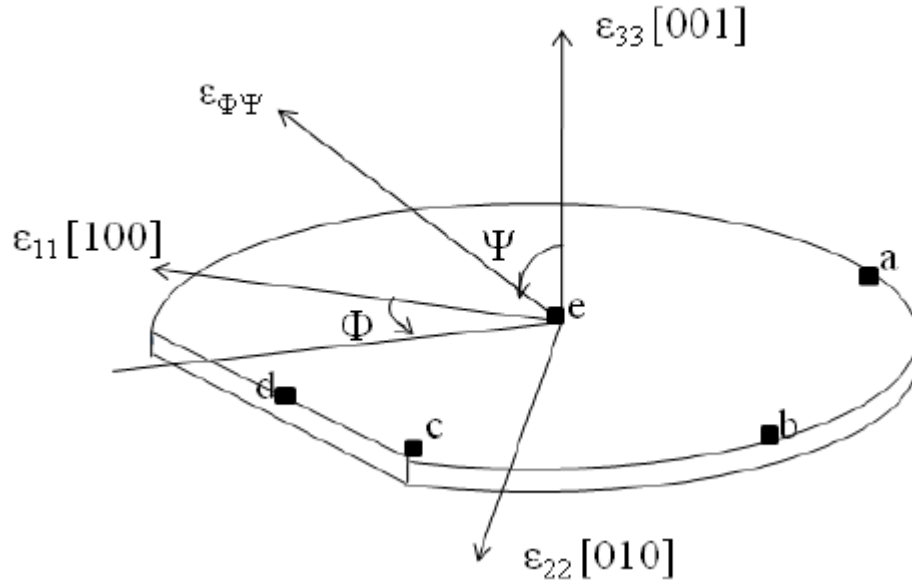


Figure 2.19: Coordinate settings.

As shown in the Fig. 2.19, the strains in the epitaxial TiN_xO_y (001)/MgO (001) system, $\varepsilon_{11}, \varepsilon_{22}, \varepsilon_{33}$ in the sample coordinate are coincident with crystallographic directions [100], [010] and [001] in crystal coordinate, respectively. The strain $\varepsilon_{\phi\psi}^L$, in the arbitrary orientation defined by angles ϕ and ψ , can be shown by the relative changes of the diffraction plane spacing and is associated with the diffraction peak displacement, that is:

$$\varepsilon_{\phi\psi}^L = \frac{\Delta d}{d_o} = \frac{d_{\phi\psi} - d_o}{d_o}$$

where $d_{\phi\psi}$ is the lattice spacing from proper diffraction position for a given reflection (hkl), and d_o is the (hkl) lattice spacing of the strain-free film. Since the diffraction data is obtained in the laboratory system \mathbf{L} , we have to transform $\varepsilon_{\phi\psi}^L$ into the strain tensor $\varepsilon_{\phi\psi}^S$ given in the sample system \mathbf{S} , according to:

$$\varepsilon_{\phi\psi}^L = \varepsilon_{33}^L = A_{3k} A_{3l} \varepsilon_{kl}^S$$

where A is the matrix which transforms from \mathbf{S} to \mathbf{L} which is defined by [2.19]:

$$A_{ik} = \begin{bmatrix} \cos \phi \cos \psi & \sin \phi \cos \psi & -\sin \psi \\ -\sin \phi & \cos \phi & 0 \\ \cos \phi \sin \psi & \sin \phi \sin \psi & \cos \psi \end{bmatrix}$$

therefore, we have:

$$\begin{aligned} \varepsilon_{\phi\psi}^L = & (\cos^2 \phi \sin^2 \psi) \times \varepsilon_{11}^S + (\sin 2\phi \sin^2 \psi) \times \varepsilon_{12}^S + (\cos \phi \sin 2\psi) \times \varepsilon_{13}^S \\ & + (\sin^2 \phi \sin^2 \psi) \times \varepsilon_{22}^S + (\sin \phi \sin 2\psi) \times \varepsilon_{23}^S + (1 - \sin^2 \psi) \times \varepsilon_{33}^S \end{aligned}$$

The complete strain/stress tensors can be determined by measuring strains from at least six different directions $[hkl]$ and then solving the linear equations. Tables 2.4, 2.5, 2.6, and 2.7 list the strains measured in multiple $[hkl]$ directions that represented by ϕ and ψ angles. Please note that in MgO and TiN_xO_y structure, we can assume $\varepsilon_{11}^S = \varepsilon_{22}^S$. It means that strain tensor can be solved from at least five directions $[hkl]$.

Table 2.4: XRD measured and calculated strains in 5 $[hkl]$ directions for the $\text{TiN}_{1.11}\text{O}_{0.10}$ film.

(hkl)	002	113	224	022	222
ψ	0	25.23	35.26	45	54.74
ϕ	0	45	45	0	45
2θ	42.058	73.763	125.982	62.088	78.702
$d_{\phi\psi}$	2.1288	1.284	0.864	1.494	1.215
d_o	2.121	1.279	0.866	1.500	1.224
$\varepsilon_{\phi\psi}^L (\%)$	0.0039	0.0037	-0.0015	-0.0038	-0.0077

Table 2.5: XRD measured and calculated strains in 5 $[hkl]$ directions for the $\text{TiN}_{0.97}\text{O}_{0.23}$ film.

(hkl)	002	113	224	022	222
ψ	0	25.23	35.26	45	54.74
ϕ	0	45	45	0	45
2θ	42.468	73.835	126.094	62.114	78.714
$d_{\phi\psi}$	2.127	1.282	0.864	1.493	1.215
d_o	2.119	1.278	0.865	1.499	1.224
$\varepsilon_{\phi\psi}^L (\%)$	0.0036	0.0035	-0.0013	-0.0036	-0.0073

Table 2.6: XRD measured and calculated strains in 5 $[hkl]$ directions for the $\text{TiN}_{0.81}\text{O}_{0.38}$ film.

(hkl)	002	113	224	022	222
ψ	0	25.23	35.26	45	54.74
ϕ	0	45	45	0	45
2θ	42.604	74.093	126.432	62.168	78.679
$d_{\phi\psi}$	2.121	1.279	0.863	1.492	1.215
d_o	2.115	1.276	0.864	1.496	1.221
$\varepsilon_{\phi\psi}^L (\%)$	0.0025	0.0024	-0.0009	-0.0025	-0.0050

Table 2.7: XRD measured and calculated strains in 5 $[hkl]$ directions for the $\text{TiN}_{0.63}\text{O}_{0.55}$ film.

(hkl)	002	113	224	022	222
ψ	0	25.23	35.26	45	54.74
ϕ	0	45	45	0	45
2θ	42.795	74.459	126.951	62.261	78.664
$d_{\phi\psi}$	2.112	1.273	0.8608	1.490	1.215
d_o	2.109	1.272	0.8612	1.492	1.2179
$\varepsilon_{\phi\psi}^L (\%)$	0.00102	0.00098	-0.00039	-0.00100	-0.00203

With the data obtained from Table 2.4, 2.5, 2.6, and 2.7, the residual strain tensors of TiN_xO_y films can be determined as:

$$\text{TiN}_{1.11}\text{O}_{0.10} \quad \varepsilon(\%) = \begin{bmatrix} -0.683 & 0.025 & 0.006 \\ 0.025 & -0.683 & -0.031 \\ 0.006 & -0.031 & 0.385 \end{bmatrix}$$

$$\text{TiN}_{0.97}\text{O}_{0.23} \quad \varepsilon(\%) = \begin{bmatrix} -0.641 & 0.022 & 0.0053 \\ 0.022 & -0.641 & -0.026 \\ 0.0053 & -0.026 & 0.361 \end{bmatrix}$$

$$\text{TiN}_{0.81}\text{O}_{0.38} \quad \varepsilon(\%) = \begin{bmatrix} -0.44 & 0.014 & 0.0039 \\ 0.014 & -0.44 & -0.018 \\ 0.0039 & -0.018 & 0.248 \end{bmatrix}$$

$$\text{TiN}_{0.63}\text{O}_{0.55} \quad \varepsilon(\%) = \begin{bmatrix} -0.18 & 0.008 & 0.0019 \\ 0.008 & -0.18 & -0.01 \\ 0.0019 & -0.01 & 0.102 \end{bmatrix}$$

From the strain tensors obtained above, the complete stress tensors could be calculated using Hook's Law for isotropic materials:

$$\begin{bmatrix} \sigma_{11} \\ \sigma_{22} \\ \sigma_{33} \\ \sigma_{23} \\ \sigma_{31} \\ \sigma_{12} \end{bmatrix} = \frac{E}{(1+\nu)(1-2\nu)} \begin{bmatrix} 1-\nu & \nu & \nu & 0 & 0 & 0 \\ \nu & 1-\nu & \nu & 0 & 0 & 0 \\ \nu & \nu & 1-\nu & 0 & 0 & 0 \\ 0 & 0 & 0 & 1-2\nu & 0 & 0 \\ 0 & 0 & 0 & 0 & 1-2\nu & 0 \\ 0 & 0 & 0 & 0 & 0 & 1-2\nu \end{bmatrix} \begin{bmatrix} \varepsilon_{11} \\ \varepsilon_{22} \\ \varepsilon_{33} \\ \varepsilon_{23} \\ \varepsilon_{31} \\ \varepsilon_{12} \end{bmatrix}$$

where ν E is the Young's modulus of the TiN_xO_y films. It is noticed that the Young's modulus strongly depends on the chemical composition of the TiN_xO_y films and the detailed calculation is presented in the chapter 4 below. The complete residual stress tensors of the TiN_xO_y films are then determined as:

$$\text{TiN}_{1.11}\text{O}_{0.10} \quad \sigma(\text{GPa}) = \begin{bmatrix} -3.76565 & 0.08812 & 0.02115 \\ 0.08812 & -3.76565 & -0.10926 \\ 0.02115 & -0.10926 & -0.00138 \end{bmatrix}$$

$$\text{TiN}_{0.97}\text{O}_{0.23} \quad \sigma(\text{GPa}) = \begin{bmatrix} -3.53453 & 0.07754 & 0.01868 \\ 0.07754 & -3.53453 & -0.09164 \\ 0.01868 & -0.09164 & -0.0029 \end{bmatrix}$$

$$\text{TiN}_{0.81}\text{O}_{0.38} \quad \sigma(\text{GPa}) = \begin{bmatrix} -2.42593 & 0.04934 & 0.01375 \\ 0.04934 & -2.42593 & -0.06344 \\ 0.01375 & -0.06344 & -0.00101 \end{bmatrix}$$

$$\text{TiN}_{0.63}\text{O}_{0.55} \quad \sigma(\text{GPa}) = \begin{bmatrix} -0.99167 & 0.02820 & 0.00670 \\ 0.02820 & -0.99167 & -0.0353 \\ 0.00670 & -0.0353 & -0.00227 \end{bmatrix}$$

From the residual stress tensors above, the principal stresses σ_1 , σ_2 , and σ_3 can be determined using Mohr's circle (Fig. 2.20) [2.20]:

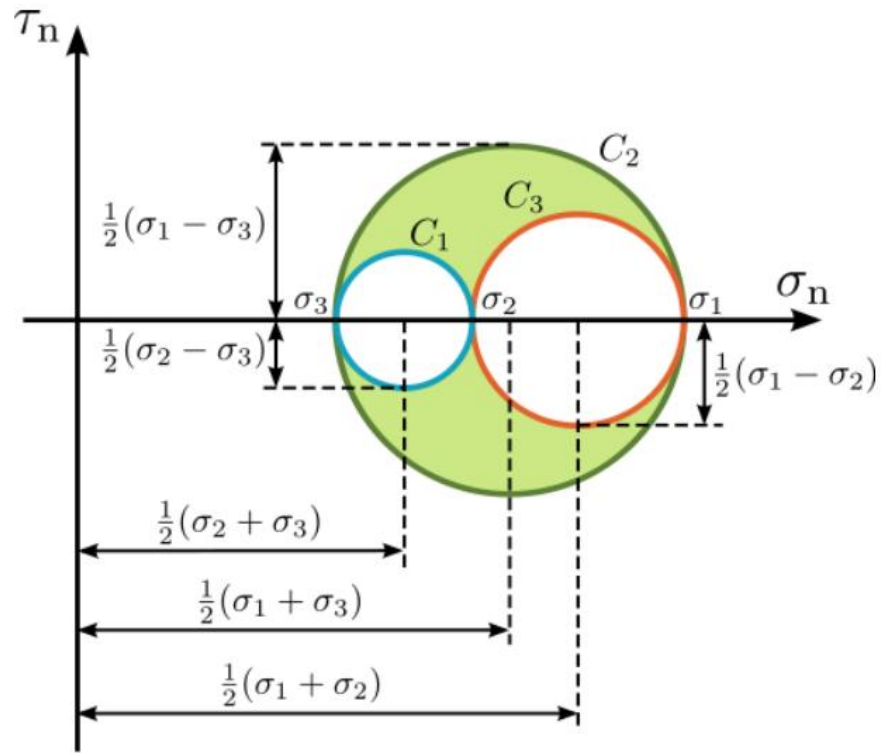


Figure 2.20. Mohr's circles for a three-dimensional state of stress.

Invariants :

$$I_1 = \sigma_{11} + \sigma_{22} + \sigma_{33}$$

$$I_2 = \sigma_{11}\sigma_{22} + \sigma_{22}\sigma_{33} + \sigma_{33}\sigma_{11} - \sigma_{12}^2 - \sigma_{23}^2 - \sigma_{13}^2$$

$$I_3 = \sigma_{11}\sigma_{22}\sigma_{33} + \sigma_{12}\sigma_{23}\sigma_{13} - \sigma_{12}^2\sigma_{33} - \sigma_{23}^2\sigma_{11} - \sigma_{13}^2\sigma_{22}$$

Calculations:

$$A_1 = -I_1, A_2 = I_2, A_3 = -I_3$$

If $I_3 \neq 0$:

$$Q = \frac{3A_1 - A_2^2}{9}$$

$$R = \frac{9A_1A_2 - 27A_3 - A_2^3}{54}$$

$$\theta = \cos^{-1} \left(\frac{R}{\sqrt{-Q^3}} \right)$$

$$R_1 = 2 \times \sqrt{-Q} \times \cos \left(\frac{\theta}{3} \right) - \frac{A_2}{3}$$

$$R_2 = 2 \times \sqrt{-Q} \times \cos \left(\frac{\theta + 2\pi}{3} \right) - \frac{A_2}{3}$$

$$R_3 = 2 \times \sqrt{-Q} \times \cos \left(\frac{\theta + 4\pi}{3} \right) - \frac{A_2}{3}$$

$$\sigma_1 = \min(R_1, R_2, R_3)$$

$$\sigma_2 = \text{median}(R_1, R_2, R_3)$$

$$\sigma_3 = \max(R_1, R_2, R_3)$$

The maximum shear stresses τ_{max} acting on the plane that bisects the angle between the planes in which the maximum σ_1 and minimum σ_3 principal stresses act (Fig. 2.21) are determined as [2.21]:

$$\tau_{max} = \frac{1}{2} |\sigma_1 - \sigma_3|$$

It is also noticed that the maximum shear stresses act on the slip directions $\langle 110 \rangle$ of TiN_xO_y (NaCl structure), therefore they are responsible for dislocation nucleation. The principal stresses σ_1 , σ_2 , and σ_3 and maximum shear stresses τ_{max} of all TiN_xO_y films are calculated and presented in Table 2.8.

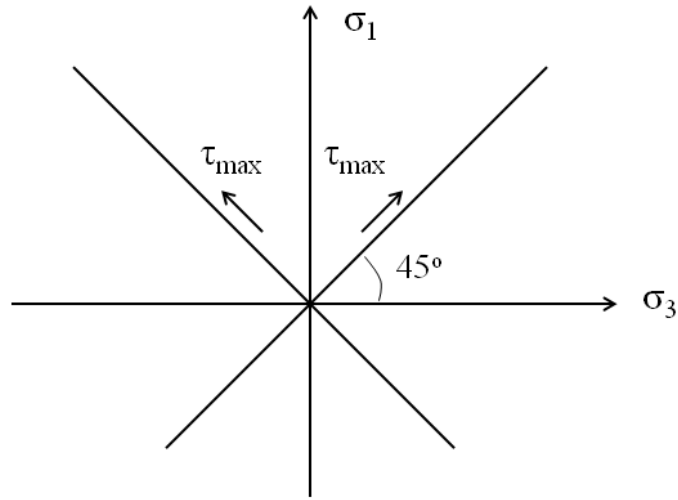


Figure 2.21: The maximum shear stresses τ_{max} acting on the plane that bisects the angle between the planes in which the maximum σ_1 and minimum σ_3 principal stresses act.

Table 2.8: The principal stress σ_1 , σ_2 , and σ_3 , maximum shear stress τ_{max} , and the critical shear stress τ_{crit} [2.22] of TiN_xO_y films.

	$\text{TiN}_{1.11}\text{O}_{0.10}$	$\text{TiN}_{0.97}\text{O}_{0.23}$	$\text{TiN}_{0.81}\text{O}_{0.38}$	$\text{TiN}_{0.63}\text{O}_{0.55}$
σ_1 (GPa)	0.0018	0.00052	0.00065	0.0035
σ_2 (GPa)	-3.678	-3.457	-2.377	-0.963
σ_3 (GPa)	-3.854	-3.612	-2.776	-1.02
τ_{max} (GPa)	1.93	1.81	1.39	0.51
τ_{crit} (GPa)	3.52	3.29	3.16	2.91

Again, the stresses in the TiN_xO_y films are not relaxed even in the films with low oxygen content, which show the thickness that much larger than the theoretical critical thickness h_c (see Table 2.3). This could be explained from the viewpoint of the critical shear stress for dislocation nucleation. Indeed, an experimental investigation has shown that the critical shear stress τ_{crit} for the nucleation of dislocations in a single crystal

TiN(001) [2.22] is about $G/50$ (G is the shear modulus for TiN). In the case of TiN_xO_y films with low oxygen content, we can also assume $\tau_{crit} \sim G/50$. The values of τ_{crit} for all samples are also listed in Table 2.8 for comparison. The results clearly show that the maximum shear stresses in the TiN_xO_y films are about 2 - 6 times lower than critical shear stress for dislocation nucleation. Therefore, no stress relaxation caused by dislocation nucleation could be observed in the TiN_xO_y films. Similar behavior without relaxation can be also observed in epitaxial TiN_x ($0.67 \leq x \leq 1$) films [2.8], in which the film thickness is much larger than the critical thickness (more than 10 times).

2.3.4. Surface morphology

The surface morphology of samples A, B, C, and D is shown in Fig. 2.22. The film surface is very uniform and smooth with root-mean-square roughness of 0.29 nm (sample A), 0.26 nm (sample B), 0.28 nm (sample C), and 0.31 nm (Sample D).

2.3.5. Electronic properties

The resistivity of TiN_xO_y films measured by Hall measurement method was found to be 28 $\mu\Omega\cdot\text{cm}$, 33 $\mu\Omega\cdot\text{cm}$, 41 $\mu\Omega\cdot\text{cm}$, and 53 $\mu\Omega\cdot\text{cm}$ for samples A, B, C, and D, respectively, indicating the metallic conduction behavior of the deposited films. The resistivity of TiN_xO_y films are much smaller than that of bulk TiO (190 $\mu\Omega\cdot\text{cm}$) and about two times larger than that of the pure epitaxial TiN ($\sim 15 \mu\Omega\cdot\text{cm}$) [2.23]. It has been shown that the increasing resistivity in the series of TiN, TiN_xO_y , and TiO can be explained by considering free electron concentration [2.24]. The lower free electron concentration results in poor conductivity of TiO and to a lesser extent TiN_xO_y [2.24]. The results can be compared with those reported in ref. [2.23], in which the resistivity of epitaxial TiN_xO_y films, with oxygen concentration of 7.02 – 11.11 at.%, is about 21.0 – 32.3 $\mu\Omega\cdot\text{cm}$. Hence, compared with polycrystalline TiN_xO_y films that have been shown to have the resistivity in the order of magnitude from $\text{m}\Omega\cdot\text{cm}$ to $\Omega\cdot\text{cm}$ [2.6, 7] epitaxial growth of TiN_xO_y films certainly can greatly improve electrical conductivity.

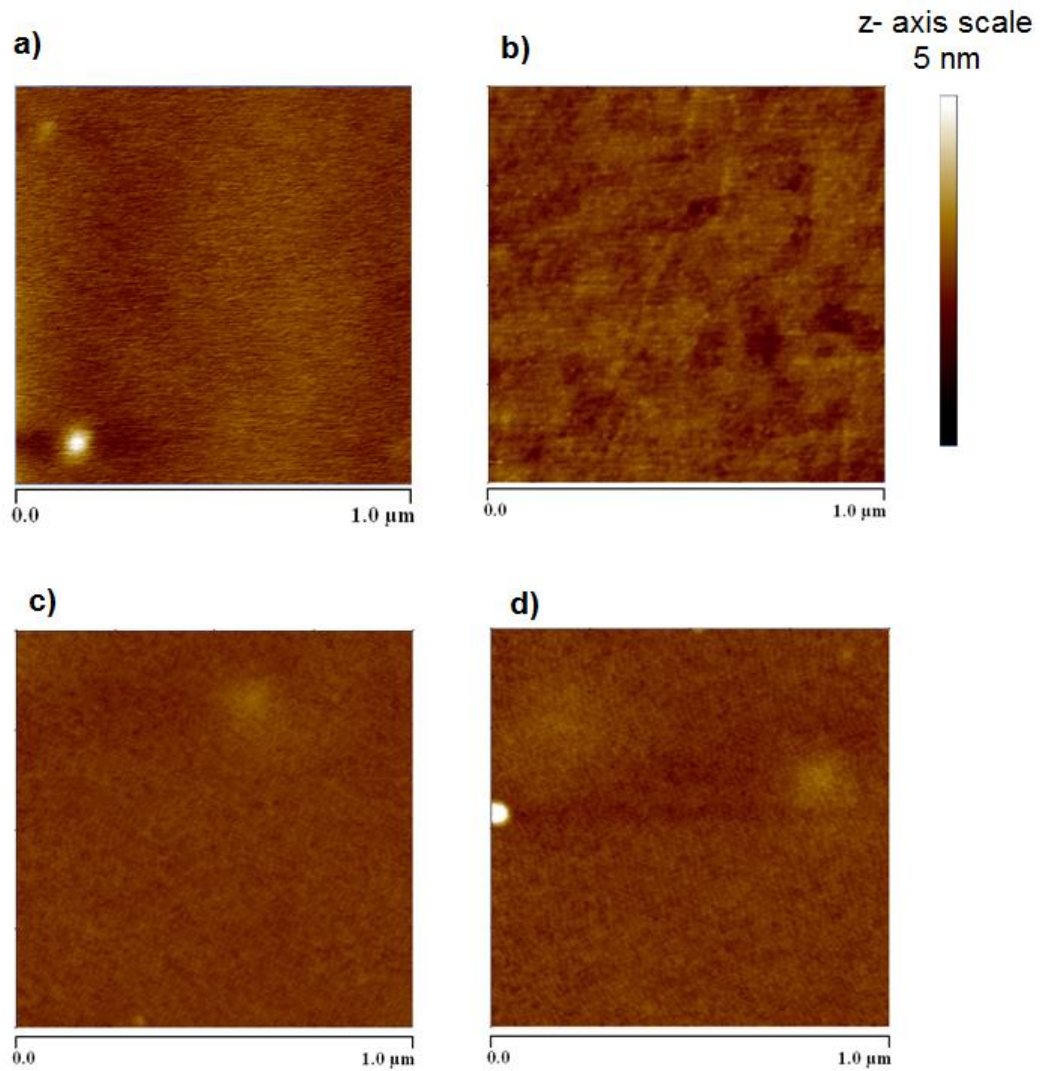


Figure 2.22: AFM images of TiN_xO_y surface for a) sample A, b) sample B, c) sample C, and d) sample D.

2.4. Structure and properties of epitaxial TiC_xO_y films on MgO (001) substrates

2.4.1. Chemical composition

Chemical composition of the TiC_xO_y film was determined by XPS measurements. Figure 2.23 shows high-resolution C-1s, Ti-2p, and O-1s XPS spectra for TiC_xO_y as a function of the Ar sputtering time. As shown in Fig. 2.23a, the C-1s spectrum from the deposited TiC_xO_y surface after air exposure shows that there are three components. The peak at 284.9 eV is assigned to hydrocarbon contamination [2.25]. The peak with lower energy at 281.8 eV corresponds to Ti-C bond [2.26, 27]. The weak peak observed at 288.8 eV is typical for C-O bond. After 1 minute of surface cleaning by Ar sputtering,

only one C-1s peak corresponding to Ti-C bond is observed. Similar situation is also found for Ti-2p signal (Fig. 2.23b). The spectrum of Ti-2p before surface cleaning exhibits two groups of Ti-2p_{3/2} and Ti-2p_{1/2}. In addition of Ti-C bonds at 454.9 and 460.8 eV, the Ti-2p_{3/2} component at 458.4 eV corresponds to Ti-O bond in TiO₂, and it disappeared after only 1 minute of Ar sputtering. Instead, only Ti-2p_{3/2} component at 454.9 eV can be observed [2.26, 27]. This component also contains Ti-2p_{3/2} in TiO that has been reported to have a peak value at 455.1 eV [2.28]. The O-1s XPS spectrum (Fig. 2.23c) of the air-exposed TiC_xO_y film exhibits a broad peak that can be decomposed into two components at 530 eV and 531.5 eV. The peak at 530 eV corresponds to O-1s in TiO₂ [2.29]. The higher binding energy peak at 531.5 eV can be assigned to O-1s in TiO [2.25, 30]. After 1 minute of Ar sputtering, only a single peak at 531.5 eV is observed. The XPS depth profile in Fig. 2.24 shows that the film has a uniform chemical composition. The average chemical composition can be determined from the values from 1 to 8 minutes of sputtering time and shown in the insert of Fig. 2.24. As a result, the stoichiometry of titanium oxycarbide is about TiC_{0.47}O_{0.69}. The higher oxygen content in the deposited film compared with that of target can be considered as a consequence of residue of oxygen in the reaction chamber that might contribute 9-22 at.% to the composition of TiC films grown even under high vacuum (1.5×10^{-7} Torr) [2.27]. This residual oxygen could strongly react with Ti ions emitted from laser ablation plume [2.2] due to high affinity between them. Also it is often found oxygen incorporation in deposited TiN films by PLD due to the interaction of Ti ions with oxygen [2.23, 31].

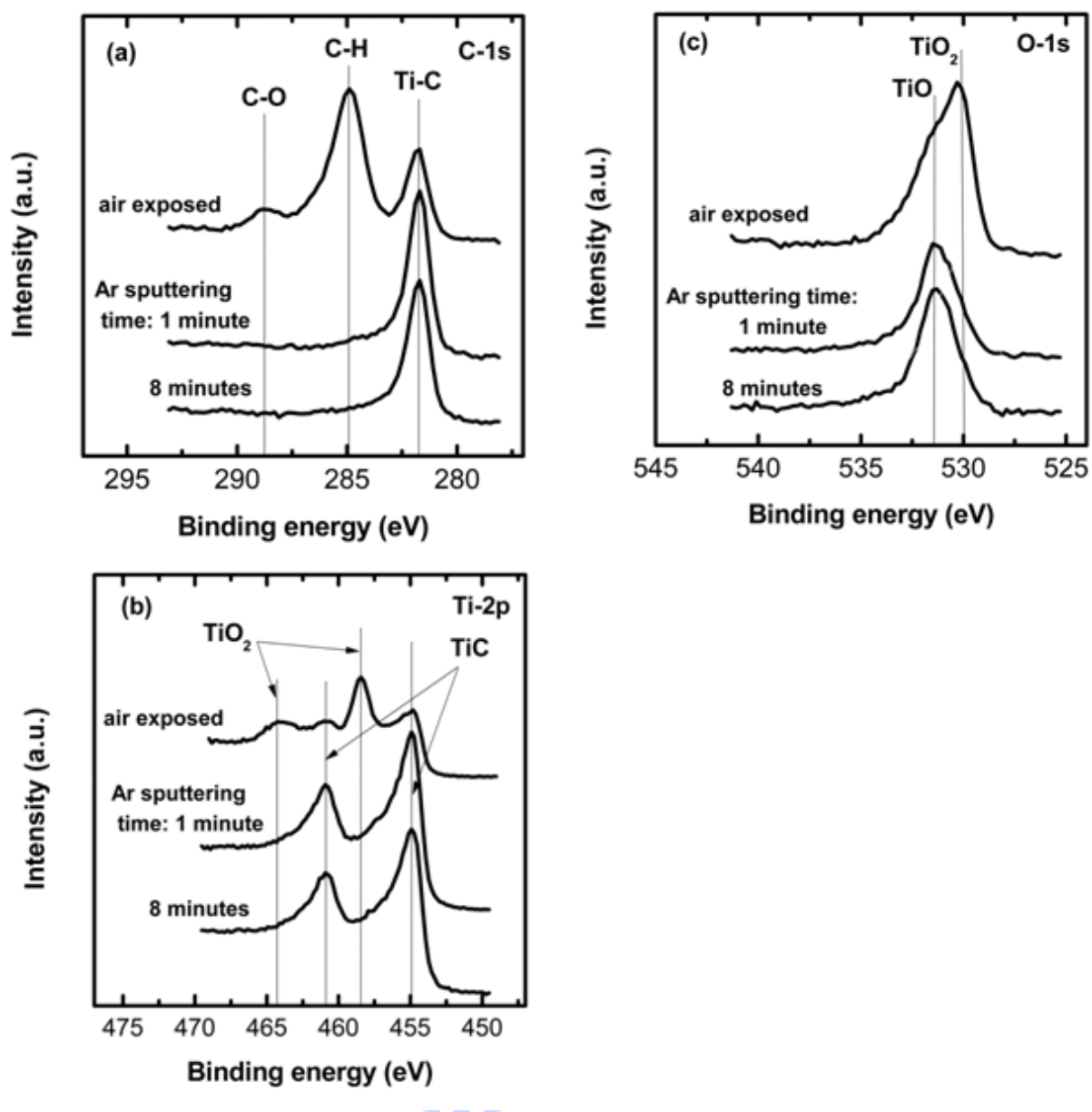


Figure 2.23: XPS spectra for (a) C-1s, (b) Ti-2p, and (c) O-1s, as a function of Ar sputtering time.

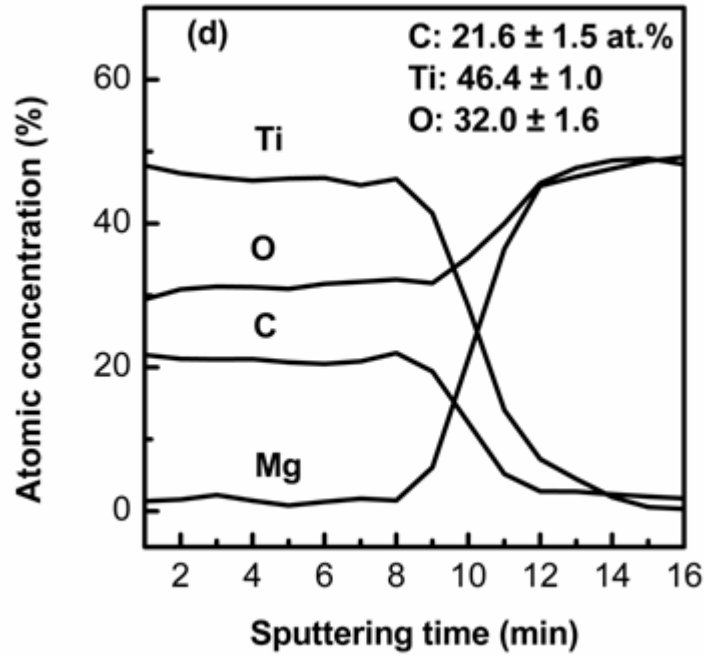


Figure 2.24: XPS depth profile for TiC_xO_y film deposited on MgO.

2.4.2. Microstructure

X-ray diffraction pattern of a titanium oxycarbide film is shown in Fig. 2.25a. It is seen only (002) and (004) reflections of TiC_xO_y and MgO, suggesting a textured or epitaxial relationship between the deposited film and MgO substrate. The d-spacing of (002) is determined to be 2.146 Å. As shown in Fig. 2.25b of the x-ray rocking curve measurement of (002) $\text{TiC}_{0.47}\text{O}_{0.69}$, the full width at half maximum (FWHM) is 133 arcsec, indicating that $\text{TiC}_{0.47}\text{O}_{0.69}$ grown on MgO has a very good quality. The x-ray ϕ -scan was also performed, using {022} reflections of substrate and film, to verify the epitaxy between the deposited film and MgO substrate. As shown in Fig. 2.26, four {022} diffraction peaks separated by 90° appear at the same ϕ angles for both the film and the substrate. This result illustrates that the deposited film has epitaxially grown on MgO with the cube-on-cube relationship of $\text{TiC}_{0.47}\text{O}_{0.69}(001)//\text{MgO}(001)$ and $\text{TiC}_{0.47}\text{O}_{0.69}[100]//\text{MgO}[100]$. Fig. 2.27 shows the x-ray reflectivity curve of the $\text{TiC}_{0.47}\text{O}_{0.69}$ film deposited on MgO, from which the film thickness can be determined to be 45 nm. As a result, the growth rate is estimated to be approximately 22.5 nm/h.

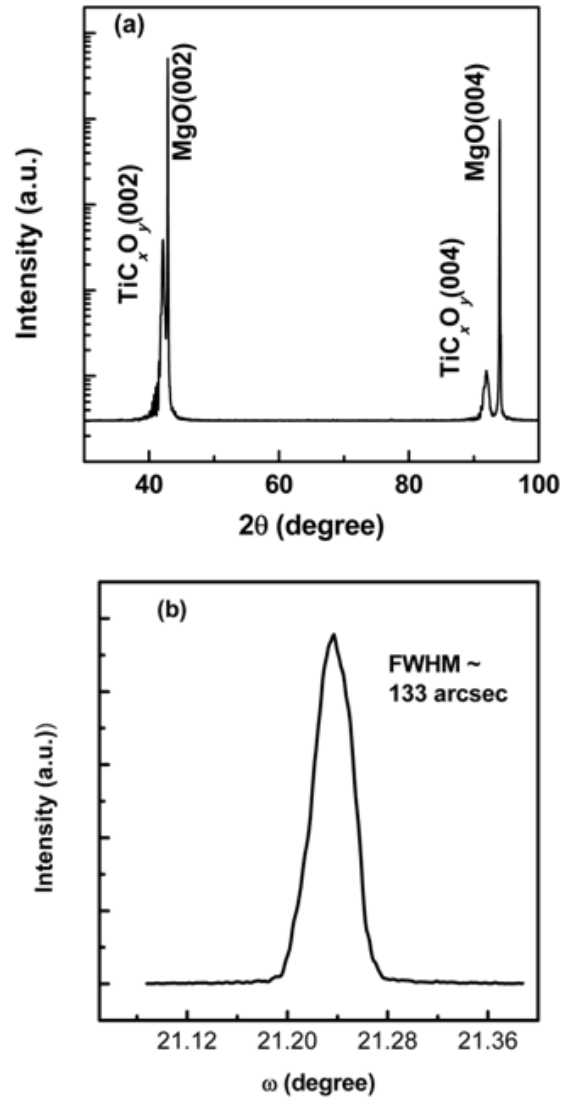


Figure 2.25: XRD (a) 2θ - θ scan and (b) ω -scan for $\text{TiC}_{0.47}\text{O}_{0.69}\text{TiC}_x\text{O}_y$ film deposited on MgO (001).

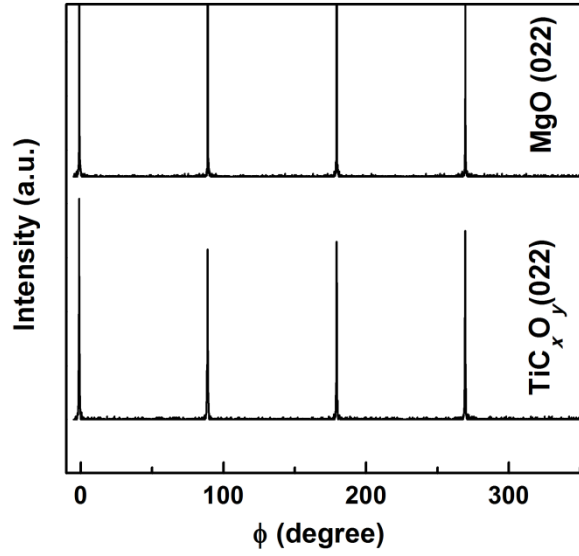


Figure 2.26: XRD ϕ -scan of {022} planes for $\text{TiC}_{0.47}\text{O}_{0.69}$ film on MgO (001) substrate, showing that epitaxial relationship between the film and the substrate is $\text{TiCO}(001)//\text{MgO}(001)$ and $\text{TiCO}[100]//\text{MgO}[100]$.

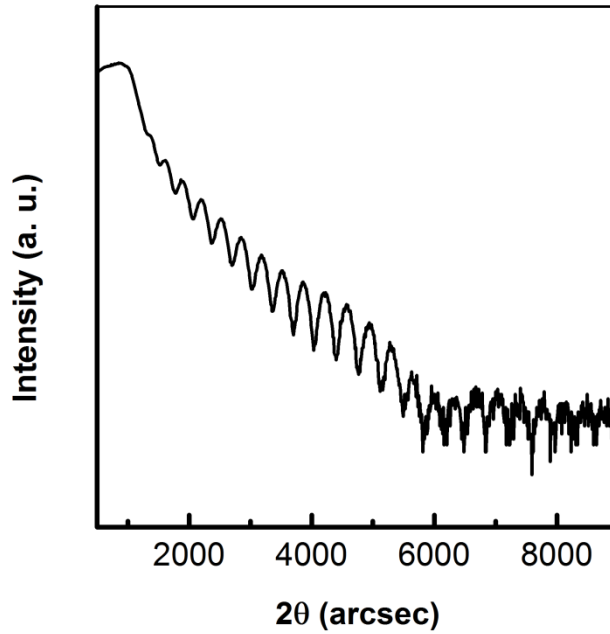


Figure 2.27: X-ray reflectivity curve for the deposited $\text{TiC}_{0.47}\text{O}_{0.69}$ film.

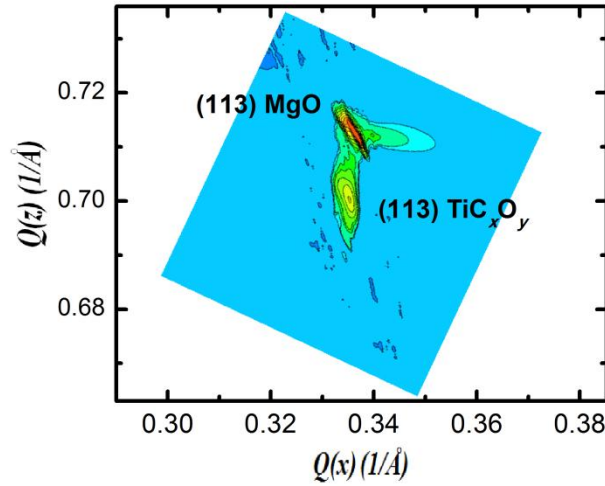


Figure 2.28: Reciprocal space map of the asymmetric (113) for $\text{TiC}_{0.47}\text{O}_{0.69}$ film on MgO.

The state of strain of the deposited TiC_xO_y film was investigated by using XRD reciprocal space map (RSM) of asymmetric (113) MgO and (113) TiC_xO_y reflections. The vertical (Q_z) and horizontal (Q_x) axes shown in Fig. 2.28 lie along MgO [001] and MgO [110] directions, respectively. Both MgO and TiC_xO_y reflections are almost vertically aligned, showing that TiC_xO_y has strong coherency with MgO. The thermal strain was induced due to a large difference in coefficient of thermal expansion (CTE) of MgO and TiC_xO_y ($\alpha_{\text{MgO}} = 13 \times 10^{-6} \text{ K}^{-1}$ [2.8] and assume $\alpha_{\text{TiCO}} \sim \alpha_{\text{TiC}} = 4.1 \times 10^{-6} \text{ K}^{-1}$ [2.32]). When substrate temperature dropped from 700°C down to room temperature, MgO substrate contracted more than the TiC_xO_y layer, resulting in the generation of compressive strain of -1.3% in the TiC_xO_y layer. It is also noticed that the FWHM of TiC_xO_y film is larger than that of TiN_xO_y films (about \sim two times). This could be due to the fact that thermal strain of TiC_xO_y film (-1.3%) is larger than that of TiN_xO_y films (-0.54%). The corresponding out-of-plane, c , and in-plane, a , lattice parameters can be determined by $c = 3/Q_z$ and $a = \sqrt{2}/Q_x$ [2.33, 34]. Using MgO (113) peak as reference with known lattice parameter ($a = 4.211 \text{ \AA}$), the lattice parameters of $\text{TiC}_{0.47}\text{O}_{0.69}$ can be $c = 4.289 \text{ \AA}$ and $a = 4.228 \text{ \AA}$. The difference between in-plane and out-of-plane lattice parameters ($c/a = 1.0144$) suggests that the $\text{TiC}_{0.47}\text{O}_{0.69}$ film is compressively strained with a tetragonal distortion resulting from the small lattice mismatch of $\text{TiC}_{0.47}\text{O}_{0.69}$ with MgO. Based on the above data and using the Poisson coefficient of TiC ($\nu = 0.17$), the cubic lattice parameter of $\text{TiC}_{0.47}\text{O}_{0.69}$ can be determined approximately to be about 4.271 \AA that lies

in the lattice parameter range between bulk TiC ($a_{\text{TiC}} = 4.317 \text{ \AA}$ from powder diffraction file PDF 89-3828) and bulk TiO ($a_{\text{TiO}} = 4.1770 \text{ \AA}$, PDF 8-117). By using Matthews and Blakeslee model [2.10], the critical thickness can be calculated as 4 nm. According to the data available in literature about the relationship between lattice parameter and stoichiometric coefficients x and y of TiC_xO_y , the lattice parameter is in the range of 4.246-4.280 \AA [2.35, 36] in good agreement with the value determined from XRD data. It also clearly shows that the substitution of oxygen for carbon enables lattice parameter to decrease. The similar behavior of lattice parameter with oxygen content was also reported in previous studies [2.37, 38].

The dislocation density of $\text{TiC}_{0.47}\text{O}_{0.69}$ can be estimated from XRD data in the same way as in TiN_xO_y case and to be around 10^8 cm^{-2} .

Cross-sectional high-resolution TEM analysis was performed to confirm the epitaxial growth of $\text{TiC}_{0.47}\text{O}_{0.69}$ on MgO. Fig. 2.29 shows a sharp interface without any interlayer between $\text{TiC}_{0.47}\text{O}_{0.69}$ and MgO. As can be seen clearly in Fig. 2.29, no misfit dislocations generated at the interface can be identified across the observation range of 15 nm, supporting that the in-plane lattice mismatch between $\text{TiC}_{0.47}\text{O}_{0.69}$ and MgO is very small in consistence with the XRD results.

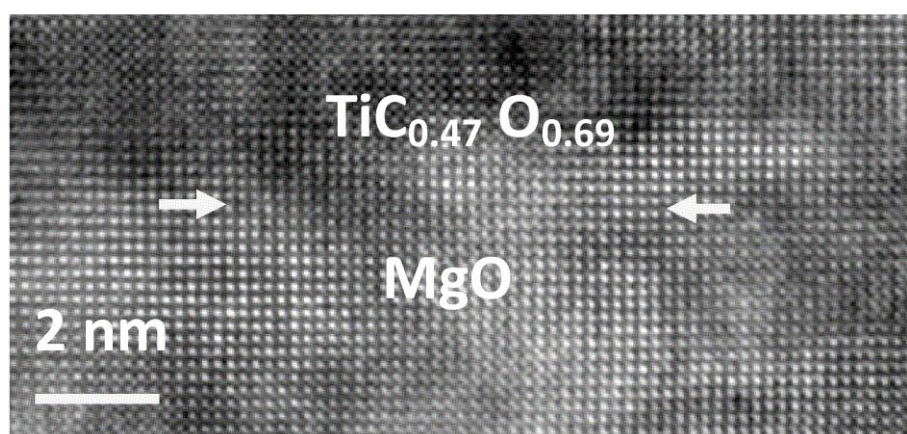


Figure 2.29: Cross-sectional HRTEM image along [100] zone axis showing a sharp interface between $\text{TiC}_{0.47}\text{O}_{0.69}$ and MgO. No misfit dislocations are observed at the interface over the range of 15 nm.

2.4.3. Determining the complete residual stress tensors in epitaxial $\text{TiC}_{0.47}\text{O}_{0.69}/\text{MgO}$ by x-ray diffraction

The complete residual stress tensor of the epitaxial $\text{TiC}_{0.47}\text{O}_{0.69}$ films on MgO was calculated by using x-ray diffraction method as described in section 2.3.3. From the data obtained from Table 2.9 the residual strain tensors of $\text{TiC}_{0.47}\text{O}_{0.69}$ films can be determined:

$$\varepsilon(\%) = \begin{bmatrix} -1.013 & 0.102 & 0.0009 \\ 0.102 & -1.013 & -0.0211 \\ 0.0009 & -0.0211 & 0.415 \end{bmatrix}$$

and the complete residual stress tensor:

$$\sigma(\text{GPa}) = \begin{bmatrix} -5.4921 & 0.3923 & 0.0346 \\ 0.3923 & -5.4921 & -0.08115 \\ 0.0346 & -0.08115 & -0.000175 \end{bmatrix}$$

Table 2.9: XRD measured and calculated strains in 5 $[hkl]$ directions for the $\text{TiC}_{0.47}\text{O}_{0.69}$ film.

(hkl)	002	113	224	022	222
ψ	0	25.23	35.26	45	54.74
ϕ	0	45	45	0	45
2θ	42.105	73.137	124.679	61.761	78.342
$d_{\phi\psi}$	2.145	1.293	0.870	1.501	1.220
d_o	2.136	1.289	0.872	1.510	1.233
$\varepsilon_{\phi\psi}^L(\%)$	0.00415	0.00397	-0.00262	-0.00611	-0.01092

The principal stresses σ_1 , σ_2 , and σ_3 and maximum shear stresses τ_{max} of the $\text{TiC}_{0.47}\text{O}_{0.69}$ film is then calculated and presented in Table 2.10. It is noticed that $\text{TiC}_{0.47}\text{O}_{0.69}$ film is not relaxed even though the film thickness is much larger than

theoretical critical thickness. This could be also explained from the viewpoint of the critical shear stress for dislocation nucleation that is similar to TiN_xO_y case. The theoretically predicted value [2.39] for critical shear stress $\tau_{crit} \sim G/10$ (G is shear modulus of the $\text{TiC}_{0.47}\text{O}_{0.69}$ and can be calculated by using the nanoindentation result in Chapter 3) is listed in Table 2.10. It clearly shows that τ_{crit} is much larger than the maximum shear stresses τ_{max} of the $\text{TiC}_{0.47}\text{O}_{0.69}$ film. Therefore, no stress relaxation caused by dislocation nucleation could be observed in the $\text{TiC}_{0.47}\text{O}_{0.69}$ films

Table 2.10: The principal stress σ_1 , σ_2 , and σ_3 , and maximum shear stress τ_{max} of the $\text{TiC}_{0.47}\text{O}_{0.69}$ film.

	$\text{TiC}_{0.47}\text{O}_{0.69}$
σ_1 (GPa)	0.001374
σ_2 (GPa)	-5.09983
σ_3 (GPa)	-5.88444
τ_{max} (GPa)	2.943
τ_{crit} (GPa)	16.7

2.4.4. Surface morphology

The surface morphology of the $\text{TiC}_{0.47}\text{O}_{0.69}$ film on MgO (001) was examined by AFM. As can be seen in Fig. 2.30, the film surface is very uniform and smooth with root-mean-square (RMS) roughness about 0.18 nm.

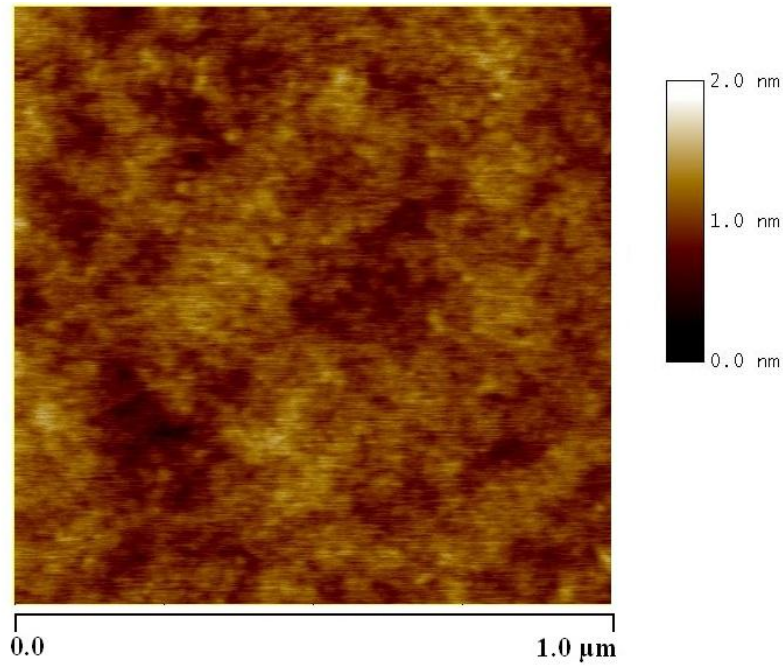


Figure 2.30: AFM image of $\text{TiC}_{0.47}\text{O}_{0.69}$ film surface.

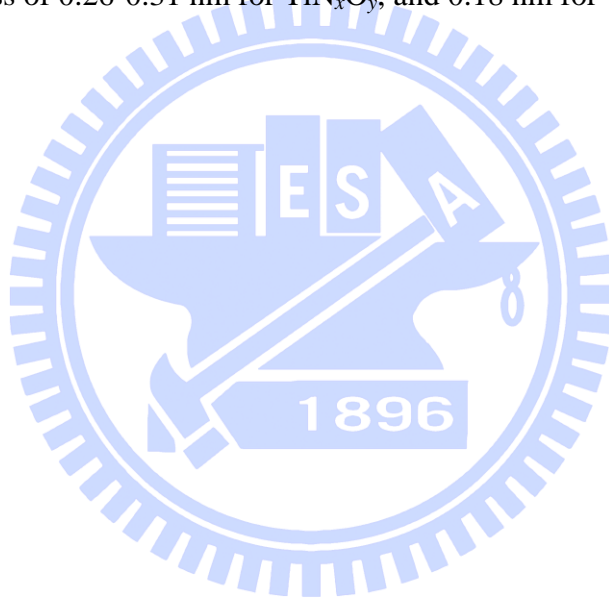
2.4.5. Electronic properties

The resistivity of the $\text{TiC}_{0.47}\text{O}_{0.69}$ film as measured by four-point-probe method is about $137 \mu\Omega\cdot\text{cm}$ that lies in the resistivity range between bulk TiC ($55 \mu\Omega\cdot\text{cm}$) [2.40] and bulk TiO ($190 \mu\Omega\cdot\text{cm}$) [2.41]. This value is smaller than that of epitaxial $\text{TiC}_{0.8}$ films that has been reported to be $200 \mu\Omega\cdot\text{cm}$ [2.42]. The high oxygen content in the $\text{TiC}_{0.47}\text{O}_{0.69}$ film is considered to be responsible for the higher resistivity (more than two times) of $\text{TiC}_{0.47}\text{O}_{0.69}$ compared with that of pure TiC. It is analogous with the case of epitaxial TiN_xO_y , in which the resistivity of oxygen-rich films is two times higher than that of bulk TiN ($21.7 \mu\Omega\cdot\text{cm}$). The $\text{TiC}_{0.47}\text{O}_{0.69}$ film deposited in our case is specially much more electrically conducting compared with polycrystalline TiC_xO_y and TiN_xO_y films that have shown the resistivity in the order of magnitude of $\text{m}\Omega\cdot\text{cm}$ [2.7, 43]. The resistivity of the $\text{TiC}_{0.47}\text{O}_{0.69}$ film is larger than that of TiN_xO_y films in this study ($0.63 < x < 1.11$, $0.1 < y < 0.55$) due to the higher oxygen content in $\text{TiC}_{0.47}\text{O}_{0.69}$ film and the fact that bulk TiN ($21.7 \mu\Omega\cdot\text{cm}$) is more electrically conducting than bulk TiC ($55 \mu\Omega\cdot\text{cm}$).

2.5. Summary

Epitaxial titanium oxynitride TiN_xO_y films with different chemical composition ($0.63 < x < 1.11$, $0.1 < y < 0.55$) and epitaxial $\text{TiC}_{0.47}\text{O}_{0.69}$ film have been successfully grown on MgO (001) substrates using pulsed laser deposition. XRD and TEM show that all the

TiN_xO_y and $\text{TiC}_{0.47}\text{O}_{0.69}$ films have low defect density and good crystallinity (FWHM $\sim 58 - 62$ arcsec for TiN_xO_y and 133 arcsec for $\text{TiC}_{0.47}\text{O}_{0.69}$). All those deposited films have excellent coherency with MgO, i.e. the TiN_xO_y and $\text{TiC}_{0.47}\text{O}_{0.69}$ films are fully strained. The lattice parameters of TiN_xO_y decrease with increased oxygen concentration, and the lattice misfit between TiN_xO_y and MgO substrate decreases as consequence. Hence, the reduction in the residual stress of the TiN_xO_y films is observed when oxygen concentration increases. All the films are electrically conducting with resistivity of 28-53 $\mu\Omega\cdot\text{cm}$ for TiN_xO_y , and 137 $\mu\Omega\cdot\text{cm}$ for $\text{TiC}_{0.47}\text{O}_{0.69}$. Oxygen is also found to be responsible for high resistivity of TiN_xO_y and $\text{TiC}_{0.47}\text{O}_{0.69}$ compared with that of pure TiN and TiC, respectively. It is clearly seen that resistivity of TiN_xO_y increases with oxygen content. The surface of the deposited TiN_xO_y and $\text{TiC}_{0.47}\text{O}_{0.69}$ films is atomically smooth with roughness of 0.26-0.31 nm for TiN_xO_y , and 0.18 nm for $\text{TiC}_{0.47}\text{O}_{0.69}$.



References

- [2.1] D.B. Chrisey, Pulsed Laser Deposition of Thin Films, Wiley, New York, USA, 1994.
- [2.2] L. D'Alessio, A. Galasso, A. Santagata, R. Teghil, A.R. Villani, P. Villani, M. Zaccagnino, Plume dynamics in TiC laser ablation, *Appl Surf Sci*, 208 (2003) 113-118.
- [2.3] L. Escobar-Alarcon, E. Camps, M.A. Castro, S. Muhl, J.A. Mejia-Hernandez, Effect of the plasma parameters on the properties of titanium nitride thin films grown by laser ablation, *Appl Phys a-Mater*, 81 (2005) 1221-1226.
- [2.4] J. Hermann, A.L. Thomann, C. Boulmerleborgne, B. Dubreuil, M.L. Degiorgi, A. Perrone, A. Luches, I.N. Mihailescu, Plasma diagnostics in pulsed-laser TiN layer deposition, *J Appl Phys*, 77 (1995) 2928-2936.
- [2.5] J. Graciani, J.F. Sanz, T. Asaki, K. Nakamura, J.A. Rodriguez, Interaction of oxygen with TiN(001): N \leftrightarrow O exchange and oxidation process, *J Chem Phys*, 126 (2007) 244713.
- [2.6] A. Trenczek-Zajac, M. Radecka, K. Zakrzewska, A. Brudnik, E. Kusior, S. Bourgeois, M.C.M. de Lucas, L. Imhoff, Structural and electrical properties of magnetron sputtered Ti(ON) thin films: The case of TiN doped in situ with oxygen, *J Power Sources*, 194 (2009) 93-103.
- [2.7] M.H. Chan, F.H. Lu, Preparation of titanium oxynitride thin films by reactive sputtering using air/Ar mixtures, *Surf Coat Tech*, 203 (2008) 614-618.
- [2.8] C.S. Shin, D. Gall, N. Hellgren, J. Patscheider, I. Petrov, J.E. Greene, Vacancy hardening in single-crystal TiN_x(001) layers, *J Appl Phys*, 93 (2003) 6025-6028.
- [2.9] Y.O. Ciftci, Y. Unlu, K. Colakoglu, E. Deligoz, The structural, thermodynamical and elastic properties of TiO, *Phys Scripta*, 80 (2009).
- [2.10] J.W. Matthews, A.E. Blakeslee, Defects in epitaxial multilayers: I. Misfit dislocations, *J Cryst Growth*, 27 (1974).
- [2.11] M. Radecka, E. Pamula, A. Trenczek-Zajac, K. Zakrzewska, A. Brudnik, E. Kusior, N.T.H. Kim-Ngan, A.G. Balogh, Chemical composition, crystallographic structure and impedance spectroscopy of titanium oxynitride TiN_xO_y thin films, *Solid State Ionics*, 192 (2011) 693-698.
- [2.12] P. Jin, S. Maruno, Stress-relaxation in reactively sputter-deposited TiO_xN_y films, *Jpn J Appl Phys* 1, 30 (1991) 2058-2062.
- [2.13] J. Graciani, S. Hamad, J.F. Sanz, Changing the physical and chemical properties of titanium oxynitrides TiN_{1-x}O_x by changing the composition, *Phys Rev B*, 80 (2009) 184112-184122.

- [2.14] P. Patsalas, S. Logothetidis, Optical, electronic, and transport properties of nanocrystalline titanium nitride thin films, *J Appl Phys*, 90 (2001) 4725-4734.
- [2.15] P. Gay, P.B. Hirsch, A. Kelly, The estimation of dislocation densities in metals from X-ray data, *Acta Metallurgica*, 1 (1953) 315-319.
- [2.16] B. Liu, R. Zhang, Z.L. Xie, H. Lu, Q.J. Liu, Z. Zhang, Y. Li, X.Q. Xiu, P. Chen, P. Han, S.L. Gu, Y. Shi, Y.D. Zheng, W.J. Schaff, Microstructure and dislocation of epitaxial InN films revealed by high resolution x-ray diffraction, *J Appl Phys*, 103 (2008).
- [2.17] R. Chierchia, T. Bottcher, H. Heinke, S. Einfeldt, S. Figge, D. Hommel, Microstructure of heteroepitaxial GaN revealed by x-ray diffraction, *J Appl Phys*, 93 (2003) 8918-8925.
- [2.18] M. Liu, L.C. Zhang, A. Brawley, P. Atanackovic, S. Duvall, Determining the complete residual stress tensors in SOS hetero-epitaxial thin film systems by the technique of X-Ray diffraction, *Advances in Materials Processing I*, 443 (2010) 742-747.
- [2.19] E. Eiper, A. Hofmann, J.W. Gerlach, B. Rauschenbach, J. Keckes, Anisotropic intrinsic and extrinsic stresses in epitaxial wurtzitic GaN thin film on γ -LiAlO₂(100), *J Cryst Growth*, 284 (2005) 561-566.
- [2.20] L.C. Zhang, *Solid Mechanics for Engineers*, Palgrave Mcmillan 2001.
- [2.21] A. Kelly, G.W. Groves, P. Kidd, *Crystallography and Crystal Deffects*, Wiley, 2000.
- [2.22] M. Oden, M. Ljungcrantz, L. Hultman, Characterization of the induced plastic zone in a single crystal TiN(001) film by nanoindentation and transmission electron microscopy, *J Mater Res*, 12 (1997) 2134-2142.
- [2.23] R. Chowdhury, R.D. Vispute, K. Jagannadham, J. Narayan, Characteristics of titanium nitride films grown by pulsed laser deposition, *J Mater Res*, 11 (1996) 1458-1469.
- [2.24] E. Vogelzang, J. Sjollem, H.J. Boer, J.T.M. Dehosson, Optical-absorption in TiN_xO_y-compounds, *J Appl Phys*, 61 (1987) 4606-4611.
- [2.25] R. Sanjines, H. Tang, H. Berger, F. Gozzo, G. Margaritondo, F. Levy, Electronic-structure of anatase TiO₂ oxide, *J Appl Phys*, 75 (1994) 2945-2951.
- [2.26] H. Ihara, Y. Kumashiro, A. Itoh, K. Meada, Some aspects of ESCA spectra of single crystals and thin films of titanium carbide, *Japanese Journal of Applied Physics*, 12 (1973).
- [2.27] O. Rist, P.T. Murray, Growth of TiC thin-films by pulsed laser evaporation, *Mater Lett*, 10 (1991) 323-328.
- [2.28] D. Simon, C. Perrin, J. Bardolle, *J. Microsc. Spectrosc. Electron*, 1 (1976).

- [2.29] H.K. Jang, S.W. Whangbo, Y.K. Choi, Y.D. Chung, K. Jeong, C.N. Whang, Y.S. Lee, H.S. Lee, J.Y. Choi, G.H. Kim, T.K. Kim, Titanium oxide films on Si(100) deposited by e-beam evaporation, *J Vac Sci Technol A*, 18 (2000) 2932-2936.
- [2.30] H.K. Yao, H.D. Shao, H.B. He, Z.X. Fan, Optical and electrical properties of TiO_x thin films deposited by electron beam evaporation, *Vacuum*, 81 (2007) 1023-1028.
- [2.31] N. Biunno, J. Narayan, S.K. Hofmeister, A.R. Srivatsa, R.K. Singh, Low-temperature processing of titanium nitride films by laser physical vapor-deposition, *Applied Physics Letters*, 54 (1989) 1519-1521.
- [2.32] J.F. Shackelford, W. Alexander, *CRC Materials Science and Engineering Handbook*, Taylor & Francis, 2010.
- [2.33] R.J. Kennedy, P.A. Stampe, Reciprocal space mapping of epitaxial MgO films on SrTiO_3 , *J Cryst Growth*, 207 (1999) 200-205.
- [2.34] C.H. Chen, A. Saiki, N. Wakiya, K. Shinozaki, N. Mizutani, Influence of ultra-thin YSZ layer on heteroepitaxial $\text{CeO}_2/\text{YSZ}/\text{Si}(001)$ films analyzed by X-ray reciprocal space map, *J Cryst Growth*, 219 (2000) 253-262.
- [2.35] A. Afir, M. Achour, N. Saoula, X-ray diffraction study of Ti-O-C system at high temperature and in a continuous vacuum, *J Alloy Compd*, 288 (1999) 124-140.
- [2.36] I.L. Shabalin, V.M. Vishnyakov, D.J. Bull, S.G. Keens, L.F. Yamshchikov, L.I. Shabalin, Initial stages of oxidation of near-stoichiometric titanium carbide at low oxygen pressures, *J Alloy Compd*, 472 (2009) 373-377.
- [2.37] T. Hashishin, T. Yamamoto, M. Ohyanagi, Z.A. Munir, Simultaneous synthesis and densification of titanium oxycarbide, $\text{Ti}(\text{C},\text{O})$, through gas-solid combustion, *J Am Ceram Soc*, 86 (2003) 2067-2073.
- [2.38] L. Marques, H.M. Pinto, A.C. Fernandes, O. Banakh, F.V.M.M.D. Ramos, Optical properties of titanium oxycarbide thin film, *Appl Surf Sci*, 255 (2009) 5615-5619.
- [2.39] D. Hull, D.J. Bacon, *Introduction to dislocations*, Butterworth-Heinemann, 2011.
- [2.40] P. Ettymayer, W. Lengauer, *Carbides: Transition Metal Solid State Chemistry*, Wiley, 1994.
- [2.41] C.N.R. Rao, W.E. Wahnsiedler, J.M. Honig, Plasma resonance in TiO , VO and NbO , *J Solid State Chem*, 2 (1970) 315-317.
- [2.42] L. Norin, S. McGinnis, U. Jansson, J.O. Carlsson, Low temperature deposition of epitaxial titanium carbide on $\text{MgO}(001)$ by co-evaporation of C_{60} and Ti, *J Vac Sci Technol A*, 15 (1997) 3082-3085.

[2.43] A.C. Fernandes, P. Carvalho, F. Vaz, S. Lanceros-Mendez, A.V. Machado, N.M.G. Parreira, J.F. Pierson, N. Martin, Property change in multifunctional TiCxOy thin films: Effect of the O/Ti ratio, *Thin Solid Films*, 515 (2006) 866-871.



Chapter 3

Nanoindentation studies of epitaxial TiN_xO_y (001) and TiC_xO_y (001) films on MgO (001)

3.1. Introduction

Nanoindentation is one of the most commonly used techniques to examine the mechanical properties of a material at the nanoscale. This technique uses a high-resolution equipment to measure the load-displacement response, and a number of mechanical properties can be deduced from this curve [3.1-3]. For this reason, the method has become a primary technique for determining the mechanical properties of thin films and small structural features. The two mechanical properties measured most frequently using indentation techniques are the hardness, H , and the elastic modulus, E .

In Chapter 2, we reported the successful growth of high-quality epitaxial (001) titanium oxynitride and titanium oxycarbide films on MgO substrates by PLD. In this chapter, we characterize the mechanical properties of our films by using nanoindentation. The nanoindentation data were then analyzed to exclude the substrate effect, and the reliable values for hardness (H) and elastic modulus (E) can be obtained. The effect of chemical composition and residual stress on hardness and elastic modulus was also investigated for TiN_xO_y films.

This chapter is organized as follows: First of all the brief theory of nanoindentation is presented. Next, the substrate effect and the limitation of the conventional Oliver-Pharr method on the extracting of substrate effect are shown. Section 3.4 describes the details of Li and Vlassak model as well its advantages over the others. Finally, in section 3.5, we present our application of Li and Vlassak model for determining hardness and Young's modulus of epitaxial TiN_xO_y and TiC_xO_y films grown on MgO (001) substrate.

3.2. The brief theory of nanoindentation

As the indenter is pressed into the sample, both elastic and plastic deformations occur, which results in the formation of a hardness impression conforming to the shape of the

indenter. During indenter withdrawal, only the elastic portion of the displacement is recovered, which facilitates the use of an elastic solution in modeling the contact process [3.1, 4, 5]. Figure 3.1 shows a typical load–displacement curve and the deformation pattern of an elastic–plastic sample during and after indentation.

Nanoindentation hardness is defined as the indentation load divided by the projected contact area of the indentation. From the load-displacement curve, hardness can be obtained at the peak load as:

$$H = \frac{P_{\max}}{A} \quad (4.1)$$

where A is the projected contact area:

$$A_c = 24.56h_c^2 + C_1h_c^1 + C_2h_c^{1/2} + C_3h_c^{1/4} + \dots + C_8h_c^{1/128} \quad (4.2)$$

where $C_1 - C_8$ are constants. The lead term describes a perfect Berkovich indenter, the others describe deviations from the Berkovich geometry due to blunting of the tip [3.1].

The contact depth can be estimated from the load-displacement data::

$$h_c = h - h_s = h - \varepsilon \frac{P_{\max}}{S} \quad (4.3)$$

where ε is a constant that depends on the geometry of the indenter. Important values are: $\varepsilon = 0.72$ for a conical indenter, $\varepsilon = 0.75$ for a Berkovich indenter [3.1].

The elastic modulus of the indented sample can be inferred from the initial unloading contact stiffness $S = dP/dh$:

$$S = 2\beta \sqrt{\frac{A}{\pi}} E_r \quad (4.4)$$

$$E_r = \frac{1-\nu^2}{E} + \frac{1-\nu_i^2}{E_i}$$

where β is a constant that depends on the geometry of the indenter ($\beta = 1.034$ for a Berkovich indenter) [3.1], E_r is the reduced elastic modulus, which accounts for the fact that elastic deformation occurs in both the sample and the indenter, and E and ν are the elastic modulus and Poisson's ratio for the sample, respectively, and E_i and ν_i are the same quantities for the indenter.

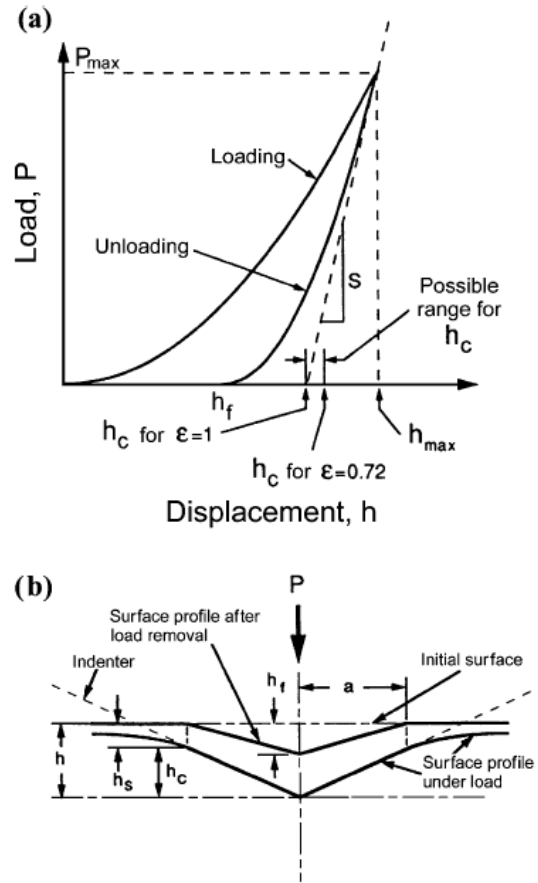


Figure 3.1: (a) A typical load-displacement curve and (b) the deformation pattern of an elastic-plastic sample during and after indentation [3.6].

Oliver & Pharr have also developed a technique that offers a significant improvement in nanoindentation measurement: continuous stiffness measurement (CSM) [3.1, 7-9]. All details about the CSM technique are presented in Appendix A.

3.3. Substrate effects and the limitation of conventional Oliver-Pharr method

The above analysis of the Oliver-Pharr method was initially developed for analyzing indentations in bulk materials, not for films on substrates, and no information about a possible substrate is included in the analysis. The Oliver-Pharr method is, however, frequently used to interpret indentations performed on thin films in an attempt

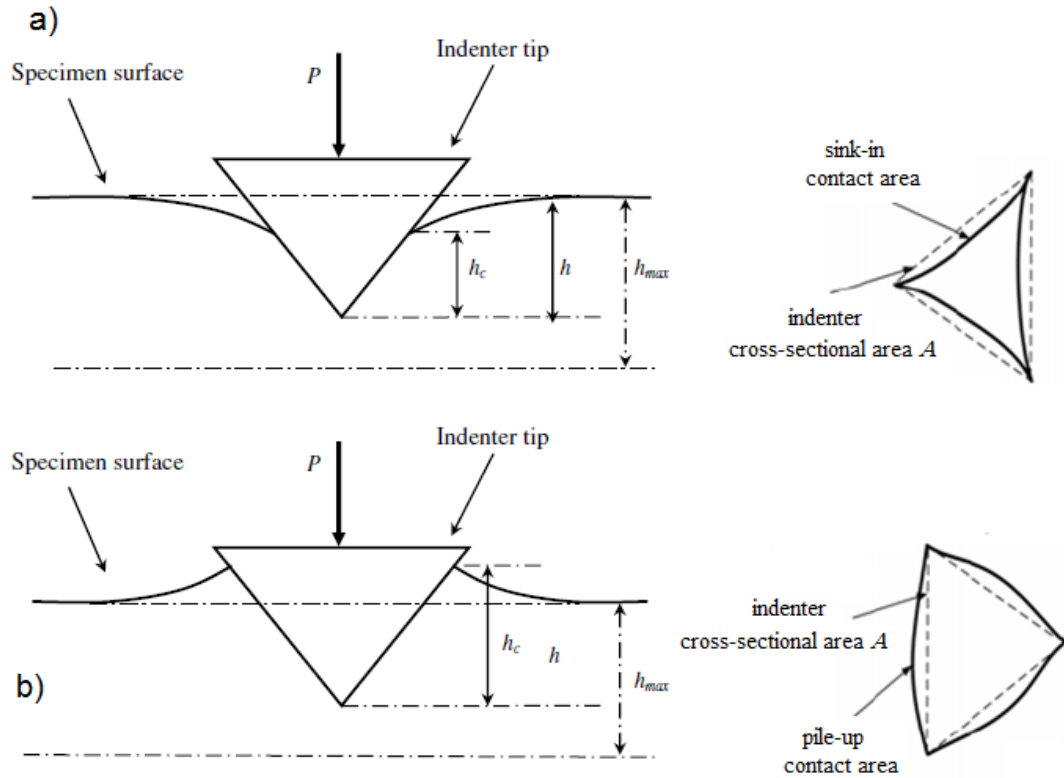


Figure 3.2: Schematic diagrams of a) sink-in (hard films/soft substrates) and b) pile-up (soft films/hard substrates) indentations.

to obtain approximate film properties regardless of the effect of substrate properties on the measurement. The accuracy of such a measurement depends on the film and substrate properties and on the indentation depth as a fraction of the total film thickness. In general, the error due to the substrate effect increases with increasing indentation depth and with increasing elastic mismatch between film and substrate [3.10-13]. To minimize the effect of the substrate on the measurement, the indentation depth is often limited to less than 10% of the film thickness. This empirical rule is not always reliable, especially if the elastic mismatch between film and substrate is large. The 10% rule is also not useful for thin films when experimental issues make it difficult to obtain accurate results for shallow indentations. Both effects lead to errors in determining the contact area. As shown in Fig. 3.2, hard films on soft substrates, the film material sinks in to the sides of the indenter during indentation, causing a smaller contact area than the predicted indenter contact area A . In the case of soft, compliant films on hard, stiff substrates, the film material piles up against the sides of the indenter during indentation, causing a larger contact area than

indenter contact area A . Thus, the Oliver and Pharr approach underestimates and overestimates the hardness when sink-in and pile-up occur, respectively. Evidently there exists a need for a method that can be used to analyze thin-film indentation data for indentation depths where the substrate effect cannot be ignored. Thus, there is a need for a method that can be used to analyze thin-films over a wide range of indentation depths and with large elastic mismatch between the film and the substrate.

Many authors have developed models that attempted to count the substrate effects, including King [3.14], Saha and Nix [3.13], Yu *et al.* [3.15], Chen and Vlassak [3.16], Han *et al.* [3.17], and Li and Vlassak [3.18], among which the Li and Vlassak model has shown advantages and improved accuracy over the others. In this chapter, therefore, we employed the model developed by Li and Vlassak to analyze the nanoindentation data, and then extract hardness and Young's modulus of our thin films.

3.4. Li and Vlassak model

Li and Vlassak presented a new data analysis procedure based on Yu's elastic solution to derive the projected contact area in an elasto-plastic indentation and to extract the elastic modulus and hardness of a film on a substrate. The detail of elastic indentation problem and solution in Yu's analysis and some useful results from Yu's solution are presented in Appendix B.

In an elastic indentation, the film thickness is well defined and application of the Yu solution is relatively straightforward. In elastoplastic indentations, however, the film between indenter and substrate is thinned as a result of plastic flow and it is not immediately clear what thickness should be used. Saha and Nix [3.13] used the initial film thickness subtracted by the indentation depth, $t - h$, whereas Han [3.17] simply used t . Li and Vlassak showed that the local thinning effect is well captured if an effective film thickness, t_{eff} , is defined as: $t_{\text{eff}} = t - \eta h$, where the dimensionless function η quantifies the local thinning of the film as a result of plastic deformation of the film. This parameter depends on the mechanical properties of film and substrate, as well as on the shape of the indenter.

Given Yu's solution, it is now possible to calculate the instantaneous contact radius a during an indentation by two ways. First, the contact radius at this position can also be calculated from the S - a relationship derived from Yu's solution, if the values of η and

the indentation modulus of the film, E_f , are assumed. We refer to the value of a calculated using this approach as the theoretical value of a^* .

Second, if the values of η and the indentation modulus of the film E_f are known or assumed, the contact radius can also be determined by solving the following implicit equation numerically:

$$a = \sqrt{\frac{1}{\pi} f \left[h - \xi \left(\frac{a}{t_{\text{eff}}|_h}, \frac{M_f}{M_s} \right) \varepsilon \frac{P}{S} \right]}$$

where f is the area function of the indenter tip and ξ is obtained from Yu's solution. We refer to this value of the contact radius as the experimental value of a_{exp} .

If the contact stiffness is known at each point of the indentation loading curve (e.g., from a continuous stiffness measurement) then the two measures of the a can be calculated at every point of the indentation loading curve resulting in two continuous S - a curves. If the assumed values of η and the indentation modulus E_f are correct, both curves overlap. In actual practice, E_f and η can be treated as free parameters that need to be varied to achieve the best possible overlap between the two S - a curves (i.e., to minimize the mean square error between the two curves). Once E_f and η have been determined, the contact radius a can be calculated and the hardness is found as $H = P / \pi a^2$. A detailed step-by-step outline to implement all these procedures is presented as follows:

I. STEPS TO GET THE EXPERIMENTAL a - S RELATION AS A FUNCTION OF E_f and η

- (i) Assume initial values of E_f and η .
- (ii) Calculate the effective thickness t_{eff} for a given point on the indentation loading curve: $t_{\text{eff}} = t - \eta h$.
- (iii) Obtain the experimental value of the contact radius at this loading point by solving the following implicit equation numerically:

$$a = \sqrt{\frac{1}{\pi} f \left[h - \xi \left(\frac{a}{t_{\text{eff}}|_h}, \frac{M_f}{M_s} \right) \varepsilon \frac{P}{S} \right]}$$

where f is the area function of the indenter tip and ξ is obtained from Yu's solution.

- (iv) Calculate the reduced stiffness to remove the compliance of the indenter tip using:

$$S_r = \left(\frac{1}{S} - \frac{1}{S_{\text{tip}}} \right)^{-1}$$

where $S_{\text{tip}} = 2a_{\text{exp}}M_{\text{tip}}$ and $M_{\text{tip}} = 1146.6$ GPa for a diamond indenter.

- (v) Repeat steps (ii)–(iv) for every point of the indentation loading curve to obtain the experimental $[S_r, a_{\text{exp}}]$ relation for the values of E_f and η assumed in step (i).

II. STEPS TO GET THE THEORETICAL S - a RELATION AS A FUNCTION OF FILM MODULUS AND η

- (vi) Assume the same initial values of E_f and η as in step (i).
- (vii) Calculate the effective thickness t_{eff} for a given point on the indentation loading curve: $t_{\text{eff}} = t - \eta h$.
- (viii) Calculate the elastic S - a relation directly from Yu's solution by using Eqs. (B.5)–(B.9) (see Appendix B).
- (ix) Calculate the theoretical contact area a^* where the contact stiffness equals S_r [as from step (iv)], from the elastic S - a relation.
- (x) Repeat step (vi)–(ix) for every point of the indentation loading curve to obtain the theoretical $[S_r, a^*]$ for the values of E_f and η assumed in step (i).

III. STEPS TO EXTRACT UNKNOWN FILM MODULUS

- (xi) Compute the χ^2 , sum of the squares of the residues, using the following formula:

$$\chi^2 = \sum (a_{\text{exp}} - a^*)^2$$

- (xii) Find the values of E_f and η that minimize χ^2 using a standard optimization algorithm.

3.5. Application of Li and Vlassak model for determining hardness and Young's modulus of epitaxial TiN_xO_y and TiC_xO_y films grown on MgO (001) substrate

3.5.1. Experimental

The mechanical properties of all TiN_xO_y and TiC_xO_y films grown with conditions described in chapter 2 were characterized using a MTS Nanoindenter XP system with a diamond Berkovich tip with an apex angle of 65.30° and a tip radius of about 20 nm. The continuous-stiffness-measurement (CSM) mode was used with a harmonic force at 45 Hz imposed on the increasing load. The Berkovich tip shape (area function) was calibrated using a fused silica specimen to ensure the accuracy of the indentation measurements. The indentation procedure consisted of five steps: loading to the specified indentation depth, holding the indenter at the peak load for 10 s, unloading 5 % of the peak load, holding the indenter at this point for 60 s for thermal drift correction, and unloading completely. Five indentations were performed for each deposited films and MgO substrate, and the average results of the group are presented here. The indentation data of all TiN_xO_y /MgO and $\text{TiC}_{0.47}\text{O}_{0.69}$ /MgO samples were then analyzed using the procedure given by Li and Vlassak as described detail in section 3.4, while the indentation data of MgO substrates were analyzed using the method of Oliver and Pharr [3.1]. All the analysis procedure was carried out by using Matlab software. Li and Vlassak [3.18] have also shown that Poisson's ratio of the film has a minor effect on nanoindentation results. In the analysis procedure, therefore, we used the Poisson's ratio of TiN ($\nu_{\text{TiN}} = 0.22$) for all as-deposited TiN_xO_y films and the Poisson's ratio of TiC ($\nu_{\text{TiC}} = 0.17$). The results were also compared with the ones calculated by the commonly used method of Oliver and Pharr [3.1].

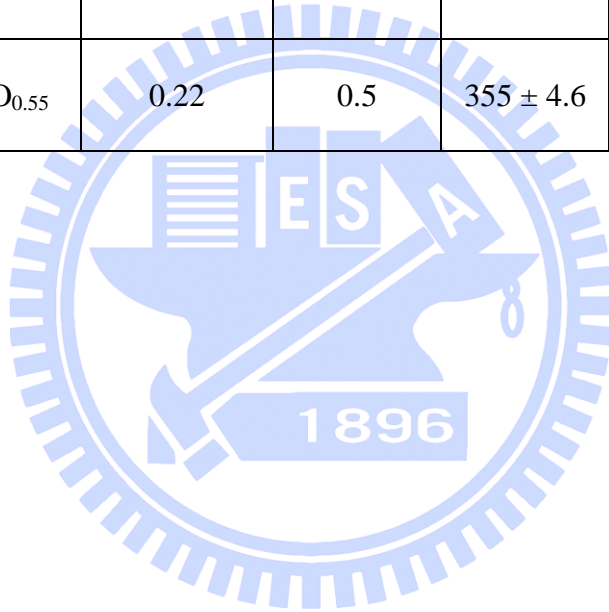
3.5.2. Results and discussions

A. TiN_xO_y /MgO

Nanoindentation results of all the TiN_xO_y films and MgO are summarized in Table 3.1. It is noticed that the extraction of the indentation modulus of the film relies on a fit of the experimental S - a relationship with the theoretical result derived from Yu's solution using E_f and η as fitting parameters. One may wonder if two or more distinct combinations of E_f and η could give a comparable quality of fit. To verify that, we present a contour plot of the sum of the squares of the residues χ^2 (Fig. 3.3) for all the TiN_xO_y films, where the fitting parameters have been varied over a wide range. The plot shows a clear minimum corresponding to the optimum combination of E_f and η . Evidently, the optimum fitting parameters are well defined and unique over the range of parameters shown in Fig. 3.3.

Table 3.1: The hardness and Young's modulus of TiN_xO_y films calculated by using Li-Vlassak method.

Sample	Poisson's ratio	η	E (GPa)	H (GPa)
MgO	0.19	-	300 ± 3.2	10 ± 1
$\text{TiN}_{1.11}\text{O}_{0.10}$	0.22	0.5	430 ± 5.7	26 ± 1.2
$\text{TiN}_{0.97}\text{O}_{0.23}$	0.22	0.5	400 ± 7.3	23 ± 1.7
$\text{TiN}_{0.81}\text{O}_{0.38}$	0.22	0.5	385 ± 5.2	21 ± 1.3
$\text{TiN}_{0.63}\text{O}_{0.55}$	0.22	0.5	355 ± 4.6	17 ± 1.2



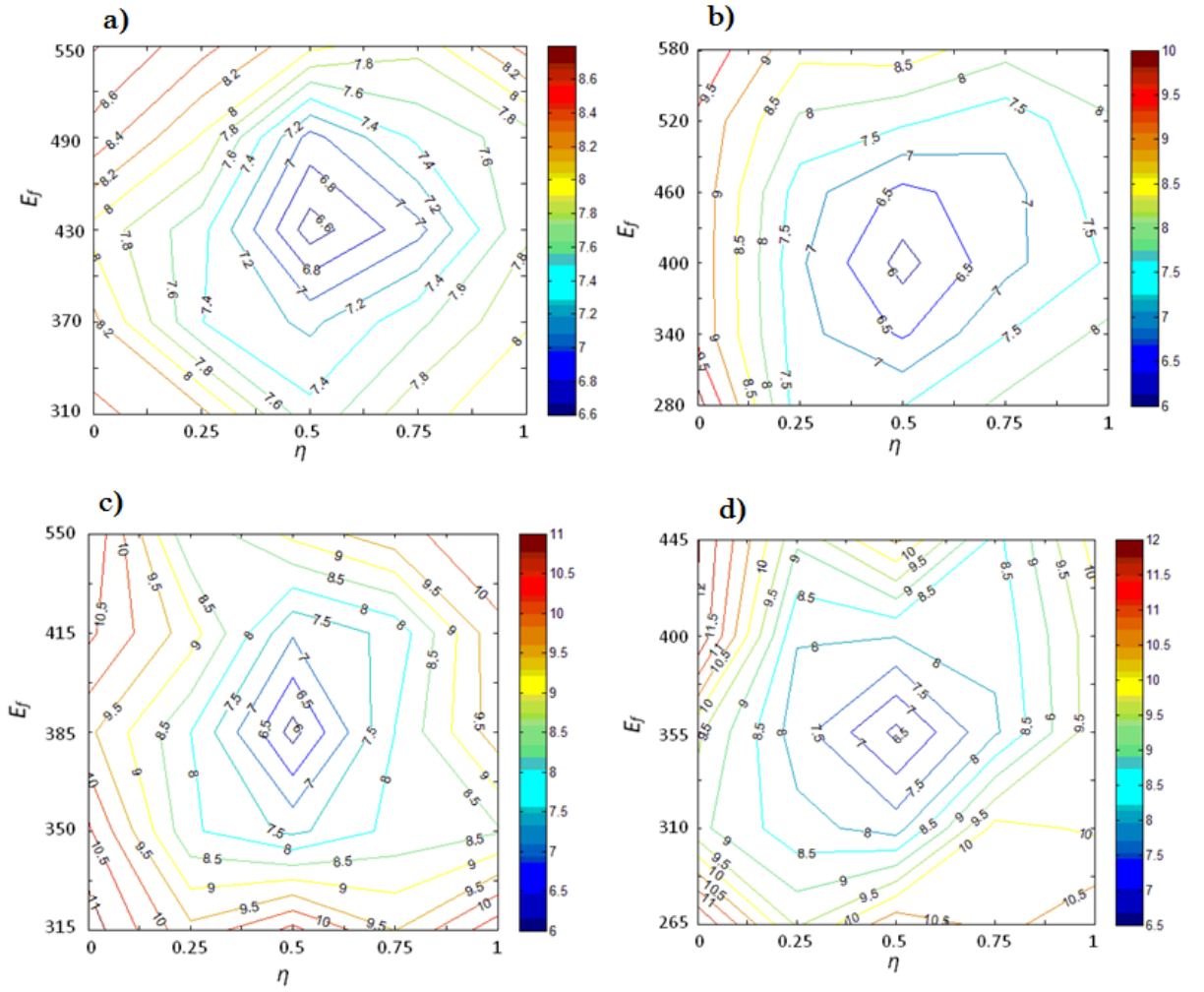


Figure 3.3: Contour plot of $\log_{10}(\chi^2)$ as a function of E_f and η for the $\text{TiN}_x\text{O}_y/\text{MgO}$ sample. The unit of χ^2 is in nm^2 .

The hardness and Young's modulus of MgO obtained using Oliver-Pharr method are in good agreement with the reported values in the literatures [3.19, 20]. The results show that the hardness and Young's modulus of the deposited TiN_xO_y films are in range of 17 - 26 GPa and 355 - 450 GPa, respectively. The TiN_xO_y film with small oxygen concentration shows that the Young's modulus is closed to the reported value of stoichiometric single-crystal TiN (001) with $E \sim 445 \pm 38$ GPa, while the hardness value is larger than that of stoichiometric single-crystal TiN (001) with $H \sim 20 \pm 0.8$ GPa [3.21]. To evaluate the accuracy of the obtained results, we also calculate H and E using conventional Oliver-Pharr method. Figure 3.4 illustrates the Young's modulus of the TiN_xO_y films obtained using Li-Vlassak approach in comparison with the values obtained

from the Oliver-Pharr method as a function of indentation depth divided by film thickness h/t . As expected, the Oliver-Pharr moduli are noisy and fall sharply at small indentation depths and quickly approach the substrate modulus with increasing h/t due to the substrate effect that not excluded from the calculated results. In contrast, the film moduli obtained from Li-Vlassak method, in which the substrate effect caused by film-substrate elastic mismatch was taken into account, are constant throughout a wide range of indentation depths. Figure 3.5 shows the hardness of TiN_xO_y films as a function of indentation depth calculated using both Li-Vlassak and Oliver-Pharr methods, together with the hardness value of MgO substrate. Both TiN_xO_y hardness curves rise from zero value at shallow indentation depths, reach the maximum values as indentation depth increases. It is noticed that the hardness curves drop off and reach the substrate hardness value rapidly when the indenter approaches film/substrate interface due to the extensive plastic deformation in the soft substrate. However, the maximum hardness values obtained from Oliver-Pharr analysis are significant lower compared with that of Li-Vlassak method due to the effect of the soft substrate. Moreover, the hardness curves obtained by Li-Vlassak model show a small plateau. This indicates that the effect of film-substrate elastic mismatch is significantly excluded from the results obtained by Li-Vlassak analysis. Therefore the values for mechanical properties of TiN_xO_y films by using Li-Vlassak method and presented in Table 3.1 are reliable.

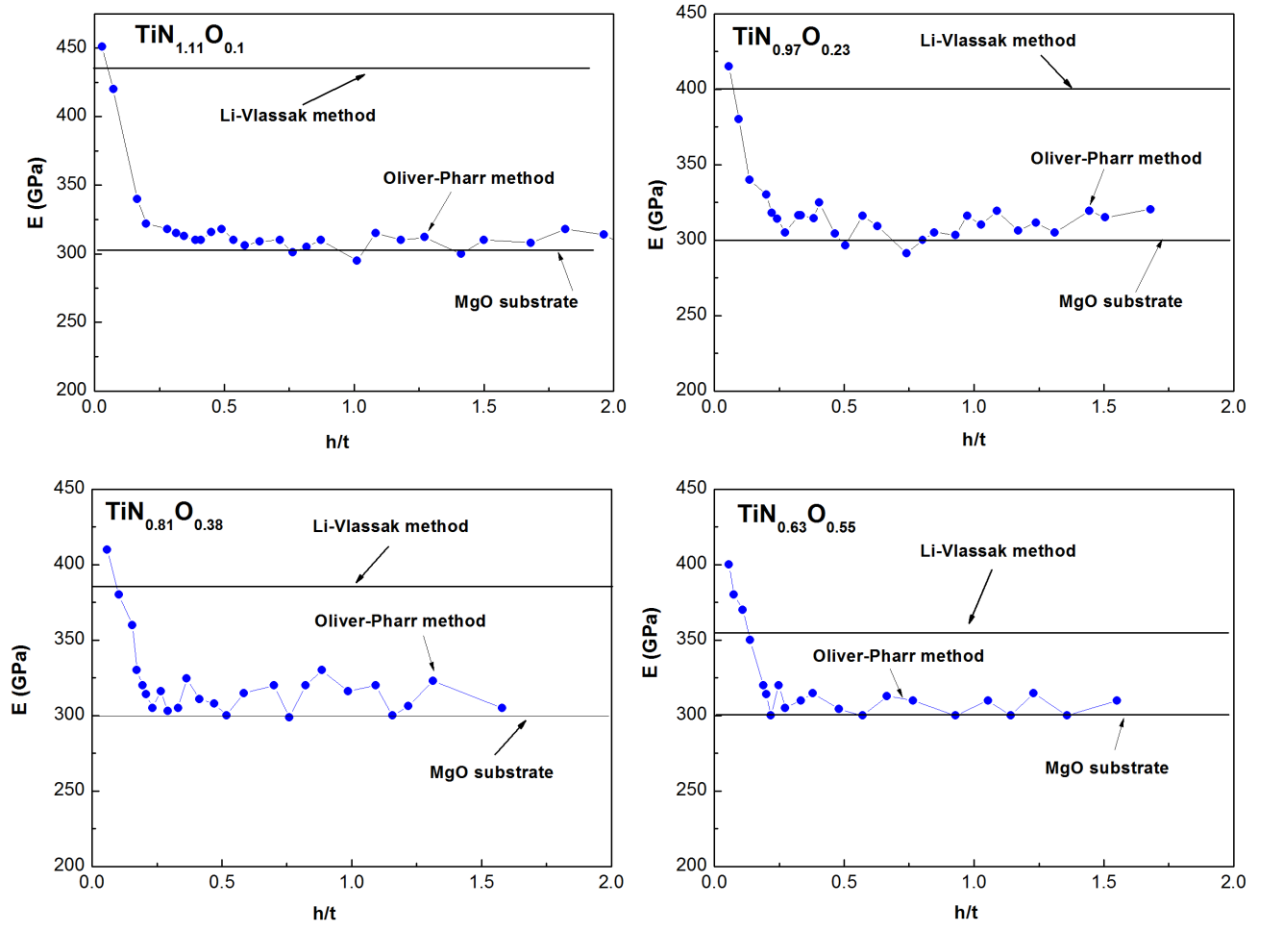


Figure 3.4: The Young's modulus of TiN_xO_y films as a function of h/t (indentation depth/film thickness) obtained by using Li-Vlassak method, together with the Young's modulus of MgO substrate. The results obtained using Oliver-Pharr method are presented for comparison.

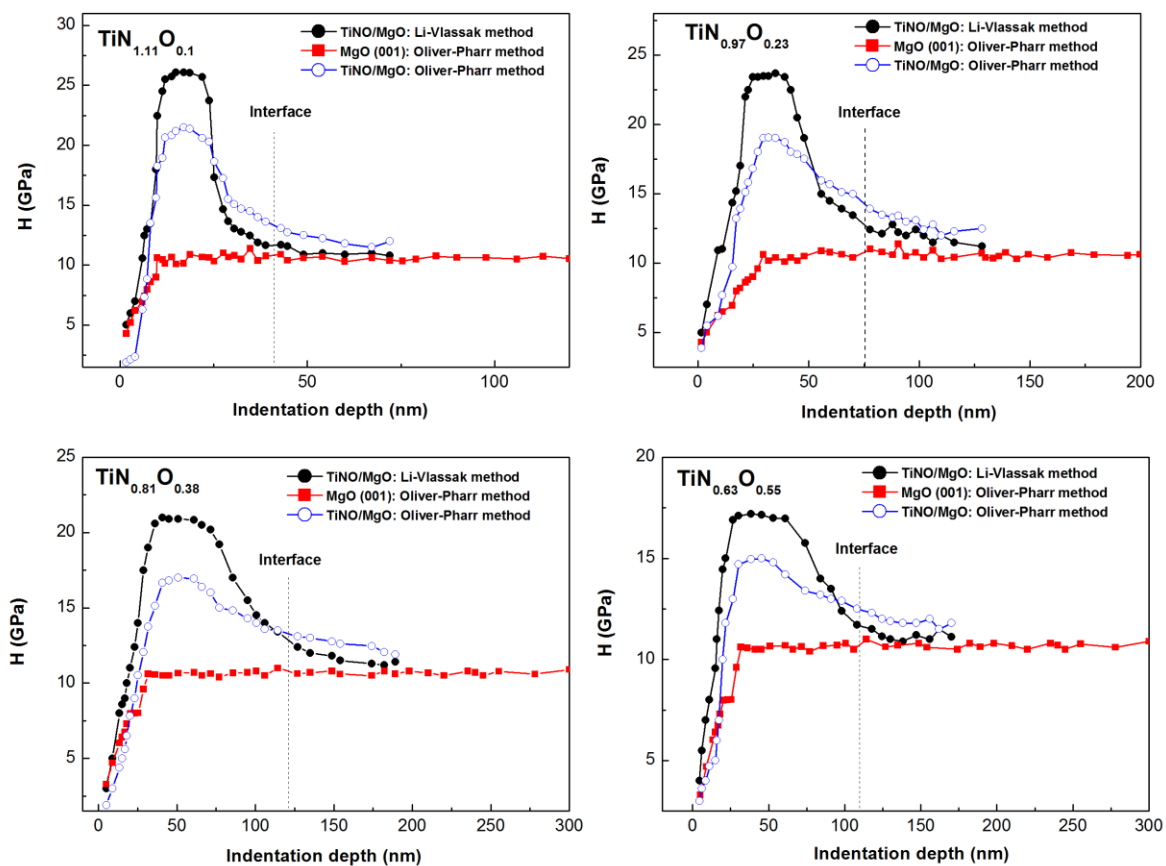


Figure 3.5: The hardness of TiN_xO_y films as a function of indentation depth calculated by using both Li-Vlassak and Oliver-Pharr methods. The hardness value of MgO substrate is also included.

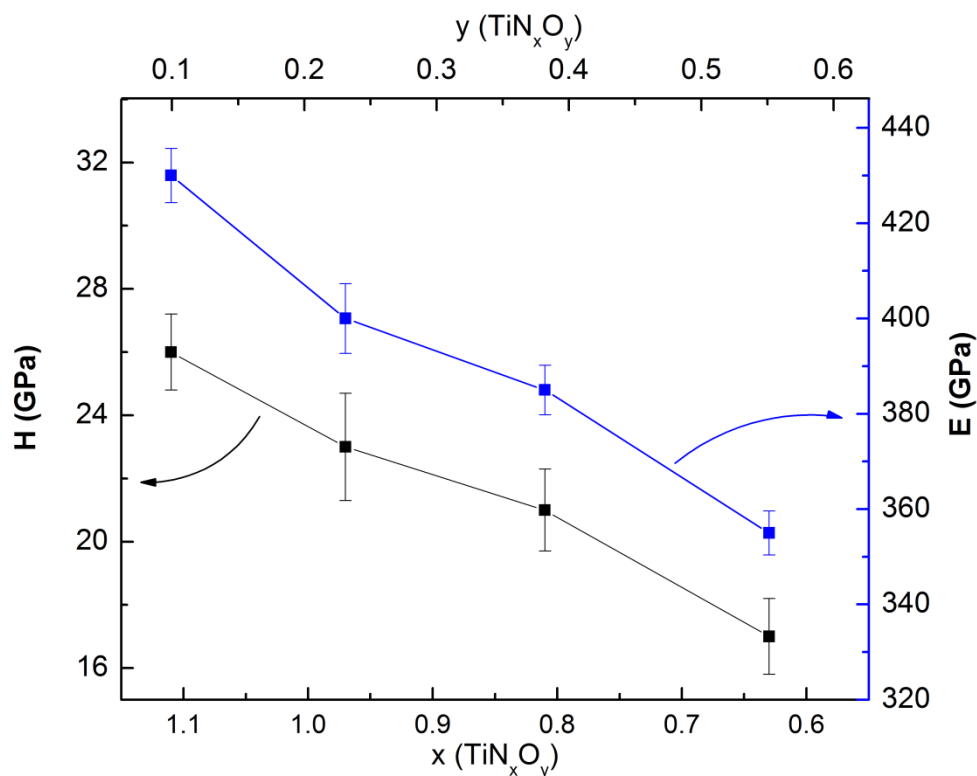


Figure 3.6: The dependence of the hardness and Young's modulus of TiN_xO_y films on chemical composition.

It is clearly seen that both hardness and Young's modulus of the TiN_xO_y films decrease with increasing oxygen content and increase with increasing nitrogen content (Fig. 3.6). The maximum values of H and E were found for the TiN_xO_y film with the highest nitrogen content. The minimum values of H and E were found for the TiN_xO_y film with the highest oxygen content. Similar behavior of H and E with chemical composition has also been reported for polycrystalline, textured, and bulk TiN_xO_y [3.22-25]. Therefore, the increase of oxygen can be considered as a softening factor on the TiN_xO_y films. The dependence of the mechanical properties of TiN_xO_y on oxygen and nitrogen content can be explained by the changes in covalent and ionic contribution to the bond in the TiN_xO_y compound. Indeed, authors in ref. [3.24] have calculated the changes in the electronic structure induced by the geometrical structure and composition $\text{TiN}_x\text{O}_{1-x}$. Figure 3.7 shows the evolution of the density of states (DOS) with x for NaCl structure of $\text{TiN}_x\text{O}_{1-x}$. The gap between the 2p (N/O) and 3d (Ti) bands increases as the concentration of O increases, and decreases as the concentration of N increases. The separation between the

bands $2p$ and $3d$ as the concentration of O increases leads to a decrease in the $2p$ - $3d$ mixing, which is related to the covalent contribution to the bond, and consequently the nature of the bond has a higher ionic contribution that causes bond strength to decrease (The bond lengths can be considered as constants due to that the bond length decreases by less than 0.5% when x decreases from 1.1 to 0.63 and y increases from 0.1 to 0.55). Similarly, the increase of nitrogen content leads to an increase in covalent character of the bond, and thereby bond strength, increases. Hence, hardness and elastic modulus increases as the amount of nitrogen increases, and decreases as the amount of oxygen increases.

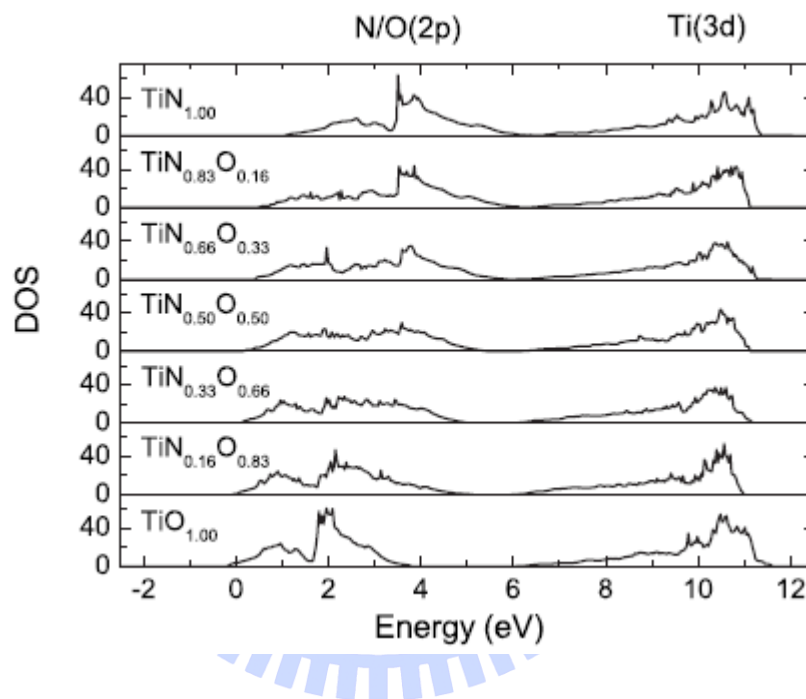


Figure 3.7: Evolution of the DOS of the titanium oxynitrides (NaCl structure) with the composition [3.24].

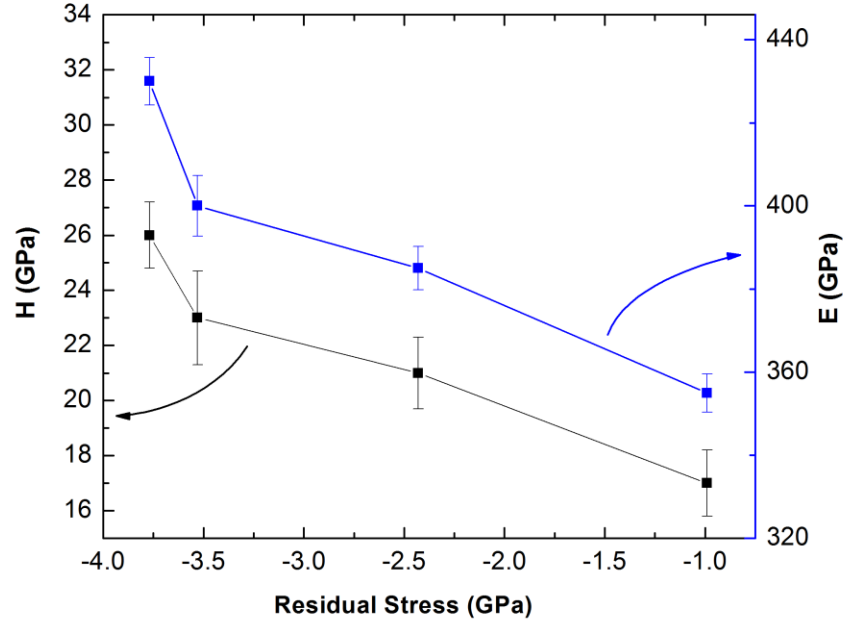


Figure 3.8: Evolution of the hardness and Young's modulus of TiN_xO_y films with residual compressive stress.

It is also noticed that in-plane residual compressive stress also has an influence on the mechanical properties of TiN_xO_y films. As shown in Fig. 3.8, H and E increase linearly as residual compressive stress increases. The same behavior of H and E with residual compressive stress was also reported for polycrystalline TiN_xO_y film [3.25] and other materials [3.26-29]. The change in mechanical properties of TiN_xO_y films with different residual compressive stresses can be explained from the viewpoint of atomic bonding force to interatomic spacing [3.28-30]. It is known that atoms locate at a balanced interatomic separation r_0 , and the spacing changes under a force. If the interatomic separation exceeds the maximum value r_{max} under an applied force over the maximum atomic bonding force F_{max} , atomic bonds will be broken, and plastic deformation may initiate. The residual compressive stress will make interatomic spacing compressed, and a larger applied force is needed to break bonds. Therefore, an increase in H and E can be expected when residual compressive stress increases.

B. $\text{TiC}_{0.47}\text{O}_{0.69}/\text{MgO}$

Nanoindentation results of the $\text{TiC}_{0.47}\text{O}_{0.69}$ film and MgO are summarized in Table 3.2. Similar to the TiN_xO_y case, the contour plot of the sum of the squares of residues χ^2 (Fig.

3.9) for the $\text{TiC}_{0.47}\text{O}_{0.69}$ film reveals a clear and unique combination of E_f and η over the range of parameters that gives the minimum value of χ^2 .

Table 3.2: The hardness and Young's modulus of $\text{TiC}_{0.47}\text{O}_{0.69}$ film calculated by using Li-Vlassak method.

Sample	Poisson's ratio	η	E (GPa)	H (GPa)
MgO	0.19	-	300 ± 3.2	10 ± 1
$\text{TiC}_{0.47}\text{O}_{0.69}$	0.17	0.5	390 ± 6.4	21 ± 1.7

The nanoindentation results show that the hardness and Young's modulus of the deposited $\text{TiC}_{0.47}\text{O}_{0.69}$ film are 21 ± 1.7 GPa and 390 ± 6.4 GPa, respectively. Those values are smaller than that of bulk TiC (001) with $H \sim 26 - 31$ GPa and $E \sim 439$ GPa [3.31, 32].

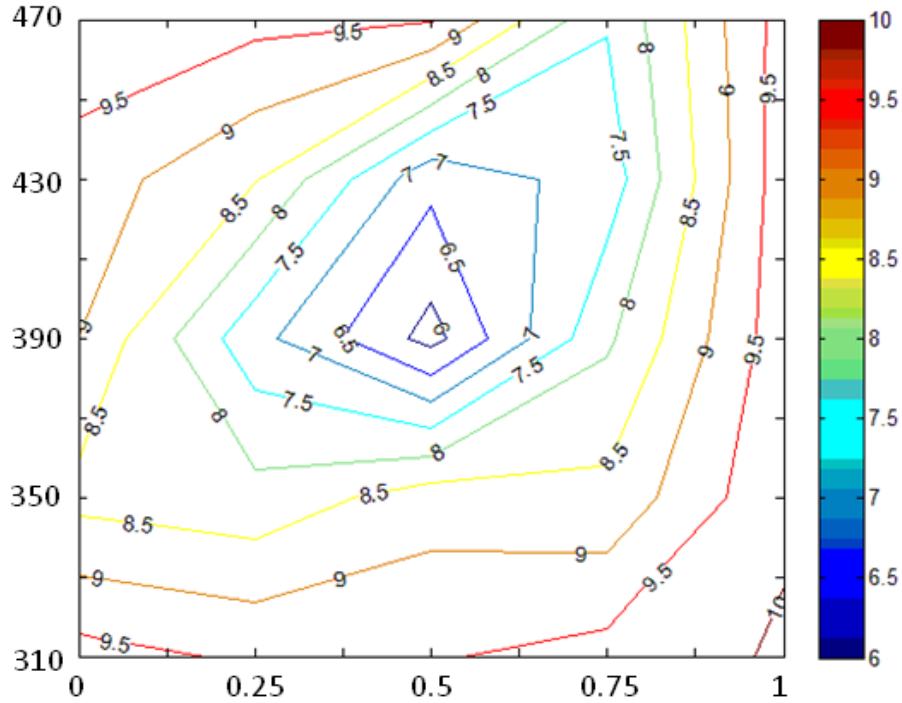


Figure 3.9: Contour plot of $\log_{10}(\chi^2)$ as a function of E_f and η for the $\text{TiC}_{0.47}\text{O}_{0.69}/\text{MgO}$ sample. The unit of χ^2 is in nm^2 .

We also compare H and E calculated by Li-Vlassak with those determined by conventional Oliver-Pharr method. Figure 3.10 and Figure 3.11 show the hardness and Young's modulus of $\text{TiC}_{0.47}\text{O}_{0.69}$ film as functions of indentation depth and h/t calculated using both Li-Vlassak and Oliver-Pharr methods. Similar to the TiN_xO_y case, the Li-Vlassak modulus of $\text{TiC}_{0.47}\text{O}_{0.69}$ film is constant throughout a wide range of indentation depths contrasted with values calculated by Oliver-Pharr method; and the maximum hardness obtained from Li-Vlassak method is higher compared with that of Oliver-Pharr analysis due to the effect of the soft substrate.

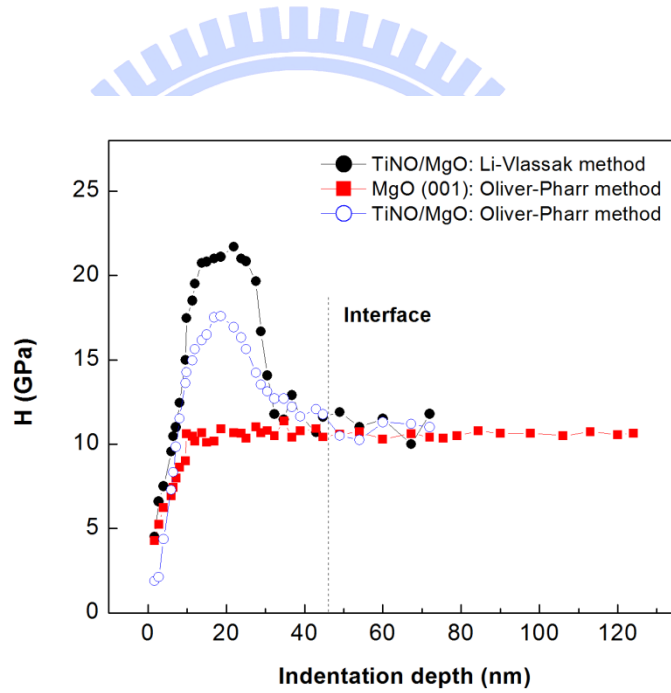


Figure 3.10: The hardness of $\text{TiC}_{0.47}\text{O}_{0.69}$ film as a function of indentation depth calculated by using both Li-Vlassak and Oliver-Pharr methods. The hardness value of MgO substrate is also included.

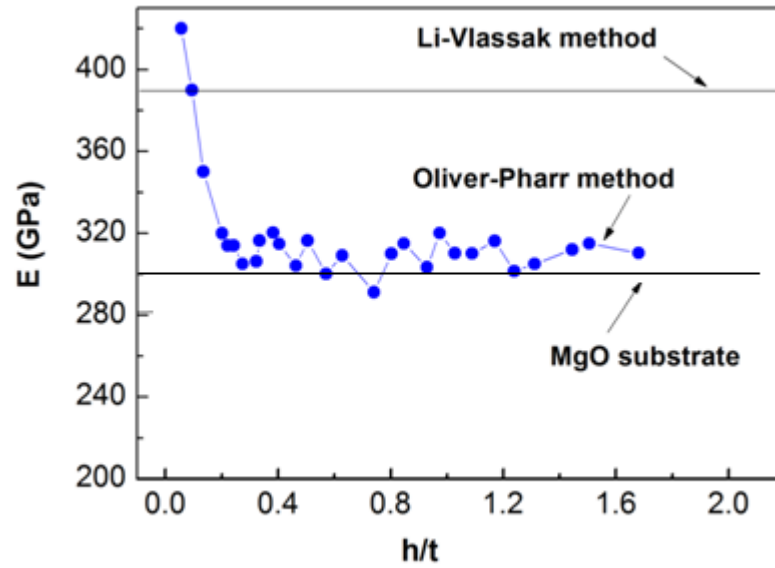


Figure 3.11: The Young's modulus of $\text{TiC}_{0.47}\text{O}_{0.69}$ film as a function of h/t (indentation depth/film thickness) obtained by using Li-Vlassak method, together with the Young's modulus of MgO substrate. The results obtained using Oliver-Pharr method are presented for comparison.

3.6. Summary

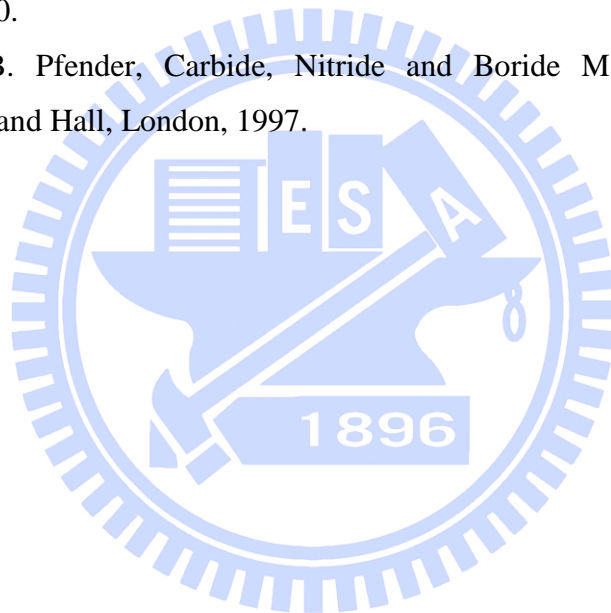
Li-Vlassak method for analysis of nanoindentation of hard TiN_xO_y and $\text{TiC}_{0.47}\text{O}_{0.69}$ films on soft MgO substrate provides the reliable values for hardness and Young's modulus. High-quality epitaxial TiN_xO_y films with different composition ($0.63 < x < 1.11$, $0.1 < y < 0.55$) shows the hardness and Young's modulus of about 17 - 26 GPa and 355 - 430 GPa, respectively, while the $\text{TiC}_{0.47}\text{O}_{0.69}$ film shows the value of $H \sim 21 \pm 1.7$ GPa and $E \sim 390 \pm 6.4$ GPa. Chemical composition and residual compressive stress have strong influence on the mechanical properties of the TiN_xO_y films. Both H and E are found to decrease as oxygen content increases, and increase as nitrogen content increases. With increasing residual compressive stress, the hardness and Young's modulus of TiN_xO_y also increase. Both TiN_xO_y and $\text{TiC}_{0.47}\text{O}_{0.69}$ show the lower values of H and E compared with that of TiN and TiC, respectively.

References

- [3.1] W.C. Oliver, G.M. Pharr, An improved technique for determining hardness and elastic-modulus using load and displacement sensing indentation experiments, *J Mater Res*, 7 (1992) 1564-1583.
- [3.2] W.C. Oliver, G.M. Pharr, Measurement of hardness and elastic modulus by instrumented indentation: Advances in understanding and refinements to methodology, *J Mater Res*, 19 (2004) 3-20.
- [3.3] A.C. Fischer-Cripps, *Nanoindentation*, Springer Verlag, 2004.
- [3.4] B. Bhushan, *Handbook of Micro/Nano Tribology*, CRC Press, 1999.
- [3.5] G.M. Pharr, Measurement of mechanical properties by ultra-low load indentation, *Mat Sci Eng a-Struct*, 253 (1998) 151-159.
- [3.6] X.D. Li, B. Bhushan, A review of nanoindentation continuous stiffness measurement technique and its applications, *Mater Charact*, 48 (2002) 11-36.
- [3.7] J.B. Pethica, W.C. Oliver, Tip surface interactions in STM and AFM, *Phys Scripta*, T19a (1987) 61-66.
- [3.8] J.B. Pethica, W.C. Oliver, Thin films: stresses and mechanical properties, in: J.C. Bravman, W.D. Nix, D.M. Barnett, D.A. Smith (Eds.) *Materials Research Society Symposium Proceedings*, Pittsburgh, PA, 1989, pp. 13-23.
- [3.9] B.N. Lucas, W.C. Oliver, J.E. Swindeman, Fundamentals of nanoindentation and nanotribology, in: N.R. Moody, W.W. Gerberich, N. Burnham, S.P. Baker (Eds.) *Materials Research Society Symposium Proceedings*, Warrendale, PA, 1998, pp. 3.
- [3.10] B.D. Fabes, W.C. Oliver, R.A. Mckee, F.J. Walker, The determination of film hardness from the composite response of film and substrate to nanometer scale indentations, *J Mater Res*, 7 (1992) 3056-3064.
- [3.11] G.M. Pharr, W.C. Oliver, Measurement of thin-film mechanical-properties using nanoindentation, *Mrs Bull*, 17 (1992) 28-33.
- [3.12] J. Mencik, D. Munz, E. Quandt, E.R. Weppelmann, M.V. Swain, Determination of elastic modulus of thin layers using nanoindentation, *J Mater Res*, 12 (1997) 2475-2484.
- [3.13] R. Saha, W.D. Nix, Effects of the substrate on the determination of thin film mechanical properties by nanoindentation, *Acta Mater*, 50 (2002) 23-38.
- [3.14] R.B. King, Elastic analysis of some punch problems for a layered medium, *Int J Solids Struct*, 23 (1987) 1657-1664.

- [3.15] H.Y. Yu, S.C. Sanday, B.B. Rath, The effect of substrate on the elastic properties of films determined by the indentation test - axisymmetrical boussinesq problem, *J Mech Phys Solids*, 38 (1990) 745-764.
- [3.16] X. Chen, J.J. Vlassak, Numerical study on the measurement of thin film mechanical properties by means of nanoindentation, *J Mater Res*, 16 (2001) 2974-2982.
- [3.17] S.M. Han, R. Saha, W.D. Nix, Determining hardness of thin films in elastically mismatched film-on-substrate systems using nanoindentation, *Acta Mater*, 54 (2006) 1571-1581.
- [3.18] H. Li, J.J. Vlassak, Determining the elastic modulus and hardness of an ultra-thin film on a substrate using nanoindentation, *J Mater Res*, 24 (2009) 1114-1126.
- [3.19] D. Caceres, I. Vergara, R. Gonzalez, Y. Chen, E. Alves, Nanoindentation on MgO crystals implanted with lithium ions, *Nucl Instrum Meth B*, 191 (2002) 154-157.
- [3.20] K. Kurosaki, D. Setoyama, J.J. Matsunaga, S. Yamanaka, Nanoindentation tests for TiO₂, MgO, and YSZ single crystals, *J Alloy Compd*, 386 (2005) 261-264.
- [3.21] H. Ljungcrantz, M. Oden, L. Hultman, J.E. Greene, J.E. Sundgren, Nanoindentation studies of single-crystal (001)-, (011)-, and (111)-oriented TiN layers on MgO, *J Appl Phys*, 80 (1996) 6725-6733.
- [3.22] M. Braic, M. Balaceanu, A. Vladescu, A. Kiss, V. Braic, G. Epurescu, G. Dinescu, A. Moldovan, R. Birjega, M. Dinescu, Preparation and characterization of titanium oxy-nitride thin films, *Appl Surf Sci*, 253 (2007) 8210-8214.
- [3.23] J.M. Chappe, N. Martin, J. Lintymer, F. Sthal, G. Terwagne, J. Takadoum, Titanium oxynitride thin films sputter deposited by the reactive gas pulsing process, *Appl Surf Sci*, 253 (2007) 5312-5316.
- [3.24] J. Graciani, S. Hamad, J.F. Sanz, Changing the physical and chemical properties of titanium oxynitrides TiN_{1-x}O_x by changing the composition, *Phys Rev B*, 80 (2009) 184112-184122.
- [3.25] F. Vaz, P. Cerqueira, L. Rebouta, S.M.C. Nascimento, E. Alves, P. Goudeau, J.R. Riviere, K. Pischow, J. de Rijk, Structural, optical and mechanical properties of coloured TiN_xO_y thin films, *Thin Solid Films*, 447 (2004) 449-454.
- [3.26] L. Karlsson, L. Hultman, J.E. Sundgren, Influence of residual stresses on the mechanical properties of TiC_xN_{1-x} (x=0, 0.15, 0.45) thin films deposited by arc evaporation, *Thin Solid Films*, 371 (2000) 167-177.

- [3.27] A. Mani, P. Aubert, F. Mercier, H. Khodja, C. Berthier, P. Houdy, Effects of residual stress on the mechanical and structural properties of TiC thin films grown by RF sputtering, *Surf Coat Tech*, 194 (2005) 190-195.
- [3.28] Y.C. Huang, S.Y. Chang, C.H. Chang, Effect of residual stresses on mechanical properties and interface adhesion strength of SiN thin films, *Thin Solid Films*, 517 (2009) 4857-4861.
- [3.29] A. Mallik, B.C. Ray, Residual stress and nanomechanical properties of sonoelectrodeposited Cu films, *Surf Eng*, 27 (2011) 551-556.
- [3.30] T.H. Courtney, *Mechanical Behavior of Materials*, McGrill-Hill, New York USA, 1990.
- [3.31] J.F. Shackelford, W. Alexander, *CRC Materials Science and Engineering Handbook*, Taylor & Francis, 2010.
- [3.32] P.C. Kong, B. Pfender, *Carbide, Nitride and Boride Materials Synthesis and Processing*, Chapman and Hall, London, 1997.



Chapter 4

Stability and etching of titanium oxynitride in hydrogen microwave plasma

4.1. Introduction

Microwave plasma is a type of plasma that has high frequency electromagnetic radiation in the GHz range. It is capable of exciting electrodeless gas discharges, and is especially well suited to generate large-area plasmas of high plasma density. It is also noticed that microwave plasma can produce a plasma density up to 10^{12} cm^{-3} [4.1] that is much higher than that in RF plasma. Hence, microwave plasma is more useful for etch study because it may have a faster etching rate compared with that of RF plasma which has been widely used in many processing. Hydrogen in microwave can produce a high density of ion and atomic hydrogen flux [4.2, 3].

In this chapter, we report the study of the effects of pure hydrogen microwave plasma on the stability and etching of TiN_xO_y films as function of gas pressure and treating time. The high-quality epitaxial TiN_xO_y films were used in our study due to the lack of bulk single crystals TiN_xO_y , and it can avoid the complicated etch effects from grain boundaries and orientations in polycrystalline films. The etch mechanism and the changes in chemical composition and surface morphology were also investigated.

4.2. Experimental

The deposited titanium oxynitride films with composition of $\text{TiN}_{0.97}\text{O}_{0.23}$ and thickness of 76 nm (sample B (see chapter 2 for details)) were placed on a molybdenum holder and loaded into a 2.45 GHz/5 kW ASTeX-type microwave plasma chemical vapor deposition (MPCVD) [4.4]. The plasma was then generated under hydrogen gas ambient with flow rate of 300 sccm and microwave power of 1000 W. Samples were placed in the active glow discharge region. The hydrogen plasma treatment was done at gas pressure varied from 40 to 80 Torr and treatment time varied from 30 to 150 minutes (details in Table 4.1). In the reactor, the increase in pressure caused the volume of the plasma ball to

shrink [4.1], which in turn increased the plasma density. During the treatment, the substrate temperature determined by optical pyrometer increased from 900 to 1100°C with pressure increasing from 40 to 80 Torr. After the plasma was switched off, the sample was cooled down to room temperature in about 10 minutes. The surface morphology of the films was then examined with atomic force microscopy (AFM) (D3100, Digital Instruments Inc.). $\text{TiN}_x\text{O}_y/\text{MgO}$ interface was observed in cross-section by using scanning electron microscopy (SEM) (JEOL JSM-6500F-SEM). Chemical compositions of the TiN_xO_y films before and after plasma treatment were determined by employing x-ray photoelectron spectroscopy (XPS) (ULVAC-PHI, PHI Quantera SXM) using a monochromatic Al $K\alpha$ radiation source. High-resolution x-ray diffractometry (Bede D1) was used to investigate the change in the crystallinity, thickness, density, and strain state of the thin films. The Bede D1 system was equipped a two-bounce Si 220 channel-cut collimator crystal, a dual channel Si 220 analyzer crystal (DCA), and $\text{CuK}\alpha_1$ radiation ($\lambda = 1.5406 \text{ \AA}$).

Table 4.1: Hydrogen plasma treatment parameters.

Sample	H ₂ gas flow (sccm)	Microwave power (W)	Pressure (Torr)	Time (min)
1	300	1000	40	90
2	300	1000	60	30
3	300	1000	80	30
4	300	1000	80	60
5	300	1000	80	150

4.3. Stability and etching of TiN_xO_y : morphology and mechanism

The surface morphology of as-grown and hydrogen plasma treated samples 1, 2, 3, 4, and 5 (Table 4.1) was examined with AFM. As seen clearly in Fig. 4.1, the surface of the TiN_xO_y film treated for 90 min at pressure of 40 Torr (sample 1) shows almost no etch pits, but it becomes slightly rougher with root-mean-square (rms) roughness of 0.48 nm

compared with 0.32 nm for the as-grown TiN_xO_y . However, TiN_xO_y became etched at pressure of 60-80 Torr for treatment time of 30 min (Fig. 4.2). The AFM image in the inset of Fig.4.2a as well as its corresponding section analysis show that the etched TiN_xO_y surface morphology appears with inverse pyramid etch pits which have the edges of the pyramid parallel to $\langle 100 \rangle$ direction of the epitaxial TiN_xO_y films. The origin of pyramid etch pits in TiN_xO_y films can be explained as in NaCl structure [4.5]. Mendelson [4.5] has demonstrated that in NaCl crystal, the inverse pyramid etch pits are produced at intersections of dislocations with the surface. Similarly, it is possible that the inverse pyramid etch pits appear in our TiN_xO_y films are associated with dislocation sites. Indeed, as shown later in XRD data, the dislocation density can be estimated from x-ray rocking curve broadening (full width half at maximum ~ 230 arcsec) to be around 10^8 cm^{-2} that is similar to the etch pit density observed on AFM images. AFM images also show that no particles left on the surface, indicating the complete removal of etch product after etching.

The distribution of etch size and etch depth for samples treated at different pressure and etching time are shown in histograms of Fig. 4.3. It is found that the etch size and the etch depth are increased with pressure and etching time. The average etch size and etch depth increase from 141 nm and ~ 15 nm to 175 nm and 20 nm, respectively, when pressure increases from 60 Torr to 80 Torr for the same etching time of 30 min. For longer treatment (at 80 Torr), the average etch size increases from 175 (30 min) to 342 nm (60 min) and 861 nm (150 min), while the average etch depth increases from 20 nm (30 min) to 34 nm (60 min) and 76 nm (150 min). The results reveal very low lateral and vertical etch rate of about 4.7-5.7 nm/min and 0.48-0.56 nm/min respectively. Moreover, the lateral etch rate is much higher than the vertical etch rate (~ 10 times), indicating the preference for lateral etching of hydrogen plasma. Mendelson [4.5] has shown that in NaCl crystal, if the strained region around a dislocation is etched away or disappears, the etch pit is not etched further in depth but is enlarged laterally. Therefore, the anisotropic etching can be expected in TiN_xO_y as shown above. Cross-sectional SEM of sample 5 (Fig. 4.2d) shows the etch pit with a depth reaching the $\text{TiN}_x\text{O}_y/\text{MgO}$ interface, implying that TiN_xO_y can be fully etched at 80 Torr with etching time over 150 min.

From the AFM images shown above it is clear that TiN_xO_y films remain stable at hydrogen gas pressure under 40 Torr but are etched at pressure above 60 Torr with the etch rate increased with pressure. It is also noticed that microwave plasma can produce a plasma density up to 10^{12} cm^{-3} [4.1] that is much higher than that in RF plasma. Hence,

microwave plasma is more useful for etch study because it may have faster etching rate under etching condition as above. Moreover, TiN_xO_y is stable under pressure below 40 Torr of microwave plasma, indicating that TiN_xO_y can survive in RF plasma which has been widely used in many processing.

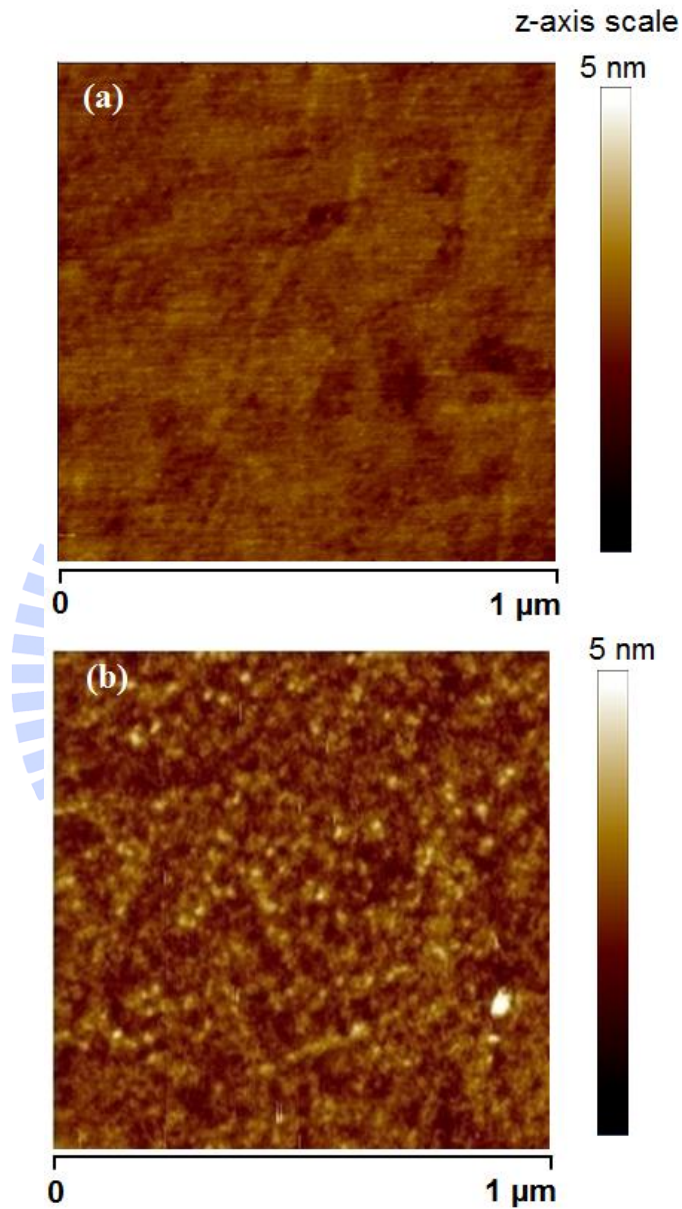


Figure 4.1: AFM images of (a) as-grown TiN_xO_y films and (b) TiN_xO_y film after hydrogen plasma treatment at pressure of 40 Torr for 90 min (sample 1).

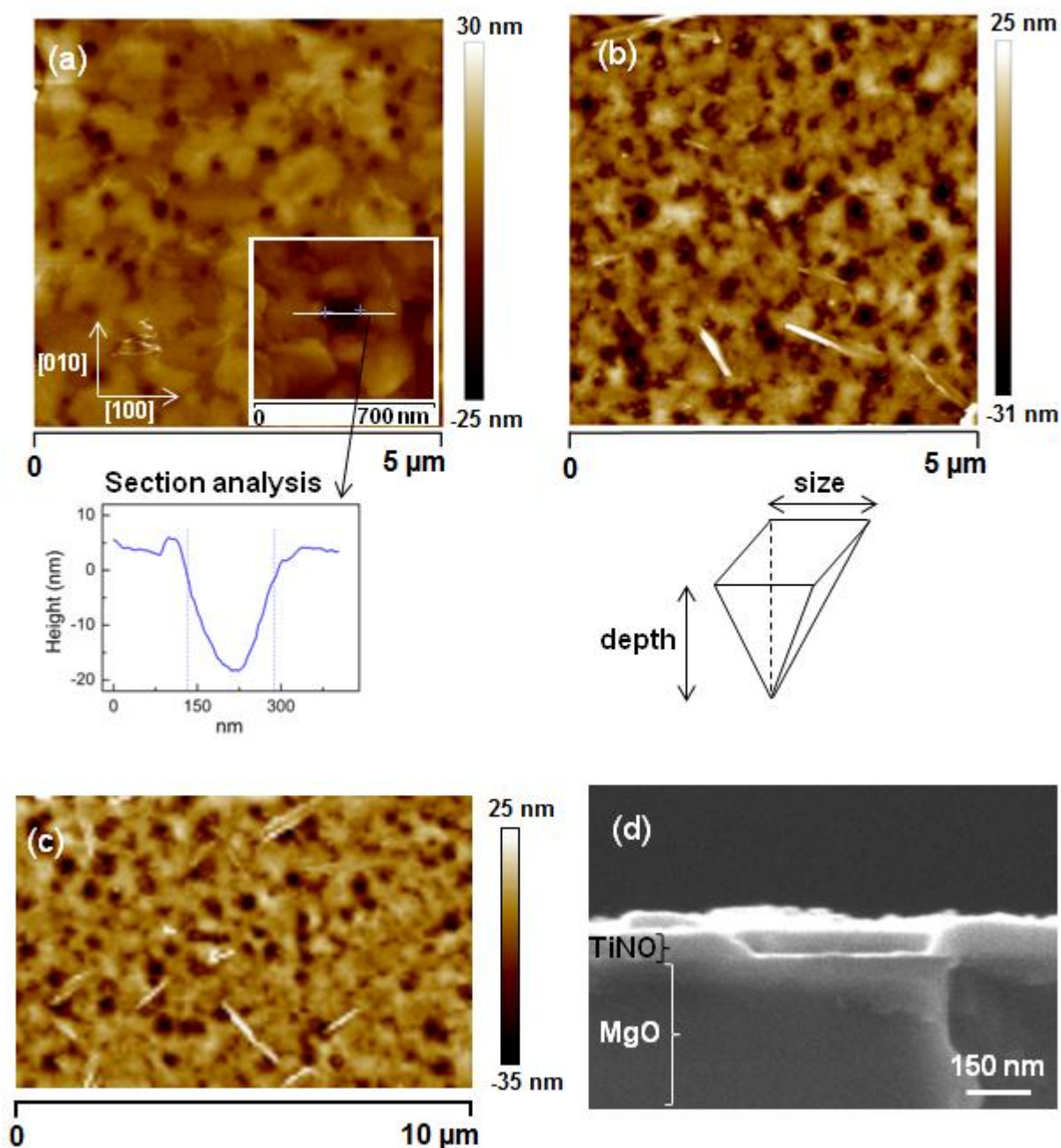


Figure 4.2: AFM images of TiN_xO_y after etching at (a) 60 Torr for 30 min (sample 2), 80 Torr for (b) 30 min (sample 3) and (c) 60 min (sample 4); (d) cross-sectional SEM image of TiN_xO_y after etching at 80 Torr for 150 min (sample 5).

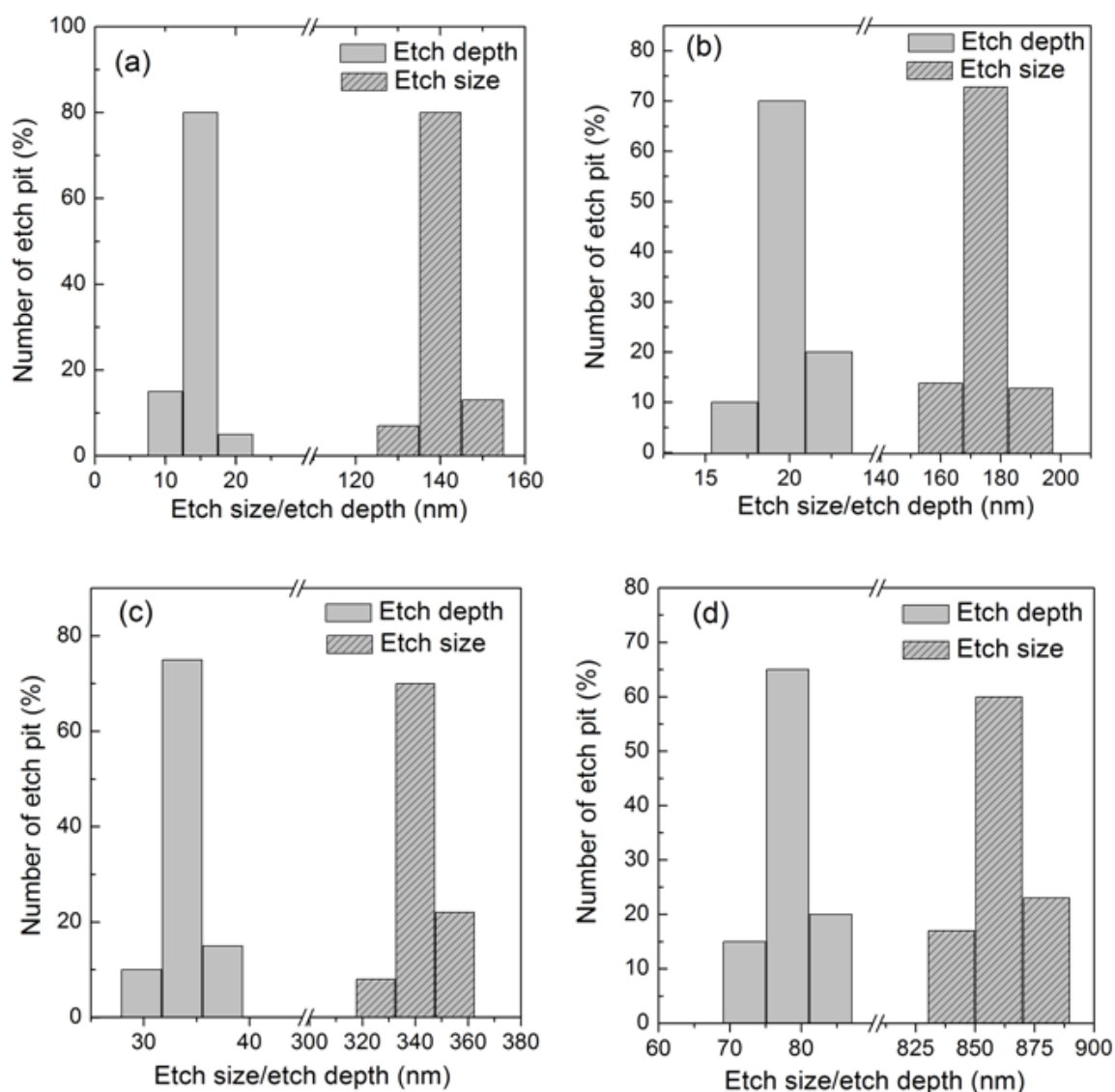
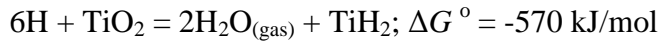
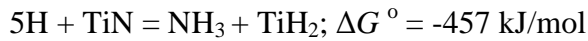


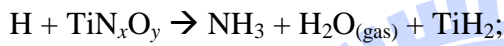
Figure 4.3: The distribution of the etch size and etch depth at (a) 60 Torr for 30 min, 80 Torr for (b) 30 min, (c) 60 min, and (d) 150 min.

Exploration of the etch mechanism of TiN_xO_y film under hydrogen plasma may be helpful for understanding the effects of pressure and treatment time. The possible etch mechanism can be proposed based on thermodynamics, which allows us to define feasible chemical reactions which may occur in hydrogen plasma. As shown later in XPS data, as-grown TiN_xO_y films can be considered to consist of three components of titanium nitride, titanium oxynitride, and titanium dioxide. Moreover, hydrogen atoms and /or ions, generated by the dissociation of molecular hydrogen in plasma, are very powerful reductants that can reduce titanium oxide and nitride. Indeed, for example, at

experimental temperature of 1000°C, the reduction of titanium oxide and nitride to the most common titanium hydride can be as the following:



All the reactions are thermodynamically favorable due to their negative Gibbs free energy ΔG° values [4.6]. Therefore, the reaction of TiN_xO_y in hydrogen plasma can be simply described as follows:



Titanium hydride (TiH_2) has a relative low melting temperature of 450°C; however, there is a lack of information on its vapor pressure. In general, a substance with low melting temperature has a high vapor pressure. Therefore, TiH_2 could possess a high vapor pressure and it has a high tendency to desorb from the surface at substrate temperature as high as 900-1100°C. The stability and etching of TiN_xO_y can be now understood in terms of plasma density. Indeed, it is known that hydrogen plasma density increases with increasing pressure from 40 to 80 Torr [4.1]. Therefore, it may lead to the increase of ion and atomic hydrogen flux impinging on the TiN_xO_y surface as well as substrate temperature. As a consequence, the etching rate of TiN_xO_y can be enhanced by increasing pressure. At hydrogen pressure of 40 Torr, the etch rate could be so low that no etch pits are formed after 90 min treatment time. When the pressure increased up to 60 Torr, the etching rate was significantly enhanced and the etch pits were then formed.

Again, it is noted that TiN_xO_y is almost intact under hydrogen plasma pressure below 40 Torr. For a better understanding of stability of TiN_xO_y , chemical composition analyses for as-grown TiN_xO_y and sample 1 were performed by using XPS measurements. The XPS depth profiles in Fig. 4.4 reveal that the chemical composition of the TiN_xO_y film after plasma treatment at gas pressure of 40 Torr remained unchanged with stoichiometry of $\text{TiN}_{0.97}\text{O}_{0.23}$. The oxygen in the as-grown film was not removed from the film by atomic hydrogen from plasma. The unchanged content of oxygen in sample 1 suggests that the properties of $\text{TiN}_{0.97}\text{O}_{0.23}$ films are not affected by hydrogen plasma under

pressure below 40 Torr. High-resolution XPS spectra of Ti-2p and O-1s were examined to identify the chemical states of the as-grown $\text{TiN}_{0.97}\text{O}_{0.23}$ and sample 1 (Fig. 4.5). As shown in Fig. 4.5a, the Ti-2p spectrum of sample 1 reveals neither reduction of Ti to metallic state nor formation of TiH_2 even at the surface region of $\text{TiN}_{0.97}\text{O}_{0.23}$ film after hydrogen treatment. The Ti-2p peak can be deconvoluted into three components of titanium nitride (454.8 eV), titanium oxynitride (~ 456.9 eV), and titanium dioxide (458.5 eV) [4.7]. After sputtering of the film surface for a few nanometers, the Ti-2p spectra of as-grown and treated $\text{TiN}_{0.97}\text{O}_{0.23}$ films show exactly the same peak position and shape. The difference in the Ti-2p spectra between two samples is only found at the surface region, in which the as-grown film shows a much stronger TiO_2 signal compared with that of sample 1. Therefore, the shift of Ti peak to higher oxidation state (TiO_2) of the as-grown film surface is larger than that of the treated film. This implies that hydrogen plasma reduces the surface oxide in some extent. The decrease of TiO_2 signal at the surface region of the treated film may also suggest that hydrogen plasma treatment results in the surface passivation of TiN_xO_y that similar to the case of nitrogen/hydrogen plasma [4.8]. Figure 4.5b shows the corresponding O-1s spectra of as-grown and hydrogen plasma treated $\text{TiN}_{0.97}\text{O}_{0.23}$. In addition to titanium dioxide (530.5 eV) and titanium oxynitride (531.5 eV) [4.7], the surface region of the as-grown film also shows a component at 532.8 eV that can be assigned to the surface contamination (CO and C-OH) or Ti-OH groups [4.9, 10]. After hydrogen plasma treatment at 40 Torr, the surface of the treated film shows a strong and broaden peak at ~ 532.8 eV that can be explained by the enhancement of Ti-OH groups. The above XPS results provide strong evidence that TiN_xO_y is very chemically stable in hydrogen microwave plasma under pressure below 40 Torr and atomic hydrogen from plasma affects mostly on the surface region of TiN_xO_y film.

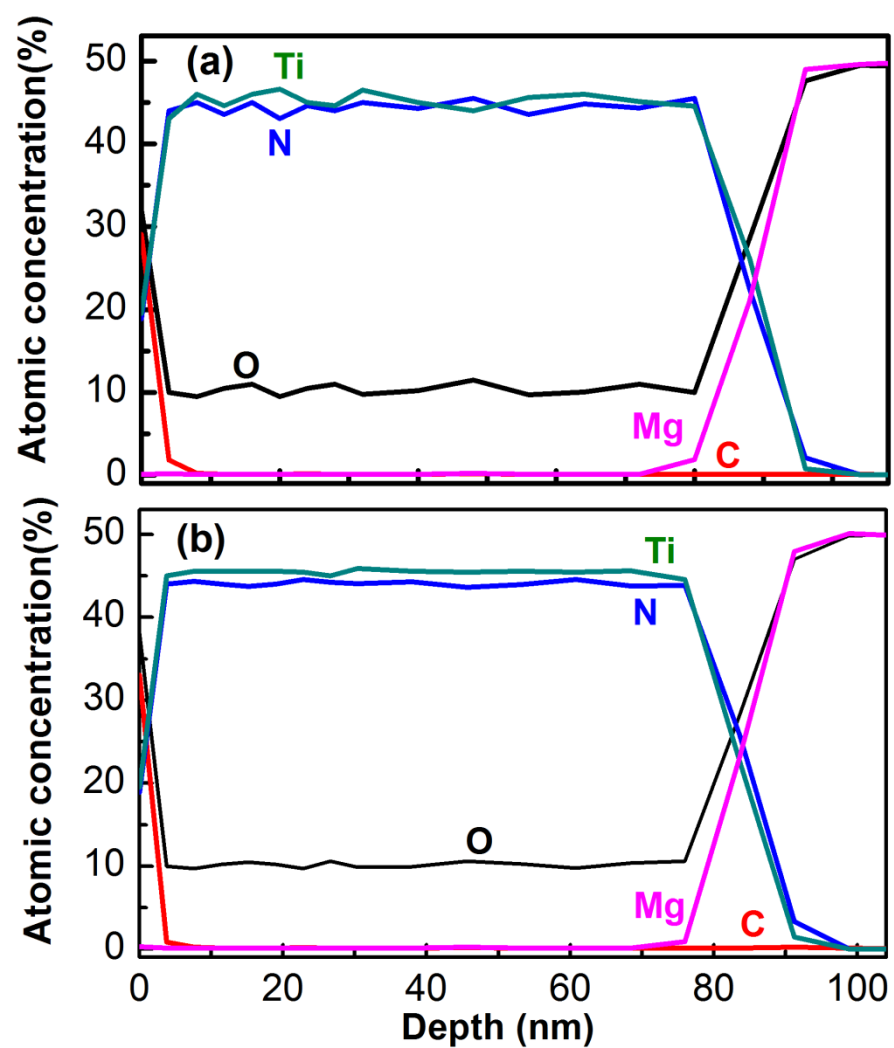


Figure 4.4: XPS depth profiles for (a) as-grown TiN_xO_y film and (b) sample 1.

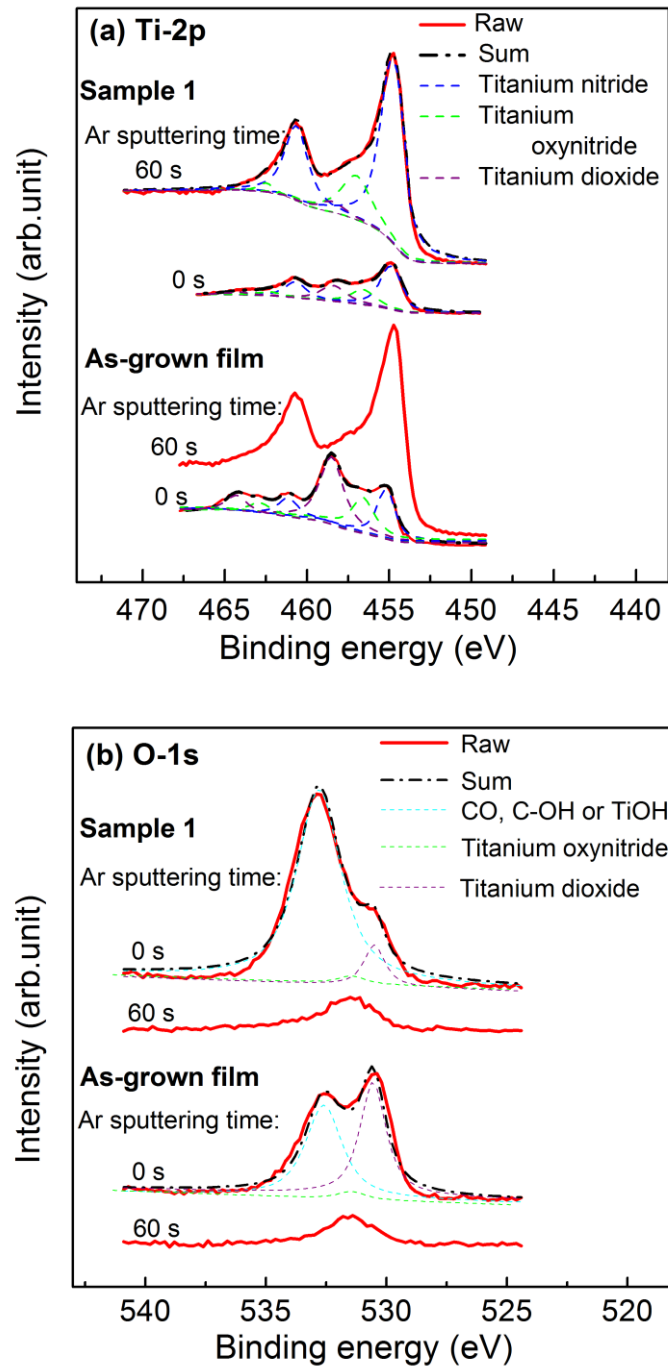


Figure 4.5: High-resolution XPS spectra for (a) Ti-2p and (b) O-1s as function of Ar sputtering time of as-grown TiN_xO_y and sample 1. The spectra were deconvoluted into components using Voigt curve fitting.

The stability of TiN_xO_y was also investigated by using x-ray diffraction. As seen in Fig. 4.6 typical XRD patterns of as-grown TiN_xO_y and sample 1 show only (002) and

(004) reflections of TiN_xO_y and MgO . No extra peaks such as Ti and TiH_2 are detected for treated TiN_xO_y films, indicating that TiN_xO_y remains stable under hydrogen plasma treatment for 90 min at pressure of 40 Torr consistent with the XPS result above. The inset of Fig. 4.6 also shows that the full width at half maximum (FWHM) of the rocking curve of (002) TiN_xO_y for sample 1 after hydrogen plasma treatment increased slightly from 230 arcsec to 280 arcsec. The d-spacing of (004) TiN_xO_y for the as-grown and treated TiN_xO_y films are determined as 1.0636 Å and 1.0639 Å, respectively. No apparent change in the d-spacing, together with the stability of chemical composition, indicates that the thermal effect of plasma treatment has not caused any noticeable change in the strain state of TiN_xO_y (-0.69 %) in spite of the treatment at high-temperature. The x-ray reflectivity (XRR) curves of as-grown sample and sample 1 (Fig. 4.7) show also no difference in the critical angle and distance between period of the interference fringes, indicating no change in the density and thickness of the TiN_xO_y films after treatment at hydrogen pressure below 40 Torr, respectively. The decrease of the fringe intensity suggests that the TiN_xO_y surface is rougher after plasma treatment. However, the hydrogen plasma treatment had no effect on the $\text{TiN}_x\text{O}_y/\text{MgO}$ interface because any increase in interface roughness will cause fringe amplitude to fall off more quickly with increasing scattering angle and may smear out the fringes. Analysis of interference fringes gives thickness and interface roughness of 76 nm and 0.2 nm for both samples; and surface roughness of as-grown and treated films can be determined as 0.3 nm and 0.4 nm in agreement with the AFM result. It has been shown that MgO is easily etched if the surface is in direct exposure to the plasma containing atomic hydrogen [4.11]. Therefore, the sharp interface still remained after plasma treatment implies that MgO can be protected by the TiN_xO_y in microwave hydrogen plasma under pressure below 40 Torr. The XRD patterns for the etched samples 2, 3, 4, and 5 also show (002) and (004) reflections of TiN_xO_y with almost unchanged d-spacing, implying that the non-etched region still remains to be TiN_xO_y .

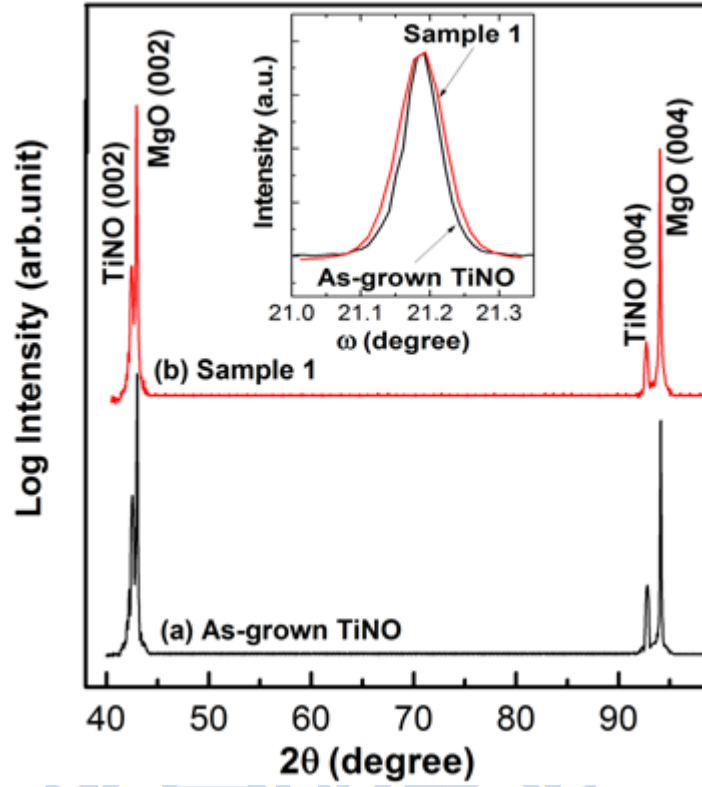


Figure 4.6: XRD 2θ - θ scans for (a) as-grown TiN_xO_y and (b) sample 1. The corresponding XRD ω -scan of (002) TiN_xO_y is displayed in the inset.

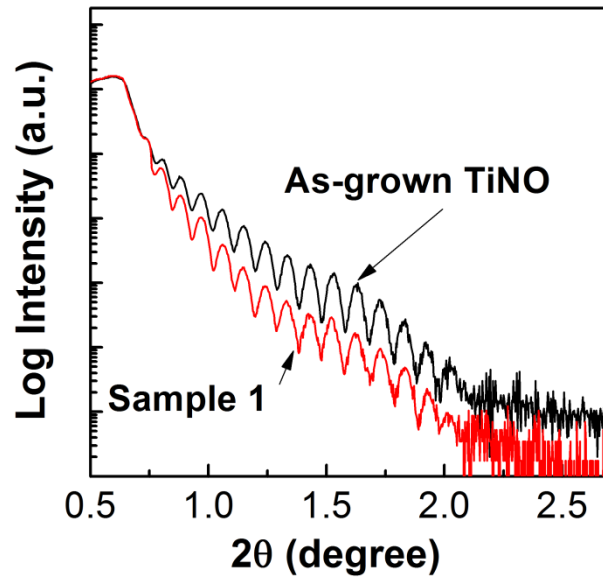


Figure 4.7: X-ray reflectivity curves for TiN_xO_y films before and after treatment at 40 Torr for 90 min.

4.4. Summary

It has been demonstrated that titanium oxynitride is very chemically and thermally stable in microwave hydrogen plasma under pressure below 40 Torr; XPS and XRD provide strong evidence that the chemistry and crystallinity of 76 nm thick TiN_xO_y films in plasma are almost intact. The etch pits with inverse pyramid shape are found to occur on (001) TiN_xO_y surface at pressure as high as 60 Torr. AFM examinations reveal that the etch size and etch depth increase with increased etching time and pressure.



References

- [4.1] Oleg A. Popov , , New Jersey, USA, 1995., High Density Plasma Sources: Design, Physics and Performance, Noyes Publications, New Jersey, USA, 1995.
- [4.2] P. Bou, J.C. Boettner, L. Vandenbulcke, Kinetic calculations in plasmas used for diamond deposition, Jpn J Appl Phys 1, 31 (1992) 1505-1513.
- [4.3] Y. Shigesato, R.E. Boekenhauer, B.W. Sheldon, Emission-spectroscopy during direct-current-biased, microwave-plasma chemical-vapor-deposition of diamond, Applied Physics Letters, 63 (1993) 314-316.
- [4.4] V.G. Ralchenko, A.A. Smolin, V.I. Konov, K.F. Sergeichev, I.A. Sychov, I.I. Vlasov, V.V. Migulin, S.V. Voronina, A.V. Khomich, Large-area diamond deposition by microwave plasma, Diam Relat Mater, 6 (1997) 417-421.
- [4.5] S. Mendelson, Dislocation etch pit formation in sodium chloride, J Appl Phys, 32 (1961) 1579-1583.
- [4.6] M.W.J. Chase, NIST-JANAF Thermochemical Tables, American Institute of Physics, New York, USA, 1998.
- [4.7] M.H. Chan, F.H. Lu, Preparation of titanium oxynitride thin films by reactive sputtering using air/Ar mixtures, Surf Coat Tech, 203 (2008) 614-618.
- [4.8] J.K. Huang, C.L. Huang, S.C. Chang, Y.L. Cheng, Y.L. Wang, Effect of N₂/H₂ plasma treatment on the moisture adsorption of MOCVD-TiN films, Thin Solid Films, 519 (2011) 4948-4951.
- [4.9] T.K. Sham, M.S. Lazarus, X-ray photoelectron-spectroscopy (XPS) studies of clean and hydrated TiO₂ (rutile) surfaces, Chem Phys Lett, 68 (1979) 426-432.
- [4.10] T. Kasuga, H. Kondo, M. Nogami, Apatite formation on TiO₂ in simulated body fluid, J Cryst Growth, 235 (2002) 235-240.
- [4.11] K.H. Baik, P.Y. Park, B.P. Gila, J.H. Shin, C.R. Abernathy, S. Norasetthekul, B. Luo, F. Ren, E.S. Lambers, S.J. Pearton, Comparison of plasma etch chemistries for MgO, Appl Surf Sci, 183 (2001) 26-32.

Chapter 5

Conclusions and future works

5.1. Conclusions

The main results of this thesis are summarized as follows:

1. In this study, titanium oxynitride TiN_xO_y films with different chemical composition ($0.63 < x < 1.11$, $0.1 < y < 0.55$) and titanium oxycarbide film with composition of $\text{TiC}_{0.47}\text{O}_{0.69}$ have been heteroepitaxially grown on MgO (001) substrates by pulsed laser deposition at substrate temperature of 700°C with using $\text{TiNO}_{0.064}$ and $\text{TiCO}_{0.5}$ targets. The deposition process was carried out under both base pressure and ambient gas of nitrogen varied from 10^{-3} to 10^{-5} Torr. The TiN_xO_y and TiC_xO_y films have good crystallinity (FWHM $\sim 58 - 62$ arcsec for TiN_xO_y and 133 arcsec for TiC_xO_y) even though they are under fully compressive strain. Transmission electron microscopy analyses showed that both TiN_xO_y and $\text{TiC}_{0.47}\text{O}_{0.69}$ films contain a low density of dislocations. The lattice parameters of TiN_xO_y films decrease with increased oxygen concentration, and residual stresses decrease as consequence. The deposited TiN_xO_y and $\text{TiC}_{0.47}\text{O}_{0.69}$ films are very electrically conducting with resistivity of $28\text{-}53\ \mu\Omega\text{cm}$ for TiN_xO_y , and $137\ \mu\Omega\text{cm}$ for $\text{TiC}_{0.47}\text{O}_{0.69}$. The resistivity of TiN_xO_y films also increases as oxygen content increases. The surface of the deposited TiN_xO_y and $\text{TiC}_{0.47}\text{O}_{0.69}$ films is atomically smooth with roughness of $0.26\text{-}0.31\ \text{nm}$ for TiN_xO_y , and $0.18\ \text{nm}$ for $\text{TiC}_{0.47}\text{O}_{0.69}$.
2. Titanium oxynitride is very chemically and thermally stable in microwave hydrogen plasma under pressure below 40 Torr. The etch pits with inverse pyramid shape are found to occur on (001) TiN_xO_y surface at pressure as high as 60 Torr. AFM examinations reveal that the etch size and etch depth increase with increased etching time and gas pressure.
3. Li-Vlassak method for analysis of nanoindentation of hard TiN_xO_y and TiC_xO_y films on soft MgO substrate are used and provide the reliable values for hardness H and Young's modulus E of about $H \sim 17 - 26\ \text{GPa}$ and $E \sim 355 - 430\ \text{GPa}$ for

TiN_xO_y, and $H \sim 21 \pm 1.7$ GPa and $E \sim 390 \pm 6.4$ GPa for TiC_{0.47}O_{0.69} film. Chemical composition and residual compressive stress have strong influence on the mechanical properties of the TiN_xO_y films. Both H and E are found to decrease as oxygen content increases, and increase as nitrogen content increases. With increasing residual compressive stress, the hardness and Young's modulus of TiN_xO_y also increase.

5.2. Future works

We have shown that the oxygen content in the deposited TiN_xO_y and TiC_xO_y films is higher than that of the corresponding target even though the growth process carried out under base pressure of 10^{-6} Torr; and pressure of ambient nitrogen gas plays a major role in the chemical composition of the deposited TiN_xO_y films. Chemical composition of TiN_xO_y films is very sensitive with pressure of nitrogen gas. Therefore, the major issue is how to control the oxygen content incorporated in the TiN_xO_y and TiC_xO_y films, especially in case of low oxygen films.

It is insufficiently to explain the etching mechanisms of TiN_xO_y mainly by thermodynamics. Kinetic analysis is needed to explore the etching behavior. However, because of complexity of the plasma interacting with the surface, it is not easy to explore the kinetics with current experimental data. Therefore another challenge is how to develop an appropriate experimental design to explore the kinetic process of etching of TiN_xO_y.

Stability and etching of TiC_xO_y films still need to be investigated.

Mechanical properties of hard TiN_xO_y and TiC_xO_y films on soft MgO substrate were characterized using nanoindenter, and the effect of soft substrate was excluded by using Li-Vlassak analysis. However, all films investigated in this study are under compressive stress that can affect the nanoindentation results. Hence, the big challenge remains in this study is how to extract the intrinsic hardness and Young's modulus of TiN_xO_y and TiC_xO_y films.

Finally, only one titanium oxycarbide with composition of TiC_{0.47}O_{0.69} is reported in this study. There is a lack of titanium oxycarbide film with different composition; therefore the effect of oxygen content on lattice parameters and mechanical properties of TiC_xO_y films is still unclear. The works remain here are to deposit epitaxial TiC_xO_y films

with chemical composition that vary in a possible range, and to study the effect of chemical composition on lattice parameter, strain/stress, and mechanical properties of TiC_xO_y films.



Appendix A

Continuous stiffness measurement (CSM)

The CSM is accomplished by imposing a harmonic force, which is added to the nominally increasing load P , on the indenter as shown in Fig. A.1. The displacement response of the indenter at the excitation frequency and the phase angle between the two are measured continuously as a function of depth. Solving for the in-phase and out-of-phase portions of the response results in an explicit determination of the contact stiffness, S , as a continuous function of depth [3.1, 3.7, 3.8]. This allows the measurement of contact stiffness at any point along the loading curve and not just at the point of unloading as in the conventional measurement. To calculate the contact stiffness, the dynamic response of the indentation system has to be determined. The relevant components are the mass, m , of the indenter, the spring constant, K_s , of the leaf springs that support the indenter, the stiffness of the indenter

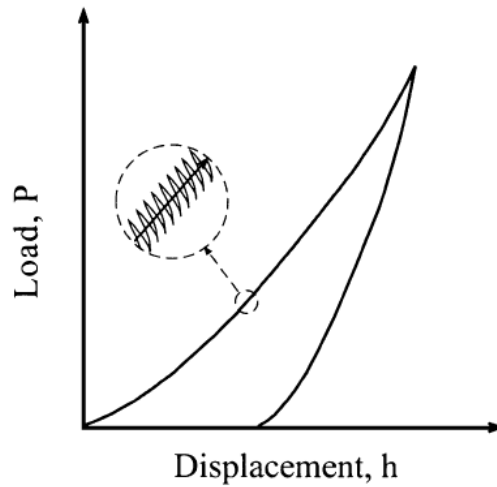


Figure A.1: Schematic of the CSM loading cycle.

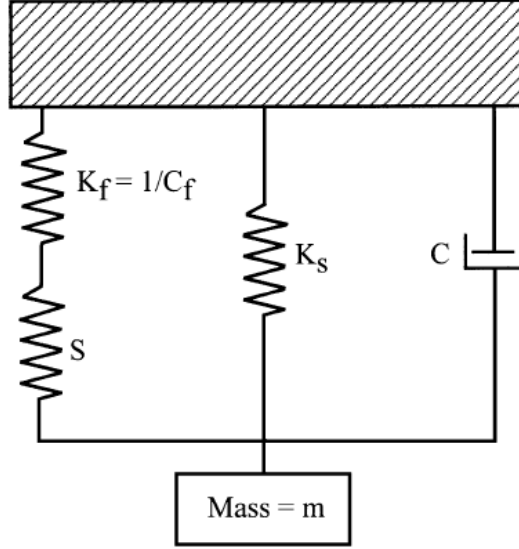


Figure A.2: Schematic of the dynamic indentation model.

frame $K_f = 1/C_f$, where C_f is the compliance of the load frame and the damping coefficient, C , due to the air in the gaps of the capacitor plate displacement sensing system. These combined with the contact stiffness, S , produce the overall response as shown in Fig. A.2. If the imposed driving force is $P = P_{os} \exp(i\omega t)$ and the displacement response of the indenter is $h(\omega) = h_o \exp(i\omega t + \phi)$, the contact stiffness, S , can be calculated from the displacement signal,

$$\left| \frac{P_{os}}{h(\omega)} \right| = \sqrt{\{(S^{-1} + K_f^{-1})^{-1} + K_s - m\omega^2\}^2 + \omega^2 C^2} \quad (\text{A.1})$$

or from the phase difference between the force and displacement signals, the phase angle, ϕ , is:

$$\tan(\phi) = \frac{\omega C}{(S^{-1} + K_f^{-1})^{-1} + K_s - m\omega^2} \quad (\text{A.2})$$

where P_{os} is the magnitude of the force oscillation, $h(\omega)$ is the magnitude of the resulting displacement oscillation, ω is the frequency of the oscillation, and ϕ is the phase angle between the force and displacement signals. Eqs. (A.1) and (A.2) can be solved for the contact stiffness, S , and the damping due to the air in the gaps between the capacitor plates

ωC (the damping of the sample itself is regarded to be negligible). The contact stiffness, S , and the damping, ωC , can be given by Eqs. (A.3) and (A.4), respectively:

$$S = \left[\frac{1}{\frac{P_{os}}{h(\omega)} \cos \phi - (K_s - m\omega^2)} - K_f^{-1} \right]^{-1}$$

(A.3)

$$\omega C = \frac{P_{os}}{h(\omega)} \sin \phi$$

(A.4)



Appendix B

Yu's analysis: Elastic indentation problem and solution

The two important parameters in Yu's analysis are $\gamma = a / a_h$, the ratio of the contact radius of the film/substrate to that of the homogeneous film material, and P / P_h , the ratio of the load on the film/substrate to that of the homogeneous film material. The respective ratios are taken at the same indentation depth h into the film/substrate system and the bulk homogeneous film material (Fig. B.1).

The elastic indentation of a layered half-space is mathematically a mixed boundary value problem that can be reduced to a Fredholm integral equation of the second kind [3.14]:

$$H(\tau) - \frac{1}{\pi} \int_0^1 [K(y+\tau) + K(y-\tau)] H(y) dy = F_0(\tau) \quad (\text{B.1})$$

The solution of the contact problem is given in terms of a function $H(\tau)$ that can be regarded as a normalized map of the pressure distribution within the contact region. The kernel of the integral equation, $K(u)$, is given by [3.14, 3.16]:

$$K(u) = \frac{a}{t} \int_0^\infty g(w) \cos\left(uw \frac{a}{t}\right) dw \quad (\text{B.2})$$

where

$$\begin{aligned}
g(u) &= 1 - \frac{A \cdot 2w + B \cdot \cosh(2w) + C \sinh(2w)}{D + C \cdot \cosh(2w) + B \sinh(2w) - A \cdot (2w)^2} \\
A &= \left(1 - \frac{M_f(1-\nu_f)}{M_s(1-\nu_s)} \right) \left(4 \frac{M_f(1-\nu_f)}{M_s(1-\nu_s)} \nu_s - 3 \frac{M_f(1-\nu_f)}{M_s(1-\nu_s)} - 1 \right) \\
B &= 8 \frac{M_f(1-\nu_f)}{M_s(1-\nu_s)} (\nu_f - 1)(\nu_s - 1) \\
C &= 3 - 4\nu_f + \frac{M_f(1-\nu_f)}{M_s(1-\nu_s)} \left[2 + 3 \frac{M_f(1-\nu_f)}{M_s(1-\nu_s)} - 4\nu_f - 4\nu_s \left(1 + \frac{M_f(1-\nu_f)}{M_s(1-\nu_s)} - 2\nu_f \right) \right] \\
D &= \left(\frac{M_f(1-\nu_f)}{M_s(1-\nu_s)} \right)^2 (4\nu_s - 3) - 2 \frac{M_f(1-\nu_f)}{M_s(1-\nu_s)} (2\nu_s - 1)(2\nu_f - 1) + 4\nu_f(2\nu_f - 3) + 5
\end{aligned} \tag{B.3}$$

where M_f and M_s are the indentation moduli of the film and subastrate, respectively; ν_f and ν_s are Poisson's ratio of the film and the substrate, respectively. The right-hand side of Eq. (B.1) is determined by the shape of the indenter. For a conical punch, for instance,

$$F_0(\tau) = 1 - \gamma\tau \tag{B.4a}$$

while for a spherical punch of radius R ,

$$F_0(\tau) = 1 - \gamma\tau \cdot \frac{\ln(1+\tau\rho) - \ln(1-\tau\rho)}{\ln(1+\rho/\gamma) - \ln(1-\rho/\gamma)} \tag{B.4b}$$

In these equations, $\rho = a/R$. The relationship between the contact radius a_h and the indentation depth h for an elastic indentation in a homogenous half space depends on the indenter shape [Math Proc. Cambridge Philos. Soc. , 41 (1945) 16]. For a conical punch with half included angle θ , one finds that,

$$h = \frac{\pi a_h}{2 \tan(\theta)} \tag{B.5a}$$

while for a spherical punch of radius R ,

$$h = \frac{a_h}{2} \left(\ln \frac{1+a_h/R}{1-a_h/R} \right) \tag{B.5b}$$

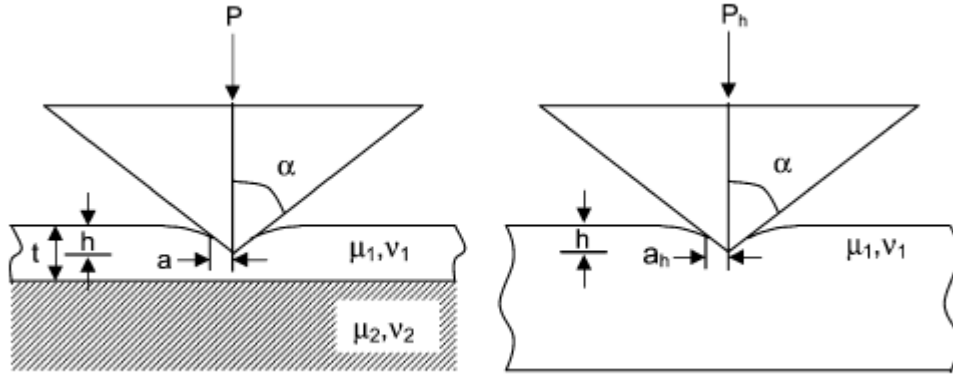


Figure B.1: The load ratio, P/P_h , and the contact radius ratio, $\gamma = a/a_h$, are calculated in the study by Yu *et al.* using the integral equation method. (The subscript h refers to the values for the homogeneous film material cases, and the parameters without the subscript refer to the film-on-substrate case.

The solution to the Fredholm equation is obtained by using the El-Gendi [Comput. J., 12 (1969) 282] method, where $H(\tau)$ is solved numerically in the form of a Chebyshev series with $N \geq 5$. For all of the work presented in this paper, $N = 6$ was used. $H(\tau)$ is solved by initially setting γ equal to 1 and then iterating γ until the boundary condition $H(1) = 0$ is satisfied. With the knowledge of the function $H(\tau)$ and the corresponding γ , Yu *et al.* were then able to obtain the load as a function of depth for conical indentation into the film/substrate system according to the following equation:

$$P = 2\gamma\zeta_f h^2 \tan \theta \int_0^1 H(\tau) d\tau \quad (\text{B.6})$$

where

$$\zeta_f = \frac{2E_f}{\pi(1-\nu_f^2)} \quad (\text{B.7})$$

is the indentation modulus of the film material. The results of Yu *et al.* can be used to determine the relationship between the contact stiffness $S = dP/dh$ and the contact radius a , as explained in ref. [3.16]. Before applying the results from the analysis by Yu *et al.* to

experimental data, the “reduced stiffness” S_r that takes into account the compliance of the diamond indenter tip needs to be determined, as also explained in [3.16].

* Some useful results from Yu’s solution

In an elastic indentation of a homogeneous half-space, the elastic deflection of the surface h_s is related to the indentation load and the contact stiffness through Eq. (4.3). For a film on a substrate, h_s also depends on the elastic mismatch between the film and the substrate, necessitating a dimensionless correction factor ξ in the expression for the surface deflection:

$$h_s = \xi(a/t, M_f/M_s, \nu_f, \nu_s) \varepsilon \frac{P}{S} \quad (\text{B.8})$$

The elastic deflection of the surface is also related to the contact radius through the indenter geometry. For a conical punch with half included angle θ , one has

$$h_s = h - h_c = h - a/\tan \theta \quad (\text{B.9})$$

Using Eqs. (B.5) through (B.9), ξ can be calculated as a function of a/t and for different levels of elastic mismatch between film and substrate. Results for a conical indenter are shown in Fig. B.2a. When the film has the same elastic properties as the substrate, ξ is obviously equal to one. As $a/t \rightarrow 0$, the curves also satisfy the condition $\xi \rightarrow 1$ independent of the elastic mismatch between film and substrate. This extreme case corresponds to an indentation in the homogeneous film material, for which ξ should be equal to one. A similar trend is observed for large contact areas, where the effect of the film is negligible and the indenter is effectively probing the substrate. It is further evident from Fig. B.2a that

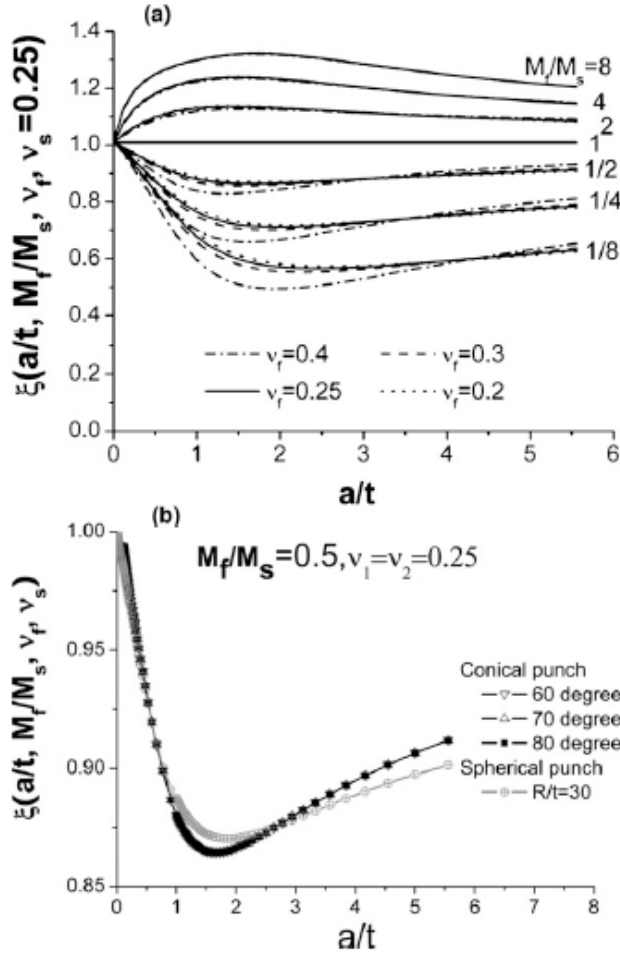


Figure B.2: The dimensionless correction factor ξ for an elastic indentation as a function of normalized contact radius for (a) different elastic mismatch and a conical indenter, and for (b) various indenter shapes.

Poisson's ratio of the film has a relatively minor effect on the value of ξ , especially if the film is stiffer than the substrate. Fig. B.2b shows ξ as a function of a/t for several conical indenters with different half included angles ($\theta = 60^\circ, 70^\circ, 80^\circ$) and for a spherical indenter ($R/t = 30$). Evidently there is a small difference between conical and spherical indenters, but for conical indenters ξ does not depend on the apex angle of the indenter.

Analysis of nanoindentation data requires the relationship between the contact stiffness and the contact radius. We have calculated the contact stiffness S as a function of the contact radius for a series of film/substrate combinations for a conical indenter with a half included angle of 70° . The results are shown on a logarithmic scale in Fig. B.3a. It is

clear that for small contact radii, the contact stiffness changes linearly with contact radius and conforms to Sneddon's equation for homogeneous materials. As the contact radius grows, the effect of the substrate becomes evident and the slopes of the curves gradually deviate from unity: the slopes increase for stiff films on compliant substrates and decrease for compliant films on stiff substrates. At large contact radii, all curves again approach Sneddon's equation as the effect of the film fades.

For a given contact area, the contact stiffness of an indenter on a homogeneous and isotropic half space is independent of the precise indenter shape as long as the indenter is axisymmetric and the profile of the punch can be approximated by a half-space—that is, the apex angle γ should be close to 180° for a conical punch, or $a/R \ll 1$ or a spherical punch [Comput. J., 12 (1969) 282]. Consequently, the contact stiffness of an arbitrary axisymmetric indenter on an elastic half space is equal to that for a flat-ended indenter with radius equal to the contact radius. The same conclusion holds true for the indentation of a film on a substrate: In Fig. B.3b, we show the S - a relationship calculated from Yu's solution for a given film-on-substrate assembly ($M_f/M_s = 0.5, \nu_f = \nu_s = 0.25$) indented by several conical ($\theta = 60^\circ, 70^\circ, 80^\circ$) and spherical indenters ($R/t = 10, 30$). All curves overlap perfectly, confirming that for films on substrates the contact stiffness is also independent of the indenter shape, at least within the context of linear elastic contact mechanics. This observation is easily rationalized based on Hill's cumulative superposition argument and is the foundation of the new analysis method. When analyzing the elastic unloading process after an elasto-plastic indentation in a thin film, the relationship between contact stiffness and contact radius can be calculated without knowledge of the precise shape of the indentation, that is, without knowledge of the plastic properties of the film.

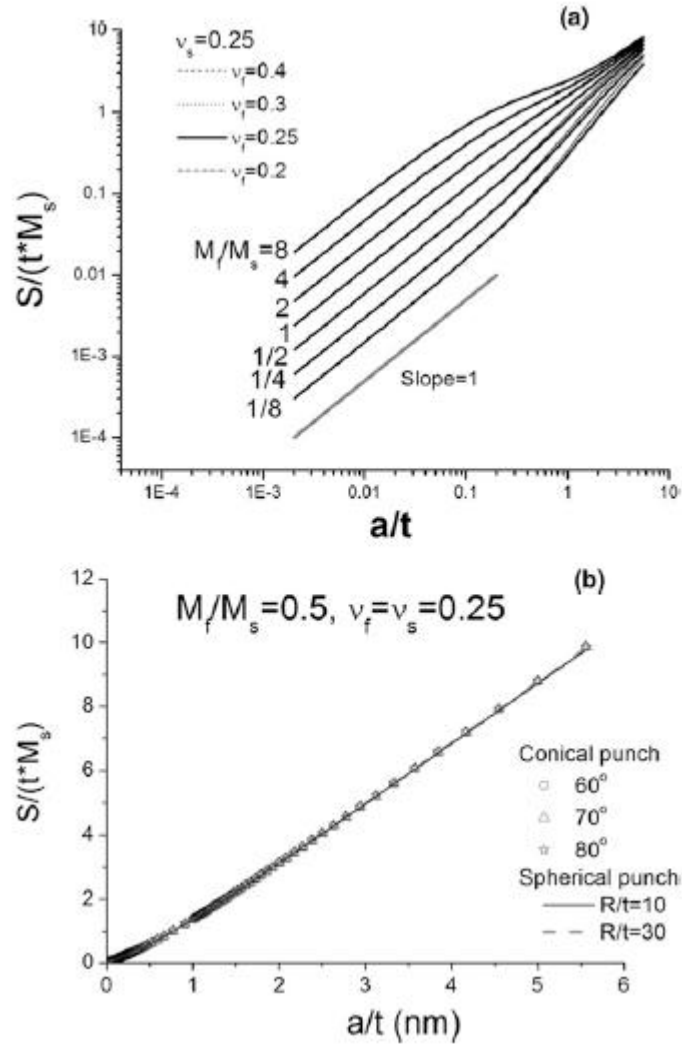


Figure B.3: Normalized contact stiffness versus contact radius calculated from Yu's solution for (a) different elastic mismatches, and (b) various conical and spherical punches.

List of publications

Journal Papers

- [1] S.K. Chong, B.T. Goh, Y.Y. Wong, H.Q. Nguyen, H. Do, I. Ahmad, Z. Aspanut, M.R. Muhamad, C.F. Dee, S.A. Rahman, Structural and photoluminescence investigation on the hot-wire assisted plasma enhanced chemical vapor deposition growth silicon nanowires, *J Lumin*, 132 (2012) 1345-1352.
- [2] H. Do, V.T. Dai, J.S. Tian, T.C. Yen, L. Chang, Nanoindentation studies of epitaxial titanium oxynitride (001) films grown on MgO(001) substrate (submitted), in 2013.
- [3] H. Do, Y.H. Wu, V.T. Dai, C.Y. Peng, T.C. Yen, L. Chang, Structure and property of epitaxial titanium oxynitride grown on MgO(001) substrate by pulsed laser deposition, *Surf Coat Tech*, 214 (2013) 91-96.
- [4] H. Do, T.C. Yen, L. Chang, Stability and etching of titanium oxynitride films in hydrogen microwave plasma, *Journal of Vacuum Science & Technology A*, 31 (2013) 041304.
- [5] H. Do, T.C. Yen, C.S. Tian, Y.H. Wu, L. Chang, Epitaxial growth of titanium oxycarbide on MgO (001) substrates by pulsed laser deposition, *Appl Surf Sci*, 257 (2011) 2990-2994.
- [6] J.S. Tian, Y.H. Wu, C.Y. Peng, K.A. Chiu, Y.S. Shih, H. Do, P.Y. Lin, Y.T. Ho, Y.H. Chu, L. Chang, Defects in semipolar (11 $\bar{2}$)over-bar(2)over-bar) ZnO grown on (112) LaAlO₃/(La, Sr) (Al, Ta)O-3 substrate by pulsed laser deposition, *J Phys-Condens Mat*, 25 (2013).

International Conference

- [1] **H. Do**, T.C. Yen, C.S. Tian, Y.H. Wu, L. Chang, Epitaxial growth of titanium oxycarbide on MgO (001) substrates by pulsed laser deposition. IUMRS 2011, Taipei, Taiwan.
- [2] **Hien Do**, Yue-Han Wu, Chun-Yen Peng, Tzu-Chun Yen, Li Chang, Effect of hydrogen plasma on titanium oxynitride, TACT 2011, Taiwan.

Autobiography

- Name: Do Thi Hien (杜氏賢)
- Gender: Female
- Nationality: Vietnam
- Education:
 - ✓ 2000-2004: Bachelor of Science in Physics, Hanoi National University of Education, Hanoi, Vietnam
 - ✓ 2004-2006: Master of Science in Physics, Institute of Physics and Electronics, Viet Nam Academy of Science and Technology, Ha Noi, Viet Nam.
 - ✓ 2007 – 2013: Ph. D Candidate, Department of Materials Science and Engineering, NCTU, Hsinchu, Taiwan.
- Research:
 - Epitaxial TiN_xO_y and TiC_xO_y films
 - Growth and structure analysis
 - Nanoindentation studies of mechanical properties